

UNIVERSIDADE FEDERAL DO ABC
Curso de Pós-Graduação em Nanociências e Materiais Avançados

Dissertação de Mestrado

Wudmir Yudy Rojas Verastegui

**Electronic and Transport Properties of Graphene
Nanoribbons with Adsorbed Transition Metal Impurities:
Spin-Orbit Interaction**

Santo André, SP, Brasil
2013



Universidade Federal do ABC



Electronic and Transport Properties of Graphene Nanoribbons with Adsorbed Transition Metal Impurities: Spin-Orbit Interaction

Wudmir Yudy Rojas Verastegui

Trabalho apresentado como parte dos
requisitos para obtenção do título de
Mestre em Nanociências e Materiais
Avançados.

Orientador:
Prof. Dr. Alexandre Reily Rocha

Banca Examinadora:
Prof. Dr. Alexandre Reily Rocha - UNESP
Prof. Dr. Cedric Rocha Leão - UFABC
Prof. Dr. Roberto Hiroki Miwa - UFU

Santo André, SP, Brasil
2013

To my parents, *Mavila* and *Nery Rojas*,
my sister *Sadith*,
my wife *Hilda* and our dear son *Dylan*.

Acknowledgements

First of all, I am deeply grateful for Professor Alexandre Rocha's supervision and support of this dissertation. What I learned from him is far beyond knowledge and skills. I really appreciate lots of help and for introducing me to the exciting field of electronic transport at the nanoscale and spintronics. An excellent physicist and great man, I consider myself very lucky to have met and have worked with him in one important phase of my academic life.

This research received the financial support from the Brazilian funding agencies CAPES, CNPQ and from Universidade Federal do ABC. They are responsible for my maintenance, and also provided me support to attend conferences. The calculations included in this dissertation were performed in the HPC clusters at the Universidade de São Paulo and Universidade Federal do ABC for which I am very grateful.

Undoubtedly, each of the group sessions were very useful and stimulating, hence special acknowledgements to all the members at the TransSim group: Rodrigo Garcia Amorim, Jeconias Guimaraes, Tarciso Silva de Andrade, Pedro Brandimarte, Cláudio Padilha, Ekaterina Filatova and César Perez. I would also like to thank all members of ABCsim's room, a place where I spent most of the time during these two years and where people made me feel like a Brazilian. Last but not least, I would like to thank all Peruvian students at Universidade Federal do ABC for lots of great time shared along this period.

I would like to thank my parents Mavila and Nery who always trusted my decision of a scientific life since the beginning and strongly encouraged me to pursue my PhD degree. This is the first step Mom and Dad. I knew how hard it is to have a family since I left the undergraduate course and even more how difficult it is, still pursuing a graduate degree, for that reason I would like to deeply thank my wife Hilda for her maturity, support and for being both father and mother of our son these two long years. Surely, special thanks to Dylan, my beloved son, for behaving like a real little man despite his age during my absence. I am greatly indebted to them. Finally, special thanks to my Peruvian friends Percy Galvez, Ricardo Egoavil and Oscar Chacaltana, who gave me their unconditional support at an important stage of my academic life.

Abstract

Graphene is a truly two dimensional material - a single carbon atom thick system. Its exceptional electronic properties combined with its weak spin-orbit (SO) interaction - which lead to large spin relaxation length - make it a very interesting material for studying spin transport. Therefore, graphene is considered as a promising candidate for spintronics applications - use of the electron spin degree of freedom instead of its charge - where one can exploit graphene unique electronic properties. However, graphene lacks of energy gap which is essential for the design of digital transistors. This problem can be solved by cutting graphene into strips known as graphene nanoribbons (GNRs) since the band gap depends on its width. Unfortunately, experimental techniques employed to synthesize these GNRs typically include undesired metal atom as impurities which can lead to the introduction of SO and consequently to significant spin-flip processes in conduction electrons.

Our work concerns a first principles study of electronic structure and spin-dependent electron transport of Ni and Ir adatoms on armchair graphene nanoribbon taking into account the SO interaction. We have used a combination of density functional theory (DFT) and non-equilibrium Green's function (NEGFs) methods to carry out those calculations. Moreover, using a recursive NEGFs we also consider a large number of Ni impurities randomly distributed along the AGNR to study transport properties of realistic devices. Finally, we performed the spin relaxation length calculations at specific energy regions of the disordered system.

We found Ni and Ir adatoms prefer hollow sites close to the edges of the AGNR and also we observed SO has induced splitting of the bands close to the Fermi energy, the intensity of those splitting, clearly depend on the adsorption position of the adatoms. We found that single defect and disordered structures exhibit the highest transmission coefficients - both spin conserving (SC) and spin-flip (SF) - when the most stable adsorption system is considered. Moreover, we observed the SC current of the Ni single defect systems is rather higher than the Ir single defect system and conversely the SF current is smaller. Furthermore, from our Polarization (P) results of the disordered systems at specific energy regions, we found that some energy regions are well behaved - P tends to zero when the device length increase - whereas the others exhibit unusual trends where further calculations is needed to get a better understanding. Finally, we

found small spin relaxation lengths - for those well behaved energy regions - compared with Graphene's spin relaxation length.

Contents

Aknowledgements	iii
List of figures	ix
List of tables	xv
1 Introduction	1
1.1 Nanoelectronics	1
1.2 Graphene	2
1.3 Graphene nanoribbons	5
1.4 Spin-orbit coupling in solids	8
1.5 Spintronics	9
1.6 Objectives	10
2 Methodology	11
2.1 Density Functional Theory	11
2.1.1 The many body problem	11
2.1.2 The Born-Oppenheimer approximation	12
2.1.3 The Hohenberg-Kohn theorems	13
2.1.4 The Kohn-Sham equations	14
2.1.5 Exchange-Correlations functionals	17
2.2 Spin-Orbit Density Functional Theory approach	19
2.3 Electronic transport: Non-equilibrium Green's function (NEGF) method	23
2.3.1 Single defect	23
2.3.2 Multiple defects	29
3 Results and discussions I : Single defect	35
3.1 Geometry relaxation	35
3.1.1 Pristine AGNR	37
3.1.2 Nickel impurities	39
3.1.3 Iridium impurities	41

3.2	Electronic structure and spin-polarized transport - Ni	44
3.2.1	Band structures	44
3.2.2	Total DOS and PDOS	48
3.2.3	Single defect transport - Ni	52
3.3	Electronic structure and spin-polarized transport - Ir	55
3.3.1	Band structures	55
3.3.2	Total DOS and PDOS	58
3.3.3	Single defect transport - Ir	63
4	Results and discussions II : Multiple defects	67
4.1	Disordered transport based on Ni@AGNR-1	68
4.1.1	Transmission versus Length at fixed concentration of 0.48 % . .	71
4.2	Transport at energies of interest - Ni@AGNR-1	75
4.3	Transport at energies of interest - Ni@AGNR-s	85
5	Conclusions	93
	Appendices	101
A	Geometry relaxation	101
A.1	Nickel relaxation	101
A.2	Iridium relaxation	105
B	Multiple defects spin-polarized transport	110
B.1	Transmission as a function of Length based on Ni@AGNR-1	111
B.1.1	At fixed concentration of 0.87 %	111
B.1.2	At fixed length of 97.425 nm	112
B.1.3	At fixed length of 194.85 nm	113
B.2	Disordered transport based on Ni@AGNR-s	114
B.2.1	At fixed concentration of 0.48 %	116
B.2.2	At fixed concentration of 0.87 %	117
B.2.3	At fixed length of 97.425 nm	118
B.2.4	At fixed length of 194.85 nm	119

List of Figures

1.1	Orbital s mixed with orbitals p_x and p_y give the hybridized orbitals sp^2 while orbital p_z remains invariant.	3
1.2	Left: lattice structure of graphene in the real space with two atoms, A and B, in the unit cell as basis. Right: Brillouin zone and the high symmetry points K and K' [1].	4
1.3	Electronic dispersion in graphene. The conduction and valence bands touch each other at six discrete points called K/K' points [1].	4
1.4	Left: Armchair graphene nanoribbon. Right: Zig zag graphene nanoribbon. .	6
1.5	First-principles band structures of $N_a - AGNRs$ with $N_a = 12, 13$, and 14, respectively.	6
1.6	Band structure for 8-ZGNR, the horizontal dashed line shows Fermi level for π electrons. The highest occupied band for oppositely oriented Π -electrons are denoted with arrows.	7
2.1	Schematic representation for transport problem at nanoscale. The central scattering region is described by the Hamiltonian H_M , H_{RM} (H_{LM}) correspond to coupling between EM and right (left) leads, H_0 correspond to unit cell of lead and H_1 correspond to coupling between two adjacent unit cells of the lead.	24
2.2	Schematic representation for a multiple defects transport problem at nanoscale. We assumed that the device was built by using different blocks (red and green) and each block is described by H_i and by the coupling V_{ij}	30
2.3	Disordered system scheme where the single defects are randomly separated by pristine segments. L is the total length of the device, L_D is the defect length and L_P is the pristine segment length.	33
3.1	11-AGNR type of ribbon with 1.238 nm of width and composed by three unit cells with lattice vector \vec{a} and lattice constant 4.33 Å.	36
3.2	Top view of possible adsorption sites over the hexagon.	36
3.3	(a) Initial adsorption sites for Ni; (b) Initial adsorption sites for Ir.	37
3.4	(a) Energy dispersion relation. (b) Total DOS of pristine AGNR around Fermi energy.	38

3.5	(a) Initial (triangles) Ni adsorption sites on AGNR; (b) Relaxed (circles) Ni adsorption sites on AGNR. Red circles indicate the systems studied in this work: the most stable (Ni@AGNR-1) and the symmetric (Ni@AGNR-4). From now on, $\text{Ni@AGNR-4} \Leftrightarrow \text{Ni@AGNR-s}$	39
3.6	(a) The most stable structure: Ni@AGNR-1, (b) The symmetric structure: Ni@AGNR-s.	40
3.7	(a) Initial (triangles) Ir adsorption sites on AGNR; (b) Relaxed (circles) Ir adsorption sites on AGNR. Red circles indicate the systems studied in this work: the most stable (Ir@AGNR-1) and the symmetric (Ir@AGNR-13). From now on, $\text{Ir@AGNR-13} \Leftrightarrow \text{Ir@AGNR-s}$	41
3.8	(a) The most stable structure: Ir@AGNR-1, (b) The symmetric structure: Ir@AGNR-s.	42
3.9	Energy dispersion of: (a) Pristine AGNR, (b) Ni@AGNR-1, and (c) Ni@AGNR-s without SO coupling.	45
3.10	Energy dispersion of: (a) Pristine AGNR, (b) Ni@AGNR-1, and (c) Ni@AGNR-s with SO coupling.	46
3.11	(a) Band structure around E_F for Ni@AGNR-1. (b) Band structure around E_F for Ni@AGNR-s. Blue lines correspond to SO and black lines to no-SO. The insets show the regions between dashed lines.	47
3.12	Total DOS around Fermi energy of: (a) Pristine AGNR, (b) Ni@AGNR-1 and (c) Ni@AGNR-s.	48
3.13	Atoms Ni, C1, C2 and/or C3 considered to obtain PDOS of each structures: (a) Ni@AGNR-1 and (b) Ni@AGNR-s.	49
3.14	Four of the five $3d$ orbitals consist of four lobes arranged in a plane that is intersected by two perpendicular nodal planes. These four orbitals have the same shape but different orientations. The fifth $3d$ orbital, $3d_{z^2}$, has a distinct shape even though it is mathematically equivalent to the others. The phase of the wave function for the different lobes is indicated by color: orange for positive and blue for negative [2].	49
3.15	For Ni@AGNR-1 : (a) Total DOS. (b) PDOS of Ni, C1, C2, and C3 atoms. (c) PDOS of $3d$ orbitals of Ni atom. These orbitals are: $4s$ (black line), $3d_{xy}$ (turquoise line), $3d_{yz}$ (indigo line), $3d_{z^2}$ (green line), $3d_{xz}$ (orange line) and $3d_{x^2-y^2}$ (magenta line).	50
3.16	For Ni@AGNR-s : (a) Total DOS. (b) PDOS of Ni, C1, and C2 atoms. (c) PDOS of $3d$ orbitals of Ni atom. These orbitals are: $4s$ (black line), $3d_{xy}$ (turquoise line), $3d_{yz}$ (indigo line), $3d_{z^2}$ (green line), $3d_{xz}$ (orange line) and $3d_{x^2-y^2}$ (magenta line).	51
3.17	Scheme of a two-probe setup used for transport computations. A central region (scattering region) is connected to two semi-infinite leads (shadow region). Scattering region is an assemble of the single defect structure sandwiched between two electrodes.	52

3.18	For Ni@AGNR-1: (a) PDOS of Ni orbitals, (b) Spin-conserved ($T_{\uparrow\uparrow} = T_{\downarrow\downarrow}$) and spin-flip ($T_{\uparrow\downarrow} = T_{\downarrow\uparrow} = 0$) transmission probabilities without SO coupling and (c) Spin-conserved ($T_{\uparrow\uparrow} = T_{\downarrow\downarrow}$) and spin-flip ($T_{\uparrow\downarrow} = T_{\downarrow\uparrow}$) transmission probabilities with SO coupling. Dashed lines correspond to transport in the pristine AGNR.	53
3.19	For Ni@AGNR-s: (a) PDOS of Ni orbitals, (b) Spin-conserved ($T_{\uparrow\uparrow} = T_{\downarrow\downarrow}$) and spin-flip ($T_{\uparrow\downarrow} = T_{\downarrow\uparrow} = 0$) transmission probabilities without SO coupling and (c) Spin-conserved ($T_{\uparrow\uparrow} = T_{\downarrow\downarrow}$) and spin-flip ($T_{\uparrow\downarrow} = T_{\downarrow\uparrow}$) transmission probabilities with SO coupling. Dashed lines correspond to transport in the pristine AGNR.	54
3.20	Energy dispersion of: (a) Pristine AGNR, (b) Ir@AGNR-1, and (c) Ir@AGNR-s without SO coupling.	55
3.21	Energy dispersion of: (a) Pristine AGNR, (b) Ir@AGNR-1, and (c) Ir@AGNR-s with SO coupling.	56
3.22	(a) Band structure around E_F for Ir@AGNR-1. (b) Band structure around E_F for Ir@AGNR-s. Blue lines correspond to SO and black lines to no-SO. The insets show the regions between dashed lines.	57
3.23	Total DOS around Fermi energy of: (a) Pristine AGNR, (b) Ir@AGNR-1 and (c) Ir@AGNR-s.	58
3.24	Ir and Carbon atoms for PDOS calculations in stable (a) and symmetric (b) systems.	59
3.25	For Ir@AGNR-1 : (a) Total DOS. (b) PDOS of Ir and carbons C1 and C2. (c-1) PDOS of $6s$, $6px$ and $5d$ orbitals of Ir. (c-2) PDOS of $5d$ orbitals of Ir.	60
3.26	For Ir@AGNR-s : (a) Total DOS. (b) PDOS of Ir and carbons C1 and C2. (c-1) PDOS of $6s$ and $5d$ orbitals of Ir. (c-2) PDOS of $5d$ orbitals of Ir.	62
3.27	Scheme of a two-probe setup used for transport computations. A central region (scattering region) is connected to two semi-infinite leads (shadow region). Scattering region is an assemble of the single defect structure sandwiched between two electrodes.	63
3.28	For Ir@AGNR-1: (a-1) and (a-2) PDOS of Ir orbitals, (b) Spin-conserved ($T_{\uparrow\uparrow} = T_{\downarrow\downarrow}$) and spin-flip ($T_{\uparrow\downarrow} = T_{\downarrow\uparrow} = 0$) transmission probabilities without SO coupling and (c) Spin-conserved ($T_{\uparrow\uparrow} = T_{\downarrow\downarrow}$) and spin-flip ($T_{\uparrow\downarrow} = T_{\downarrow\uparrow}$) transmission probabilities with SO coupling. Dashed lines correspond to transport in the pristine AGNR.	64
3.29	For Ir@AGNR-s: (a-1) and (a-2) PDOS of Ir orbitals, (b) Spin-conserved ($T_{\uparrow\uparrow} = T_{\downarrow\downarrow}$) and spin-flip ($T_{\uparrow\downarrow} = T_{\downarrow\uparrow} = 0$) transmission probabilities without SO coupling and (c) Spin-conserved ($T_{\uparrow\uparrow} = T_{\downarrow\downarrow}$) and spin-flip ($T_{\uparrow\downarrow} = T_{\downarrow\uparrow}$) transmission probabilities with SO coupling. Dashed lines correspond to transport in the pristine AGNR.	65

4.1	Schematic view of the typical setup for a disordered transport calculations. The left and right electrodes (grey shadow) consist of two semi-infinite segments of the pristine AGNR. The one dimensional realistic disordered nanoribbon attached to the electrodes consists of a randomly intercalation of pristine AGNR (blue shadow) and single defect (pink shadow) segments.	67
4.2	Spin-conserved transmission coefficients ($T_{\uparrow\uparrow} = T_{\downarrow\downarrow}$) without spin-orbit coupling as a function of energy of disordered ribbon based on Ni@AGNR-1 structure. (a) At fixed concentration of $[\text{Ni}]_1 = 0.48\%$; (b) At fixed concentration of $[\text{Ni}]_2 = 0.87\%$; (c) At fixed nanoribbon length of $L_1 = 97.425$ nm and (d) At fixed nanoribbon length of $L_2 = 194.85$ nm. Dashed lines correspond to the transmission coefficients for a pristine AGNR.	69
4.3	Spin-conserved transmission coefficients ($T_{\uparrow\uparrow} = T_{\downarrow\downarrow}$) with spin-orbit coupling as a function of energy of disordered ribbon based on Ni@AGNR-1 structure. (a) At fixed concentration of $[\text{Ni}]_1 = 0.48\%$; (b) At fixed concentration of $[\text{Ni}]_2 = 0.87\%$; (c) At fixed nanoribbon length of $L_1 = 97.425$ nm and (d) At fixed nanoribbon length of $L_2 = 194.85$ nm. Dashed lines correspond to the transmission coefficients for a pristine AGNR.	70
4.4	Scattering process in presence of a scatter element; (a) Without influence of SO interaction; (b) With influence of SO interaction.	71
4.5	Disordered transport of nanoribbon at fixed concentration of $[\text{Ni}]_1 = 0.48\%$. (a) Total conductance ($T_{\uparrow\uparrow} + T_{\downarrow\uparrow}$); (b) Spin-conserved ($T_{\uparrow\uparrow} = T_{\downarrow\downarrow}$) transmission probabilities without SO coupling; (c) Spin-conserved ($T_{\uparrow\uparrow} = T_{\downarrow\downarrow}$) and spin-flip ($T_{\uparrow\downarrow} = T_{\downarrow\uparrow}$) transmission probabilities with SO coupling. Dashed lines correspond to transport in the pristine AGNR.	72
4.6	Spin-flip ($T_{\uparrow\downarrow} = T_{\downarrow\uparrow}$) and spin-conserved ($T_{\uparrow\uparrow} = T_{\downarrow\downarrow}$) transmission coefficients as a function of energy of disordered ribbon based on Ni@AGNR-1 and Ni@AGNR-s structures at fixed concentration of $[\text{Ni}]_1 = 0.48\%$. (a) Based on Ni@AGNR-1 with SO; (b) Based on Ni@AGNR-s with SO; (c) Based on Ni@AGNR-1 without SO and (d) Based on Ni@AGNR-s without SO. Dashed lines are the transmission coefficients for pristine AGNR.	74
4.7	Schematic illustration of energy intervals chosen to study the trend of the spin-conserved and spin-flip transmissions.	75
4.8	Spin-conserved transmission coefficients versus length of the disordered device for the set of energy ranges of interest calculated without take into consideration the SO interaction.	77
4.9	Transmission coefficients versus length of the disordered device for the set of energy ranges of interest calculated considering the SO interaction. (a) Spin-conserved transmission coefficients. (b) Spin-flip transmission coefficients.	79
4.10	(a) Total conductance versus length of the disordered device with no SO effect. (b) Total conductance versus disordered device length with SO effect.	80

4.11	Polarization versus length of the disordered device with SO effect for the set of energy ranges of interest.	82
4.12	Polarization as a function of the device length for two energy regions (E_0 and E_7).	83
4.13	Natural logarithm of polarization versus the length of the device showing the data fitting curve.	84
4.14	Schematic illustration of energy intervals chosen to study the trend of the spin-conserved and spin-flip transmissions.	85
4.15	Spin-conserved transmission coefficients versus length of the disordered device for the set of energy ranges of interest calculated without take into consideration the SO interaction.	87
4.16	Transmission coefficients versus length of the disordered device for the set of energy ranges of interest calculated considering the SO interaction. (a) Spin-conserved transmission coefficients. (b) Spin-flip transmission coefficients.	88
4.17	(a) Total conductance versus length of the disordered device with no SO effect. (b) Total conductance versus disordered device length with SO effect.	89
4.18	Polarization versus disordered device length with SO effect for the set of energy ranges of interest.	90
4.19	Polarization as a function of the device length for five energy regions (E_0 , E_3 , E_4 , E_5 and E_6).	91
4.20	Natural logarithm of polarization versus the length of the device showing the data fitting curve.	92
B.1	Disordered transport of nanoribbon at fixed concentration of $[\text{Ni}]_2 = 0.87\%$. (a) Spin-conserved ($T_{\uparrow\uparrow} = T_{\downarrow\downarrow}$) transmission probabilities without SO coupling; (b) Spin-conserved ($T_{\uparrow\uparrow} = T_{\downarrow\downarrow}$) and spin-flip ($T_{\uparrow\downarrow} = T_{\downarrow\uparrow}$) transmission probabilities with SO coupling. Dashed lines correspond to transport in the pristine AGNR.	111
B.2	Disordered transport of nanoribbon at fixed length of $L_1 = 97.425$ nm. (a) Spin-conserved ($T_{\uparrow\uparrow} = T_{\downarrow\downarrow}$) transmission probabilities without SO coupling; (b) Spin-conserved ($T_{\uparrow\uparrow} = T_{\downarrow\downarrow}$) and spin-flip ($T_{\uparrow\downarrow} = T_{\downarrow\uparrow}$) transmission probabilities with SO coupling. Dashed lines correspond to transport in the pristine AGNR.	112
B.3	Disordered transport of nanoribbon at fixed length of $L_2 = 194.85$ nm. (a) Spin-conserved ($T_{\uparrow\uparrow} = T_{\downarrow\downarrow}$) transmission probabilities without SO coupling; (b) Spin-conserved ($T_{\uparrow\uparrow} = T_{\downarrow\downarrow}$) and spin-flip ($T_{\uparrow\downarrow} = T_{\downarrow\uparrow}$) transmission probabilities with SO coupling. Dashed lines correspond to transport in the pristine AGNR.	113

B.4	Spin-conserved transmission coefficients ($T_{\uparrow\uparrow} = T_{\downarrow\downarrow}$) without spin-orbit coupling as a function of energy of disordered ribbon based on Ni@AGNR-s structure. (a) At fixed concentration of $[\text{Ni}]_1 = 0.48\%$; (b) At fixed concentration of $[\text{Ni}]_2 = 0.87\%$; (c) At fixed nanoribbon length of $L_1 = 97.425\text{ nm}$ and (d) At fixed nanoribbon length of $L_2 = 194.85\text{ nm}$. Dashed lines are the transmission coefficients for pristine AGNR.	114
B.5	Spin-conserved transmission coefficients ($T_{\uparrow\uparrow} = T_{\downarrow\downarrow}$) with spin-orbit coupling as a function of energy of disordered ribbon based on Ni@AGNR-s structure. (a) At fixed concentration of $[\text{Ni}]_1 = 0.48\%$; (b) At fixed concentration of $[\text{Ni}]_2 = 0.87\%$; (c) At fixed nanoribbon length of $L_1 = 97.425\text{ nm}$ and (d) At fixed nanoribbon length of $L_2 = 194.85\text{ nm}$. Dashed lines are the transmission coefficients for pristine AGNR.	115
B.6	Disordered transport of nanoribbon at fixed concentration of 0.48% . (a) Total conductance ; (b) Spin-conserved ($T_{\uparrow\uparrow} = T_{\downarrow\downarrow}$) transmission probabilities without SO coupling; (c) Spin-conserved ($T_{\uparrow\uparrow} = T_{\downarrow\downarrow}$) and spin-flip ($T_{\uparrow\downarrow} = T_{\downarrow\uparrow}$) transmission probabilities with SO coupling in logarithmic scale. Dashed lines correspond to transport in the pristine AGNR.	116
B.7	Disordered transport of nanoribbon at fixed concentration of 0.87% . (a) Spin-conserved ($T_{\uparrow\uparrow} = T_{\downarrow\downarrow}$) transmission probabilities without SO coupling; (b) Spin-conserved ($T_{\uparrow\uparrow} = T_{\downarrow\downarrow}$) and spin-flip ($T_{\uparrow\downarrow} = T_{\downarrow\uparrow}$) transmission probabilities with SO coupling. Dashed lines correspond to transport in the pristine AGNR.	117
B.8	Disordered transport of nanoribbon at fixed length of $L_1 = 97.425\text{ nm}$. (a) Spin-conserved ($T_{\uparrow\uparrow} = T_{\downarrow\downarrow}$) transmission probabilities without SO coupling; (b) Spin-conserved ($T_{\uparrow\uparrow} = T_{\downarrow\downarrow}$) and spin-flip ($T_{\uparrow\downarrow} = T_{\downarrow\uparrow}$) transmission probabilities with SO coupling. Dashed lines correspond to transport in the pristine AGNR.	118
B.9	Disordered transport of nanoribbon at fixed length of $L_2 = 194.85\text{ nm}$. (a) Spin-conserved ($T_{\uparrow\uparrow} = T_{\downarrow\downarrow}$) transmission probabilities without SO coupling; (b) Spin-conserved ($T_{\uparrow\uparrow} = T_{\downarrow\downarrow}$) and spin-flip ($T_{\uparrow\downarrow} = T_{\downarrow\uparrow}$) transmission probabilities with SO coupling. Dashed lines correspond to transport in the pristine AGNR.	119

List of Tables

3.1	Ni adsorption sites, relative energies of relaxed structures and Ni adsorption distances of relaxed structures.	40
3.2	Ir adsorption sites, relative energies of relaxed structures and Ir adsorption distances of relaxed structures.	43
4.1	Values of the energy regions considered in Fig. 4.7.	76
4.2	Spin relaxation length of the energy regions E_0 and E_7	83
4.3	Values of the energy regions considered in Fig. 4.14.	86
4.4	Spin relaxation length of the energy regions E_0 , E_3 , E_4 , E_5 and E_6	92
A.1	Initial and relaxed structures from Ni@AGNR-1 to Ni@AGNR-8 with their respective relative energy in eV after relaxation.	102
A.2	Initial and relaxed structures from Ni@AGNR-9 to Ni@AGNR-16 with their respective relative energy in eV after relaxation.	103
A.3	Initial and relaxed structures of Ni@AGNR-17 with their respective relative energy in eV after relaxation.	104
A.4	Initial and relaxed structures from Ir@AGNR-1 to Ir@AGNR-8 with their respective relative energy in eV after relaxation.	106
A.5	Initial and relaxed structures from Ir@AGNR-9 to Ir@AGNR-16 with their respective relative energy in eV after relaxation.	107
A.6	Initial and relaxed structures from Ir@AGNR-17 to Ir@AGNR-24 with their respective relative energy in eV after relaxation.	108
A.7	Initial and relaxed structures of Ir@AGNR-25 with their respective relative energy in eV after relaxation.	109

Chapter 1

Introduction

1.1 Nanoelectronics

For more than four decades, the Silicon industry has thrived with the rapid improvement in the development of integrated circuit technology. This trend is mainly a result of the industry's ability to exponentially decrease the minimum feature sizes of devices used to fabricate integrated circuits. This trend is usually expressed as Moore's Law [3] (that is, the number of components per chip doubles roughly every 2 years). The most significant trend is the decreasing cost-per-function, which has led to significant improvements in economic productivity and overall quality of life through proliferation of computers, communication, and other industrial and consumer electronics [4]. However, the increase in response of speed and the number of transistors per chip are creating new problems for designers who have endeavoured over the past decades in finding solutions to correct the quantum phenomena limitations that come with miniaturization.

According to experts, the factories cannot bear the high costs that technological progress requires, in addition to addressing the limitations of silicon technology (at such small scales, devices begin show different behaviors). In this perspective, many scientists have committed to new technology trends where devices at the nanoscopic scale present new and challenging issues. At the nanoscale, systems must fundamentally obey quantum mechanics, and as such need to be thoroughly studied.

At the same time electrons have charge and spin, recently in conventional electronics, the charges are manipulated by electric fields but the spins are ignored. Another widespread technology was the magnetization of a ferromagnet to store and read information. The discovery of the giant magnetoresistance effect in 1988 [5] has led to an equivalent of Moore's Law for magnetic recording. However, in the same manner that downsizing is leading to us to the limit at silicon technology, one also envisions a limit to GMR-based devices. Furthermore, one could like to forehead a future where

electronics and spin electronics (spintronics) can be performed in the same chip with new types of devices [6].

1.2 Graphene

Graphene is a promising material which open the possibility to use it in electronics applications due to its exceptional electronic properties. It would also be possible to use the electron spin to design new types of integrated circuits.

Graphene is a single layer of carbon atoms arranged in a honeycomb lattice. It was first studied theoretically by P. Wallace in 1947 [7]. Although, some decades ago Landau [8] and Peierls [9] argued that any 2D crystal was thermodynamically unstable - hence its existence would be impossible - in 2004 Andre Geim and Kostya Novoselov [10] from Manchester University were able to obtain an isolated graphene sheet by using the micro-mechanical cleavage technique. They were awarded the Nobel Prize in 2010 for study electronic transport in graphene. Two years later after being isolated, graphene appeared in hundreds of articles because its unique properties arising from its honeycomb arrangement (combined with the electronic distribution of carbon) that allow us for instance to observe relativistic effects at speeds much lower than the speed of light [11].

The carbon atom has the following distribution $1s^2 2s^2 2p_x^1 2p_y^1$. This structure gives carbon the ability to bind with other atoms in many ways to form a variety of crystals. This comes from a process known as the hybridization [12]. In particular graphene comes of an sp^2 hybridization because all p orbitals initially have the same energy and the electrons prefer to be furthest apart due to the Pauli exclusion principle. The atomic $2s$ orbital mixed with the p_x and p_y orbitals to generate three molecular orbitals known as σ arranged in a trigonal form and are responsible for the strong bands of graphene. The remaining p_z orbital known as π is perpendicular to the σ orbitals, and the electron that is in this orbital is delocalized and is responsible for most of the electronic properties (see Fig. 1.1).

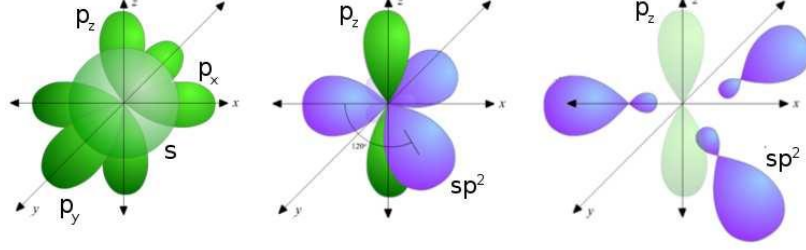


Figure 1.1: Orbital s mixed with orbitals p_x and p_y give the hybridized orbitals sp^2 while orbital p_z remains invariant.

In order to understand the basic properties of graphene we can use a simple model based on nearest neighbour Tight binding approach [13]. The graphene structure is a triangular lattice with two atoms per unit cell as basis (see Fig.1.2). These lattice vectors, reciprocal lattice vectors and nearest neighbours vectors in real space are given by

$$\vec{a}_1 = \frac{a}{2}(3, \sqrt{3}), \quad \vec{a}_2 = \frac{a}{2}(3, -\sqrt{3}) \quad (1.1)$$

$$\vec{b}_1 = \frac{2\pi}{3a}(1, \sqrt{3}), \quad \vec{b}_2 = \frac{2\pi}{3a}(1, -\sqrt{3}) \quad (1.2)$$

$$\delta_1 = \frac{a}{2}(1, \sqrt{3}) \quad \delta_2 = \frac{a}{2}(1, -\sqrt{3}) \quad \delta_3 = -a(1, 0) \quad (1.3)$$

and the positions of the symmetry points in the reciprocal space K and K' (named Dirac points) are given by

$$K = \frac{2\pi}{3a}(1, \sqrt{3}/3), \quad K' = \frac{2\pi}{3a}(1, -\sqrt{3}/3) \quad (1.4)$$

where $a = 1.42 \text{ \AA}$ is the C-C bond length

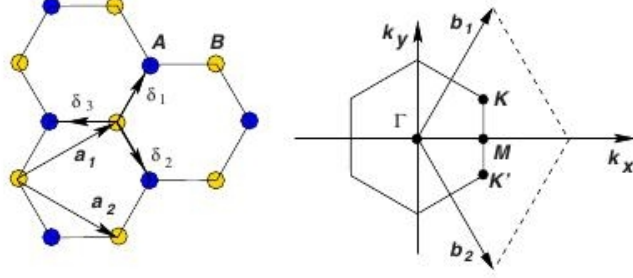


Figure 1.2: Left: lattice structure of graphene in the real space with two atoms, A and B, in the unit cell as basis. Right: Brillouin zone and the high symmetry points K and K' [1].

Therefore after solving the Tight binding formalism for graphene structure the energy dispersion relation is given by

$$E(\mathbf{k}) = \epsilon_0 \pm t \sqrt{1 + 4 \cos\left(\frac{3ak_x}{2}\right) \cos\left(\frac{\sqrt{3}ak_y}{2}\right) + 4 \cos^2\left(\frac{\sqrt{3}ak_y}{2}\right)} \quad (1.5)$$

and the plot of this energy dispersion is shown in Fig.1.3

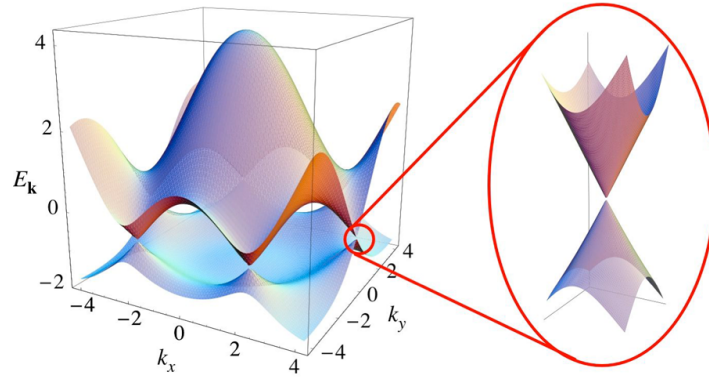


Figure 1.3: Electronic dispersion in graphene. The conduction and valence bands touch each other at six discrete points called K/K' points [1].

Graphene presents an unusual close to linear energy dispersion (see Fig.1.3) around the so-called Dirac points (K and K') where a zero gap allows unusual electronic properties, e.g. It is not a metal because it has a vanishing density of states and also it is not

a typical semiconductor (or insulator) because it does not have a gap in the spectrum. Moreover, due to that particular dispersion it can be mapped into the relativistic equation for massless Dirac fermions except for the fact that in graphene electrons travel as a massless particle with a velocity of the order of 10^6 ms^{-1} (approximately 300 times smaller than the speed of light), therefore the way electrons behave in graphene is very useful to study some fundamental physical properties [11]. Furthermore, because of the near perfect crystal nature of graphene, it is a very clean system to pursue experiments restricting the electrons to only two dimensions. They exhibit some interesting properties such as the anomalous quantum Hall effect and possibly Klein tunnelling [14], topological insulator [15], Hofstadter butterfly [16] and Atomic collapse [17]. Its thermal conductivity was measured at room temperature and it is much higher than the value observed in all the other carbon structures such as carbon nanotubes, graphite and diamond [18]. Since devices continue to shrink and circuit density increases, high thermal conductivity is essential for dissipating heat efficiently thus study of thermal conductivity in graphene may have important implications in graphene-based electronic devices. Moreover, graphene exhibit weak intrinsic spin-orbit interaction which make it interesting to spintronics applications.

1.3 Graphene nanoribbons

One of the problem facing graphene's application in electronics is the lack of an energy gap at the Fermi level. This is a requirement if one wishes to obtain a logical switch - such a transistor. One possible path to circumvent this problem is to further confine electrons in graphene. Graphene nanoribbons (GNRs) are one-dimensional structures made of stripes of graphene. Their structures and their electronic and magnetic properties [19] have been intensively studied both experimentally and theoretically. The confinement to one dimension (1D) introduces significant quantum confinement effects, which give to GNRs several attractive properties [20]. Depending on the edge termination GNRs are classified as Armchair or Zigzag (see Fig.1.4). Taking into account the standard notation, the width of an armchair GNR (AGNR) is defined by the number of dimer lines (N_a) across the ribbons. Equally, the width of a zigzag GNR (ZGNR) is defined by the number of zigzag chains (N_z) across the ribbons.

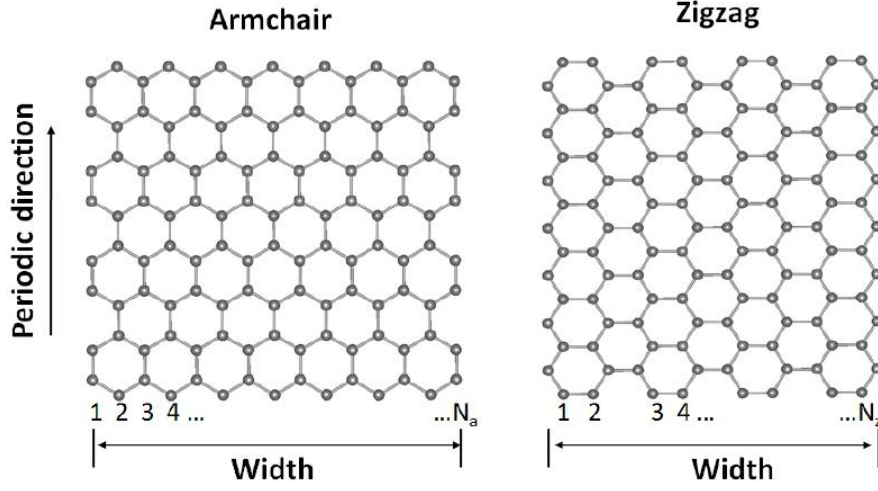


Figure 1.4: Left: Armchair graphene nanoribbon. Right: Zig zag graphene nanoribbon.

Calculations based on tight-binding method predict that all AGNRs are semiconductors with energy gaps decreasing as a function of increasing ribbon widths [21]. On the other hand, the high density of states of the Fermi level in ZGNR is believed to lead to an Stoner instability and to possible magnetic edges, although no conclusive evidence has been found for magnetism in ZGNRs [22]. The ZGNRs within this model are always metallic, those features in the band structures are reported in Figs.1.5 and 1.6 for both GNRs.

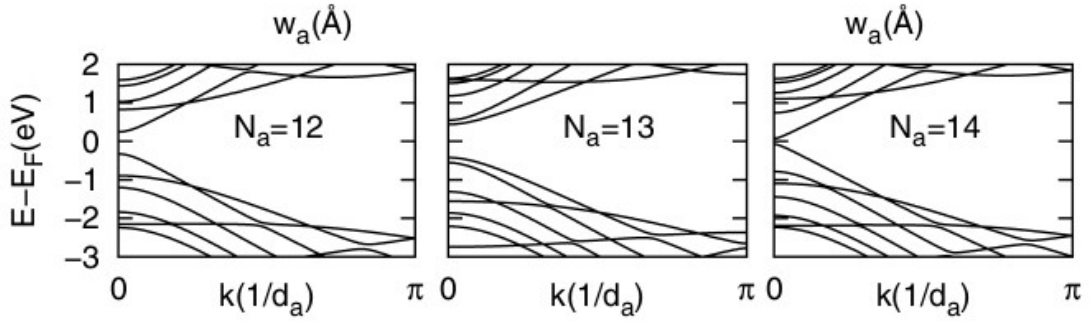


Figure 1.5: First-principles band structures of N_a - AGNRs with $N_a = 12, 13$, and 14 , respectively.

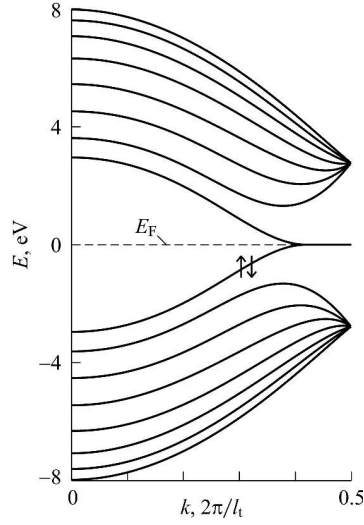


Figure 1.6: Band structure for 8-ZGNR, the horizontal dashed line shows Fermi level for π electrons. The highest occupied band for oppositely oriented Π -electrons are denoted with arrows.

Currently there is development and improvement of several techniques that are tackling the physical limits in fabrication of GNRs. For instance using the fully-fledged micro-lithography technique is expected to be suited for etching GNRs. Also Oxygen plasma [23] and electron beams have been used to etch graphene on SiO_2 wafers. However, due to the limit in spacial resolution, lithographic techniques have been unable to produce narrow GNRs with smooth edges [24]. Scanning Tunnelling Microscopy (STM) can also be used to tailor graphene sheets into nanoribbons in a well defined shape. Taking advantage of the atomic resolution of STM, armchair edged GNRs with width 2.5 nm and energy gap 0.5 eV have been reported [25] but the low throughput and low yield restrict the application of STM technique. Metallic nanoparticles can also be used as scissors in the lithographic-etching procedure. Particularly Fe [26] and Ni [27] nanoparticles have been thermally generated and used to cut down graphene into GNRs. Chemical vapor deposition method can also be used to fabricate GNRs directly where widths of 20 ~ 300 nm and thickness as of 2 ~ 40 layers are obtained. In other words, there is still need to improve and develop new fabrication techniques is still a challenge.

The potential application envisioned by using the GNRs depend on the large variety of electronic and magnetic properties: semiconducting with a wide range of band gaps, metallic, ferromagnetic, anti-ferromagnetic, half-metallic and half-semiconducting [28]. Those properties can be tailored by chemical modifications of the edge, as adsorbing appropriate atoms, or by substituting carbons with an appropriate host are some options to functionalize these materials. Therefore, these properties along with the

ballistic electronic transport and the high carrier mobility associated to these quasi-1D materials make them promising candidates for nanoelectronics and spintronics applications.

In order to achieve these potential applications it is essential to have a better understanding of the electronic structure of GNRs and have ability to control them. From a practical point of view, when nanoribbons are fabricated experimentally, they will have some structural defects. Vacancies and ad-atom defects are within the most probable ones [29]. These defects should be taken into account in practical aspects of the electronic transport in nanodevices based on graphene nanoribbons.

These defects are typically distributed along the nanoribbon and one has no control over their relative position. Depending on length and concentration one would, for example, expect to see a new transport regime known as localized regime [30]. Previous works in the group have shown that this regime gives rise to significant changes in the transport properties of nanoribbons [31].

1.4 Spin-orbit coupling in solids

The non-relativistic quantum mechanics theory accurately describes the interaction and motion of electrons and nuclei when the atoms treated are light (or the speed of the particles is small). If the atoms involved in the treatment are relatively heavy, e.g. transition metals atoms, relativistic effects become significant, especially for inner electrons due to the intensive confinement and high kinetic energy. From a fundamental physics point of view one such effect is known as the spin-orbit coupling (SO) and arises from the coupling between the intrinsic magnetic moment of the electron (proportional to its spin angular momentum) and the magnetic angular momentum around the nucleus (proportional to the electronic orbital angular momentum). This effect increases in the valence band with order¹ Z^2 .

Spin-orbit interaction has become one important direction in current spintronics where interesting phenomena, such as quantum spin Hall effect and quantum anomalous Hall effect, were predicted in graphene just based on its SO interactions [32, 33]. However, the intrinsic SO splitting in pure graphene or carbon nanotubes was found to be very weak (0.37 meV or smaller) [34, 35, 36]; not enough for practical applications. Therefore, it is important to explore the mechanism of SO interactions and yield large SO strength in those carbon systems under certain ambient environment. Also, the first spin injection measurements based on a non-local spin valve geometry [37] surprisingly revealed short spin relaxation times of about 100 - 200 ps. This contradiction opens a window to study the role of the intra-atomic spin-orbit interaction in the electronic

¹The so called spin-orbit correction to the Schrödinger equation can be obtained by expanding Dirac's equation in powers of α , the hyperfine constant.

properties of single and few layer graphene. In solids the spin-orbit effect manifests itself in the band structure.

The Rashba-Dresselhaus effect is a momentum dependent splitting of spin bands in two-dimensional condensed matter systems. The splitting is a combined effect of atomic spin-orbit coupling and the breaking of spacial symmetry. As a consequence, the energy bands become splitted in the wave vector direction.

Electronic devices are based on the ability to manipulate the electrons charge by the means of electric fields. Similarly, devices can be based on the manipulation of the spin degree of freedom.

Graphene exhibits weak spin-orbit (SO) interaction and ideally long spin lifetimes. As mentioned previously, experiments show spin relaxation times which are significantly smaller than those predicted by theory [38]. Thus it very important investigate which spin relaxation mechanism plays the major role in graphene. The Dyakonov-Perel [39] and the Elliot-Yafet [40][41] mechanisms are usually discussed in graphene. Experiments suggest that the main source of spin relaxation in single layer graphene is extrinsic, lending support to the Elliot-Yafet mechanism [38]. This means that impurities would play a key role both in graphene and graphene nanoribbons.

1.5 Spintronics

It is well known that the silicon based electronics era is reaching its limits because device miniaturization is facing the physical barriers where phenomena like tunnelling effects prevent the control of charge carriers. Therefore, new ways to fabricate devices that sort out these limitations are necessary. In this context several alternatives to build devices have appeared. We are interested in the field of spin electronics (spintronics) because it has promising advantages in futures electronics devices based on the fact that one exploits the electronic spin degree of freedom instead of the electronic charge.

In the so called field of spintronics there are three main challenges one needs to address before obtaining solid-state devices, namely: (1) the most effective way to polarize a spin system at the source, (2) obtaining long spin coherence times (small spin relaxation) during electronic transport, and (3) the ability to detect spin at the drain.

Carbon based nano-structures seem to be suitable candidates for spintronics because of the long spin relaxation time and large spin coherence of electrons. It is due to the fact that the organic molecules are composed of light atoms with small intrinsic spin-orbit interactions. Furthermore, the main element of organic compounds, i.e. carbon atom, has zero nuclear spin which results in a very small intrinsic spin-orbit interaction. Generating and injecting a spin-polarized current into graphene is of vital importance to the development of graphene-based spintronics. GNRs are theoretically predicted to possess a local magnetic moment at the zigzag edges, but a major limitation arises

in the presence of edge disorder and impurities which were shown to suppress this magnetic state. At the same time, impurities and defects might play an important role to the coherence of these systems. In particular, the presence of metal atoms can lead to significant spin-flip processes of conduction electrons due to the importance of the spin orbit interaction. These impurities are usually unavoidable and could deteriorate the spin current. So the key question that arises is how long can a spin-polarized current travel in a graphene nanoribbon and still conserve its polarization?.

1.6 Objectives

In general, we focused on the electronic structure and spin-polarized transport properties of armchair graphene nanoribbons with adsorbed transition metal (TM) atoms as impurities (Ni and Ir). We considered the spin-orbit effect. We have two main goals in this work: first, to understand the influence of the SO interaction over electronic structure and transport properties of a single adatom configuration (TM@AGNR) using a combination of density functional theory and non-equilibrium Green's functions (NEGFs). Second, to understand how the SO coupling affects the transport properties of a disordered system: a large number of impurities randomly distributed along the nanoribbon. This is done based on the single configuration studied previously by employing a recursive NEGFs method. For this last purpose we considered different setups. Finally, we compute the spin relaxation length at some specific energy regions of the disordered system.

The present work is organized as follow: In the first chapter a brief introduction was given on the subject. In the second chapter we explain the methodology used (i.e DFT and NEGFs without and with the spin-orbit coupling effects). In the third and fourth chapter we present our results for single defect and multiple defects structures, respectively. In the fifth chapter we give our conclusions to the project. Finally, we present the appendices containing additional results.

Chapter 2

Methodology

2.1 Density Functional Theory

2.1.1 The many body problem

Quantum mechanics is a theory for determining the processes occurring in atoms, molecules or nanoscale devices with dimensions from few Angstroms to hundreds of nanometers. Hence, in order to describe the behaviour of any many-electron system one must usually find an approximate solution of the non-relativistic time-independent Schrödinger Equation (SE)¹ [42]

$$\hat{H}\Psi = E\Psi, \quad (2.1)$$

where \hat{H} is the Hamiltonian operator of any system with M nuclei and N electrons given in atomic units ² by

$$\hat{H} = -\frac{1}{2} \sum_i \nabla_i^2 - \frac{1}{2} \sum_{\alpha} \frac{1}{m_{\alpha}} \nabla_{\alpha}^2 + \sum_i \sum_{i>j} \frac{1}{r_{ij}} - \sum_i \sum_{\alpha} \frac{Z_{\alpha}}{r_{\alpha i}} + \sum_{\alpha} \sum_{\beta>\alpha} \frac{Z_{\alpha}Z_{\beta}}{R_{\alpha\beta}}, \quad (2.2)$$

or

$$\hat{H} = \hat{T}_e + \hat{T}_n + \hat{V}_{ee} + \hat{V}_{en} + \hat{V}_{nn}, \quad (2.3)$$

¹As we will later see, relativistic effects are, in many cases important. Although not the topic of this dissertation so might be time dependent effects.

² $\hbar = m_e = e = 1/4\epsilon_0 = 1$

where the first, second, third, fourth and fifth terms of the right-hand side of equations 2.2 and 2.3 correspond to the operators for electronic and nuclear kinetic energy, the electron-electron interaction potential, electron-nuclei potential and nuclear repulsion potential respectively. As well as, $r_{i/j}$, $r_{\alpha/\beta}$, $Z_{\alpha/\beta}$ and m_{α} are the electron and nuclear coordinates, the nuclear charge and the nuclear mass respectively. The aim is to find the total energy levels ε_i as well as the wave function $\psi_i(\{\vec{r}_j\}, \{R_{\alpha}\})$ for electrons and nuclei.

2.1.2 The Born-Oppenheimer approximation

Finding a solution for this Hamiltonian is a difficult task but the key to achieve it is to rely on simplifications. One of these simplifications is known as the Born-Oppenheimer approximation (BO)[43] which is based on the fact that the electron speed is much higher than the nuclear speed, so nuclear motion can be almost static (from the electronic point of view) because the electrons can quickly adjust their state in response to any slower nuclear movement. A direct result of this approximation allow us to neglect the nuclear kinetic operator in the molecular Hamiltonian and split the total molecular wavefunction Ψ in two terms: one electronic and other nuclear. The electronic wavefunction will depend on the electronic coordinates r_i and parametrically on nuclear coordinates r_{α} while the nuclear wavefunction will be a function of nuclear coordinates only

$$\Psi = \Psi_e(\vec{r}_i; \vec{r}_{\alpha}) \Phi_{nucl}(\vec{r}_{\alpha}), \quad (2.4)$$

In this way, we will separate the equation for the electronic and nuclear particles. Since we are interested in the electronic formulation of the problem, we only write the electronic equation as

$$\hat{H}_e \Psi_e = E_e \Psi_e, \quad (2.5)$$

and the electronic Hamiltonian as

$$\hat{H}_e = \hat{T}_e + \hat{V}_{ee} + \hat{V}_{en}, \quad (2.6)$$

where \hat{V}_{nn} is nothing but a constant and \hat{H} becomes \hat{H}_e after applying the BO approach.³ There is still a huge problem: although we have somewhat eliminated the

³From now on we simply call our electronic Hamiltonian as \hat{H} unless we state the contrary.

nuclear degrees of freedom, one still needs to deal with a large number of electrons⁴.

2.1.3 The Hohenberg-Kohn theorems

In 1964, Hohenberg and Kohn (HK)[44] proved a couple of theorems that state the following:

Theorem I: *The external potential v_{ext} , and hence the total energy, is a unique functional of the electron density $\rho(\vec{r})$.*

It legitimizes the use of the electron density, instead of the wavefunction, as a basic variable, which for molecules with non-degenerated ground states, means that the wavefunction, the energy and the rest of the electronic properties can be determined uniquely by the electronic density $\rho(x, y, z)$. For this reason we can consider the energy E as a functional of the electronic density, $E[\rho]$.

Lets see more carefully this statement, considering as a starting point the electronic Hamiltonian of equation 2.6 which was obtained after applying the BO approach

$$\hat{H} = \hat{T}_e + \hat{V}_{en} + \hat{V}_{ee}, \quad (2.7)$$

also for practical purposes we rewrite \hat{V}_{en} as

$$\hat{V}_{en} = \hat{V}_{ext} = \sum_i v_{ext}(r_i), \quad (2.8)$$

where $v_{ext}(r_i) = -\sum_{\alpha} Z_{\alpha}/r_{i\alpha}$ is the external potential operator that acts over the i -th electron, as it has an external origin respect to the electron system. Hohenberg and Kohn demonstrated the electron density determines the external potential for a fixed number of electrons, so we assert the electron density contains all the necessary information to describe the system. Writing equation 2.7 in terms of expectation values and considering the HK theorem we have it in terms of the electronic density

$$E[\rho] = T[\rho] + V_{ext}[\rho] + V_{ee}[\rho], \quad (2.9)$$

with

⁴For this problem even a handful of electrons would be considered "large".

$$V_{ext} = \int \rho_0(r) v_{ext}(r) dr, \quad (2.10)$$

then we have

$$E[\rho] = T[\rho] + \int \rho(r) v_{ext}(r) dr + V_{ee}[\rho], \quad (2.11)$$

from this equation we only know the first term. Therefore now we have to call the second HK theorem :

Theorem II: *The ground state energy can be obtained variationally, hence the density that minimises the total energy is the exact ground state density.*
It means we can find the energy using the variational principle

$$E_0 \leq \int \rho(r) v_{ext}(r) dr + T[\rho] + V_{ee}[\rho] = E[\rho], \quad (2.12)$$

In other words for any trial electron density $\rho(r)$, which satisfies the necessary boundary conditions such as $\rho(r) \geq 0$ and $\int \rho(r) dr = N$ then $E[\rho]$ represents an upper bound to the true ground state energy E_0 . However, these theorems do not tell us the recipe for calculating E_0 from ρ_0 since we do not know the functional expression of $E[\rho]$.

2.1.4 The Kohn-Sham equations

Kohn and Sham (KS), in 1965[45], proposed that it is possible to reduce the many-body quantum problem to an exactly equivalent set of one-electron equations, solved self-consistently. They proposed a method that in principle allows us to obtain exact results.

The KS *ansatz* considers a fictitious reference system of N non-interacting electrons (referred to by the letter "s") that feel the same external potential $v_{ext}(r_i)$ and generates the same density as the interacting system

$$\rho_s = \rho_0, \quad (2.13)$$

therefore, by solving the set of equations for the system s it is possible (at least in principle) to obtain the exact density of the interacting system. This reference system has the Hamiltonian

$$\hat{H}_s = \sum_{i=1}^N \left[-\frac{1}{2} \nabla_i^2 + v_{ext}^{KS}(r_i) \right] = \sum_{i=1}^N h_i^{KS}, \quad (2.14)$$

where h_i^{ks} is the one electron KS Hamiltonian.

Due to the nature of the system s and taking into account the Pauli exclusion principle it is possible to use a ground state wavefunction for the reference system $\psi_{s,0}$ which can be described by the Slater Determinant (SD)[46] of the KS spin-orbitals φ_i^{KS} , where the spatial part $\phi_i^{KS}(r_i)$ of each spin-orbital is an eigenfunction of the one-electron KS Hamiltonian h_i^{KS} . Thus we have $\varphi_i^{KS} = \phi_i^{KS}(r_i)\sigma_i$ where σ_i is the spin function (\uparrow or \downarrow), finally leading us to the eigenvalue equation

$$h_i^{KS}\phi_i^{KS} = \varepsilon_i^{KS}\phi_i^{KS}, \quad (2.15)$$

where ε_i^{ks} is the KS energy.

Considering the reference system s it is possible to define the difference in kinetic energy between the real and fictitious system as

$$\Delta T[\rho] = T[\rho] - T_s[\rho] \quad (2.16)$$

where ΔT is the kinetic energy difference between the real and reference systems with the same electronic density. Similarly, we have the next difference

$$\Delta V_{ee}[\rho] = V_{ee}[\rho] - \frac{1}{2} \int \int \frac{\rho(r_1)\rho(r_2)}{r_{12}} dr_1 dr_2, \quad (2.17)$$

where r_{12} is the distance between the positions $r_1(x_1, y_1, z_1)$ and $r_2(x_2, y_2, z_2)$. The term $\frac{1}{2} \int \int \frac{\rho(r_1)\rho(r_2)}{r_{12}} dr_1 dr_2$ is the classical expression for the electronic repulsion potential energy assuming they are immersed in a continuous electronic charge distribution ρ .

Replacing equations 2.16 and 2.17 in equation 2.11, we have

$$E[\rho] = \int \rho(r)v_{ext}(r)dr + T_s[\rho] + \frac{1}{2} \int \int \frac{\rho(r_1)\rho(r_2)}{r_{12}} dr_1 dr_2 + \Delta T[\rho] + \Delta V_{ee}[\rho], \quad (2.18)$$

in this equation the functionals ΔT and ΔV_{ee} are unknown. From now on we define the exchange and correlation functional energy E_{xc} as follow

$$E_{xc}[\rho] = \Delta T[\rho] + \Delta V_{ee}[\rho], \quad (2.19)$$

here E_{xc} contains the kinetic correlation energy, the exchange energy (originated by the asymmetry requirement) and the Coulomb correlation energy, rewriting equation 2.18 as

$$E[\rho] = \int \rho(r)v_{ext}(r)dr + T_s[\rho] + \frac{1}{2} \int \int \frac{\rho(r_1)\rho(r_2)}{r_{12}}dr_1dr_2 + E_{xc}[\rho], \quad (2.20)$$

we note that except for the fourth term⁵, E_{xc} , in equation 2.20 the other three terms can be evaluated from the electronic density.

In order to solve equation 2.20 it is necessary to calculate the ground state density. At this point remember we defined $\rho_s(\vec{r})$ as $\rho_0(\vec{r})$. The electronic density of a system of N particles is calculated from the single SD of spin-orbitals as

$$\rho = \rho_s = \sum_{i=1}^N |\phi_i^{ks}|^2. \quad (2.21)$$

Now we have to rewrite each term of $E[\rho]$ as an explicit one-particle function of ρ thus we have

$$\int \rho(r)v_{ext}(r)dr = - \sum_{\alpha} Z_{\alpha} \int \frac{\rho(r_1)}{r_{1\alpha}}dr_1, \quad (2.22)$$

which is easy to calculate if we know $\rho(r_1)$. The kinetic energy of our reference system can be expressed using the spatial part of the orthonormal KS spin-orbitals as

$$T_s[\rho] = -\frac{1}{2} \sum_i \langle \phi_i^{ks}(1) | \nabla^2 | \phi_i^{ks}(1) \rangle, \quad (2.23)$$

Therefore equation 2.20 becomes

$$E_0 = - \sum_{\alpha} Z_{\alpha} \int \frac{\rho(r_1)}{r_{1\alpha}}dr_1 - \frac{1}{2} \sum_i \langle \phi_i^{ks}(1) | \nabla^2 | \phi_i^{ks}(1) \rangle + \int \int \frac{\rho(r_1)\rho(r_2)}{r_{12}}dr_1dr_2 + E_{xc}[\rho]. \quad (2.24)$$

⁵Although E_{xc} is functional of ρ , the expression to calculate it is unknown.

One more time we observe that it is possible to determine E_0 from the one-particle electronic density as long as one knows both the Kohn-Sham orbitals ϕ_i^{KS} and the exchange-correlation energy functional E_{xc} . The KS orbitals ϕ_i^{KS} are the orbitals for the reference system (fictitious system of non-interacting electrons) which do not have any physical meaning; its utility is to allow me to calculate the real density from equation 2.21.

The Kohn-Sham orbitals are obtained following the second HK theorem which state that we can find the ground state energy from the variational principle, namely, changing the density to minimize $E[\rho]$ or equivalently varying the orbitals ϕ_i^{KS} to find the density that satisfies the KS equation[47]

$$h^{KS}\phi_i^{KS}(1) = \varepsilon_i^{KS}\phi_i^{KS}(1), \quad (2.25)$$

$$\left[-\frac{1}{2}\nabla^2 + v_s(1)\right]\phi_i^{KS}(1) = \varepsilon_i^{KS}\phi_i^{KS}(1), \quad (2.26)$$

$$\left[-\frac{1}{2}\nabla_i^2 - \sum \frac{Z_\alpha}{r_{1\alpha}} + \int \frac{\rho(r_2)}{r_{12}}dr_2 + V_{xc}\right]\phi_i^{KS}(1) = \varepsilon_i^{KS}\phi_i^{KS}(1), \quad (2.27)$$

This exchange-correlation potential V_{xc} is the functional derivative of the exchange-correlation energy E_{xc} with respect to the density as is shown below

$$V_{xc}(r) = \frac{\delta E_{xc}[\rho(r)]}{\delta \rho(r)}. \quad (2.28)$$

This v_{xc} term contains all the remaining contributions to the potential that we do not know exactly.

In brief, the Kohn-Sham picture leads the quantum many-electron problem into a single electron problem, and dumps all the unknown part into the exchange-correlation term. Hence, it is necessary to find an approximate E_{xc} functional of high quality for our calculation. Some kinds of widely used E_{xc} functionals are presented in the next section.

2.1.5 Exchange-Correlations functionals

In order to have a formulation to describe the $E_{xc}[\rho]$ functional, three approximations generally used have been developed. The Local Density Approximation (LDA) [45],

the Local Spin Density Approximation (LSDA) and the Generalized Gradient Approximation (GGA) [48].

In the LDA formulation, the exchange-correlation energy per electron at each point \vec{r} in space is assumed to be the exchange-correlation energy per electron in a homogeneous electron gas (*Jellium* [49]) which has the same density as the electron gas considered at the same point in space. Its analytic expression is given by

$$E_{xc}^{LDA}[\rho] = \int \rho(r) \varepsilon_{xc}[\rho(r)] dr, \quad (2.29)$$

considering the functional derivative of E_{xc}^{LDA} we have

$$V_{xc}^{LDA} = \frac{\delta E_{xc}^{LDA}}{\delta \rho} = \varepsilon_{xc}[\rho] + \rho \frac{\partial \varepsilon_{xc}[\rho]}{\partial \rho}, \quad (2.30)$$

within this approximation it is possible to split E_{xc} into exchange ε_x and correlation ε_c parts

$$\varepsilon_{xc}[\rho] = \varepsilon_x[\rho] + \varepsilon_c[\rho], \quad (2.31)$$

the $\varepsilon_x(\rho)$ in the uniform electron gas model was given by Dirac, defined as

$$\varepsilon_x[\rho] = -\frac{3}{4} \left(\frac{3}{\pi} \right)^{1/3} [\rho(r)]^{1/3}, \quad (2.32)$$

whereas the correlation part $\varepsilon_c(\rho)$ was computed by Ceperly and Alder[50] using the Quantum Monte Carlo method. Therefore, it is possible to calculate the approximate value of E_{xc} and subsequently $V_{xc}[\rho]$.

In the LSDA formulation the electrons with different spin orientations are described by two different spatial orbitals $\phi_{i\uparrow}^{ks}$ and $\phi_{i\downarrow}^{ks}$. In this way we separate the total electronic density in a sum of spin-up and down electronic densities

$$\rho(r) = \rho^\uparrow(r) + \rho^\downarrow(r). \quad (2.33)$$

as a consequence, E_{xc} becomes a functional of both densities (or of the total density

and the magnetic moment $\rho_m(r) = \rho^\uparrow(r) - \rho^\downarrow(r)$

$$E_{xc}^{LSDA}[\rho^\uparrow, \rho^\downarrow] = \int \rho(r) \varepsilon_{xc}[\rho^\uparrow(r), \rho^\downarrow(r)] dr, \quad (2.34)$$

the procedure to obtain the LSDA is analogous to the LDA procedure. In fact, LDA is a special case of LSD for spin-compensated cases. The way we calculate the E_{xc} energy in LDA/LSD means we assume that the exchange-correlation potentials depend only on the local values of density. But the density in real systems, atoms and molecules, often varies drastically with r . Hence the next step is to supply information about how density changes with r .

In the GGA one tries to correct the LDA/LSDA approximation by introducing a dependence on the gradient of the density, in order to take into account the possible inhomogeneity of the electron gas. Thus the E_{xc} is given by

$$E_{xc}^{GGA}[\rho^\uparrow, \rho^\downarrow] = \int f[\rho^\uparrow(r), \rho^\downarrow(r), \nabla \rho^\uparrow(r), \nabla \rho^\downarrow(r)] dr. \quad (2.35)$$

where f is a functional of spin density and its gradient. As usual, it is possible to split E_{xc}^{GGA} in exchange and correlation parts: $E_{xc}^{GGA} = E_x^{GGA} + E_c^{GGA}$ and follow a procedure analogous to the LDA.

A note on the Kohn-Sham orbitals and eigenvalues

As we noted in the derivation of the Kohn-Sham scheme, the KS orbitals as well as the eigenvalues are not the real quasi-particle spectrum. This means that calculating any single-particle property (such as the band structure) is in principle not allowed. It has been noted, however that the KS eigenvalues do resemble the quasi-particle eigenstates thus it has become common practice to use them as such in electronic structure calculation. In particular in our transport calculations, the KS Hamiltonian will be considered a single particle Hamiltonian.

2.2 Spin-Orbit Density Functional Theory approach

In the previous section we reviewed a non-relativistic quantum mechanical prescription to solve the many-body problem. In particular we derived the density functional theory approach. This approach is useful to study systems of light atoms where the relativistic effects are negligible. In the case of systems composed of heavy atoms where the spin-orbit interaction becomes significant, it is necessary to include this effect in the

prescription in order to accurately describe the electronic structure. More accurately because in semiconductors the spin-orbit interaction is of paramount importance and responsible for splitting the edges of valence and conduction bands, the spin-relaxation time of electrons, the spin-flip processes and the spin relaxation length. Hereafter, we will describe the most important concepts that allow us to include the spin-orbit coupling in the DFT approach. These concepts are based in the original paper by L. Fernández-Seivane *et al.*[51].

The starting point of the so-called On-site approximation method is based on the extraction of the pseudo-potential ⁶(in the DFT approach), V_j from the solution of a single atom self-consistent all-electron Dirac equation is given by

$$\hat{V} = \sum_{j,m_j} |j, m_j\rangle V_j \langle j, m_j|, \quad (2.36)$$

where $j = l \pm \frac{1}{2}$ is the total angular momentum (includes both scalar and spin-orbit relativistic corrections) and $\langle j, m_j|$ are the total angular momentum states. In order to rewrite equation 2.35 in a fashion useful for non-relativistic pseudopotentials we can express it in terms of $\langle l, m|$ and eigenstates of z component of the Pauli spin matrices. In that way equation 2.35 becomes

$$\hat{V} = \hat{V}^{sc} + \hat{V}^{so} = \sum_{l,m} [\bar{V}_l \mathbb{I}_\sigma + \bar{V}_l^{so} \vec{L} \cdot \vec{S}] |l, m\rangle \langle l, m|, \quad (2.37)$$

where \mathbb{I}_σ is the 2x2 unit operator in the spin space, $\vec{L} \cdot \vec{S}$ is

$$\vec{L} \cdot \vec{S} = \frac{1}{2} \begin{pmatrix} \hat{L}_z & \hat{L}_- \\ \hat{L}_+ & -\hat{L}_z \end{pmatrix}, \quad (2.38)$$

and

$$\begin{aligned} \bar{V}_l &= \frac{1}{2l+1} [(l+1)V_{l+\frac{1}{2}} + lV_{l-\frac{1}{2}}], \\ \bar{V}_l^{so} &= \frac{2}{2l+1} [V_{l+\frac{1}{2}} - V_{l-\frac{1}{2}}], \end{aligned} \quad (2.39)$$

in this way the scalar part of pseudo-potential contains the non-relativistic and the

⁶The simulation takes into account only valence electrons leaving the core electrons contribution treated in the pseudo-potentials which can be constructed from DFT.

scalar relativistic corrections. The latter is already commonly included in pseudo-potentials. Because the Hamiltonian is a real matrix, the complex spherical harmonics vectors $|l, m\rangle$ are replaced by real spherical harmonics $|l, M\rangle$. Then, the pseudo-potential operator \hat{V} expressed in these new real representation becomes

$$\hat{V} = \hat{V}^{sc} + \hat{V}^{so} = \sum_{l,m} [\bar{V}_l \Pi_\sigma + \bar{V}_l^{so} \vec{L} \cdot \vec{S}] |l, M\rangle \langle l, M|, \quad (2.40)$$

where the unitary change of basis is given by

$$\begin{aligned} |l, M\rangle &= \frac{1}{\sqrt{2}} (|l, m\rangle + (-1)^m |l, -m\rangle) \\ |l, \bar{M}\rangle &= \frac{1}{\sqrt{2}i} (|l, m\rangle - (-1)^m |l, -m\rangle), \end{aligned} \quad (2.41)$$

This way, by including this term in the Hamiltonian it is possible to calculate the matrix elements for \hat{V}^{so} by calculating terms of the form $\langle l_i M_i | L_{\pm z} | l_j M_j \rangle$, the Clebsch-Gordan coefficients for the real spherical harmonics.

The Kohn-Sham Hamiltonian containing the spin-orbit pseudo-potential is

$$\hat{H} = \hat{T} + \hat{V}^{sc} + \hat{V}^{so} + \hat{V}^H + \hat{V}^{xc}, \quad (2.42)$$

where all the operators are 2x2 matrices in the spin space have the form

$$\hat{H} = \begin{bmatrix} \hat{H}^{\uparrow\uparrow} & \hat{H}^{\uparrow\downarrow} \\ \hat{H}^{\downarrow\uparrow} & \hat{H}^{\downarrow\downarrow} \end{bmatrix}, \quad (2.43)$$

The next step, in order to obtain a set of equations that let us implement a code based on this Kohn-Sham Hamiltonian (which includes the relativistic spin-orbit interaction term), is to use a suitable basis set following the LCAO⁷ method. Therefore, we consider the expansion of the non-collinear Kohn-Sham Hamiltonian wavefunction $|\psi_n\rangle$ in terms of localized orbitals $|\phi_i\rangle$ as

$$|\psi_n\rangle = \sum_i \begin{pmatrix} C_{n,i}^{\uparrow} \\ C_{n,i}^{\downarrow} \end{pmatrix} |\phi_i\rangle, \quad (2.44)$$

⁷Linear Combination of Atomic Orbitals.

where $|\phi_i\rangle$ is written as a product of radial and angular states centred at position \vec{d}_i $\phi_i(\vec{r} - \vec{d}_i) = \langle \vec{r} | \phi_i \rangle$ as follows

$$|\phi_i\rangle = |R_{n_i, l_i}\rangle \otimes |l_i, M_i\rangle, \quad (2.45)$$

In particular the spin-orbit matrix is given by

$$V_{ij}^{so} = \langle \phi_i | \hat{V}^{so} | \phi_j \rangle = \sum_{k, l_k, M_k} \langle \phi_i | \bar{V}_{l_k}^{so} \vec{L} \cdot \vec{S} | l_k, M_k \rangle \langle l_k, M_k | \phi_j \rangle, \quad (2.46)$$

where $\bar{V}_{l_k}^{so} = \bar{V}_l^{so}(\vec{r} - \vec{d}_k)$ and $|l_k, M_k\rangle$ are centred at the same position \vec{d}_k . At this point, equation 2.46 can be implemented as part of the KS Hamiltonian to treat systems that exhibit spin-orbit effects. Since it includes a great number of three central integrals, its calculation would be computationally expensive. For that reason, the *ansatz* of the On-site approximation is to simplify the matrix elements of equation 2.46 to one center integrals (on the same atom) based on the fact that \bar{V}^{so} has a very short-ranged radial part. This allows matrix elements to decay quickly with distance. Therefore, the on-site approximate version of equation 2.46 is

$$V_{ij}^{so} = \sum_{k, l_k, M_k} \langle R_{n_i, l_i} | \bar{V}_{l_k}^{so} | R_{n_j, l_j} \rangle \langle l_i, M_i | \vec{L} \cdot \vec{S} | l_k, M_k \rangle \langle l_k, M_k | l_j, M_j \rangle \quad (2.47)$$

$$\approx \langle R_{n_i, l_i} | \bar{V}_{l_i}^{so} | R_{n_j, l_i} \rangle \langle l_i, M_i | \vec{L} \cdot \vec{S} | l_i, M_j \rangle \delta_{l_i, l_j}, \quad (2.48)$$

where the angular part of the on-site matrix elements can be obtained analytically[51].

Then, projecting the KS equation $\hat{H}|\psi_n\rangle = E_n|\psi_n\rangle$ on such orbitals we obtain

$$\begin{bmatrix} H_{ij}^{\uparrow\uparrow} - E_n S_{ij} & H_{ij}^{\uparrow\downarrow} \\ H_{ij}^{\downarrow\uparrow} & H_{ij}^{\downarrow\downarrow} - E_n S_{ij} \end{bmatrix} \begin{bmatrix} C_{n,i}^{\uparrow} \\ C_{n,i}^{\downarrow} \end{bmatrix} = 0, \quad (2.49)$$

where $H_{ij}^{\sigma\sigma}$ and S_{ij} are the matrix elements⁸ of the Hamiltonian and overlap matrix, respectively.

⁸ $H_{ij}^{\sigma\sigma} = \langle \phi_i | H^{\sigma\sigma} | \phi_j \rangle$ and $S_{ij} = \langle \phi_i | \phi_j \rangle$

Finally, the electronic density expressed in the LCAO basis is

$$\rho(\vec{r}) = \sum_n f_n \psi_n(\vec{r}) \psi_n(\vec{r})^\dagger = \sum_{i,j} \phi_i(\vec{r} - \vec{d}_i) \phi_j^*(\vec{r} - \vec{d}_j) \rho_{ij}, \quad (2.50)$$

where f_n is a KS eigenstate distribution and ρ_{ij} is given by

$$\rho_{ij}^{\sigma\sigma'} = \sum_n f_n C_{n,i}^\sigma C_{n,j}^{\sigma'*}, \quad (2.51)$$

and electronic contribution to the total energy expressed as a sum of band structure (BS) contribution and double-counting corrections given by

$$E_e^{BS} = \sum_n f_n \langle \psi_n | \hat{H} | \psi_n \rangle = \sum_{i,j,\sigma,\sigma'} H_{ij}^{\sigma\sigma'} \rho_{ji}^{\sigma'\sigma} \quad (2.52)$$

and the spin-orbit contribution to the total energy is therefore

$$E^{so} = Tr \sum_{i,j} V_{ij}^{so} \rho_{ji} \quad (2.53)$$

Finally, we would also have to express the spin-orbit contribution to the force but in the on-site approach it does not give rise to an explicit contribution to forces.

Thus we have presented a framework for calculating the electronic structure of many-electron system including the effect of spin-orbit. Although such an effect is noticeable in the electronic structure (bands) of the systems under consideration, corrections to the total energy are extremely small (less than 1 meV) and are thus unreliable for pseudo-potential codes, this means we will ignore such effects when obtaining the relaxed structures.

2.3 Electronic transport: Non-equilibrium Green's function (NEGF) method

2.3.1 Single defect

In order to obtain the transmission coefficients in terms of the retarded Green's functions for our system of interest, which is the main goal of this section, we use a typical

configuration for atomic scale scattering problems [52] shown in figure 2.1. It is a central region (scattering region called extended molecule, EM) sandwiched by two electrodes (left and right leads). The leads are defect-free periodic structures in one direction (semi-infinite leads). It is also built in such a way that each unit cell interacts only with its nearest neighbours. Finally, we assume that the transport problem will be formulated in terms of a linear combination of atomic orbitals (LCAO).

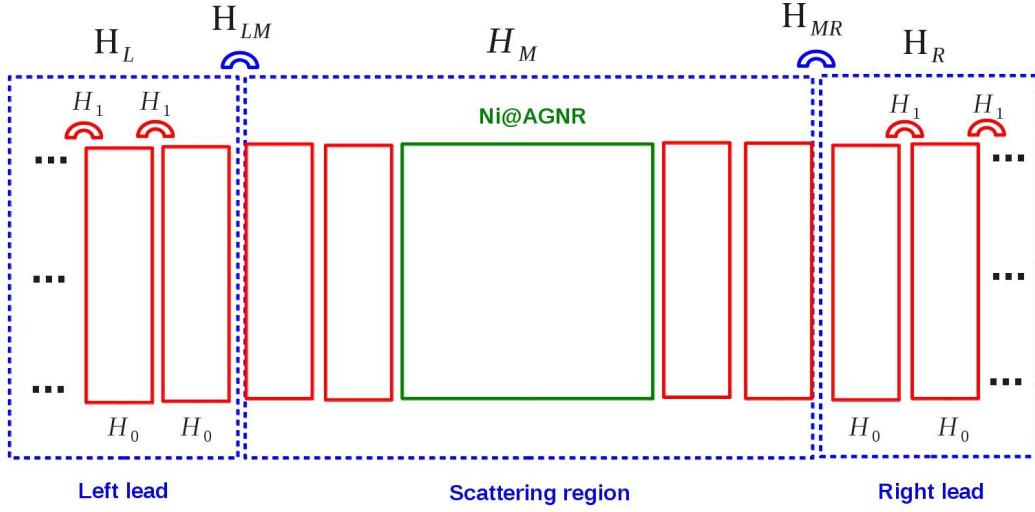


Figure 2.1: Schematic representation for transport problem at nanoscale. The central scattering region is described by the Hamiltonian H_M , H_{RM} (H_{LM}) correspond to coupling between EM and right (left) leads, H_0 correspond to unit cell of lead and H_1 correspond to coupling between two adjacent unit cells of the lead.

From a quantum mechanical point of view we can describe the total Hamiltonian \mathcal{H} ⁹ for the scattering configuration in terms of their constituent Hamiltonian elements expressed as

$$\mathcal{H} = \begin{pmatrix} \ddots & \vdots & \vdots & \vdots & \vdots & \vdots & \vdots & \vdots & \vdots & \vdots & \vdots & \ddots \\ \cdots & 0 & H_{-1} & H_0 & H_1 & 0 & \cdot & \cdot & \cdot & \cdot & \cdot & \cdots \\ \cdots & \cdot & 0 & H_{-1} & H_0 & H_{LM} & 0 & \cdot & \cdot & \cdot & \cdot & \cdots \\ \cdots & \cdot & \cdot & 0 & H_{ML} & H_M & H_{MR} & 0 & \cdot & \cdot & \cdot & \cdots \\ \cdots & \cdot & \cdot & \cdot & 0 & H_{RM} & H_0 & H_1 & 0 & \cdot & \cdot & \cdots \\ \cdots & \cdot & \cdot & \cdot & \cdot & 0 & H_{-1} & H_0 & H_1 & 0 & \cdot & \cdots \\ \cdot & \cdot & \vdots & \vdots & \vdots & \vdots & \vdots & \vdots & \vdots & \vdots & \vdots & \ddots \end{pmatrix}, \quad (2.54)$$

⁹Calligraphic letter refer to infinite matrix and capital letter for finite one.

where H_M describes the EM, H_{RM} (H_{LM}) corresponds to coupling between EM and right (left) lead, H_0 correspond to unit cell of lead and H_1 ¹⁰ corresponds to coupling between two adjacent unit cells of the lead.

We can write \mathcal{H} as a set of infinite Hamiltonians that comprise the EM and its interaction with the right (left) leads as

$$\mathcal{H} = \begin{pmatrix} \mathcal{H}_L & \mathcal{H}_{LM} & 0 \\ \mathcal{H}_{ML} & H_M & \mathcal{H}_{MR} \\ 0 & \mathcal{H}_{RM} & \mathcal{H}_R \end{pmatrix}, \quad (2.55)$$

where

$$\mathcal{H}_L = \begin{pmatrix} \ddots & \vdots & \vdots & \vdots \\ \cdots & H_{-1} & H_0 & H_1 \\ \cdots & 0 & H_{-1} & H_0 \end{pmatrix}; \quad \mathcal{H}_R = \begin{pmatrix} H_0 & H_1 & 0 & \cdots \\ H_{-1} & H_0 & H_1 & \cdots \\ \vdots & \vdots & \vdots & \ddots \end{pmatrix}, \quad (2.56)$$

and

$$\mathcal{H}_{LM} = \begin{pmatrix} \vdots \\ 0 \\ H_{LM} \end{pmatrix} \quad \mathcal{H}_{RM} = \begin{pmatrix} H_{RM} \\ 0 \\ \vdots \end{pmatrix}. \quad (2.57)$$

We are facing an infinite-dimensional problem which is impossible to solve by traditional diagonalization methods. Therefore, the problem can be solved if one calculates the retarded Green's function for the total system by solving the Green's function[53] equation

$$[\epsilon^+ \mathcal{S} - \mathcal{H}] \mathcal{G}^R(E) = \mathcal{I}, \quad (2.58)$$

where E is the energy, \mathcal{I} is the infinite identity matrix and $\epsilon^+ = \lim_{\delta \rightarrow 0^+} E + i\delta$.

¹⁰If the time-reversal symmetry is preserved then $H_1 = H_1^\dagger$, $H_{ML} = H_{LM}^\dagger$ and $H_{MR} = H_{RM}^\dagger$.

Using the block-diagonal structure of \mathcal{H} (2.54) and the overlap matrix¹¹ we have equation 2.57 in the form

$$\begin{pmatrix} \epsilon^+ \mathcal{S}_L - \mathcal{H}_L & \epsilon^+ \mathcal{S}_{LM} - \mathcal{H}_{LM} & 0 \\ \epsilon^+ \mathcal{S}_{ML} - \mathcal{H}_{ML} & \epsilon^+ S_M - H_M & \epsilon^+ \mathcal{S}_{MR} - \mathcal{H}_{MR} \\ 0 & \epsilon^+ \mathcal{S}_{RM} - \mathcal{H}_{RM} & \epsilon^+ S_R - \mathcal{H}_R \end{pmatrix} \begin{pmatrix} \mathcal{G}_L^R & \mathcal{G}_{LM}^R & \mathcal{G}_{RL}^R \\ \mathcal{G}_{ML}^R & G_M^R & \mathcal{G}_{MR}^R \\ \mathcal{G}_{LR}^R & \mathcal{G}_{RM}^R & \mathcal{G}_R^R \end{pmatrix} = \begin{pmatrix} \mathcal{I} & 0 & 0 \\ 0 & I_M & 0 \\ 0 & 0 & \mathcal{I} \end{pmatrix}, \quad (2.59)$$

where the retarded Green's function $\mathcal{G}^R(E)$ has been expressed in terms of infinite blocks describing the left \mathcal{G}_L^R (right \mathcal{G}_R^R) lead, the left \mathcal{G}_{LM}^R (right \mathcal{G}_{RM}^R) coupling with the EM, the interaction between left (right) leads \mathcal{G}_{LR}^R and for the extended molecule the finite G_M^R .

Considering there are no changes to the electronic structure of the charge reservoirs coming from neither the coupling to the EM nor through the external bias, we can treat the leads as effective interactions (self energies Σ_L^R and Σ_R^R). Therefore G_M^R is formally the Green's function associated to an effective Hamiltonian $H_{eff} = H_M + \Sigma_L^R + \Sigma_R^R$. Thus, the final expression for G_M^R is

$$G_M^R(E) = [\epsilon^+ S_M - H_M - \Sigma_L^R(E) - \Sigma_R^R(E)]^{-1}, \quad (2.60)$$

and the expression for the self energies [53] are given by

$$\Sigma_L^R(E) = (\epsilon^+ S_{ML} - H_{ML}) G_L^{0R}(E) (\epsilon^+ S_{LM} - H_{LM}), \quad (2.61)$$

$$\Sigma_R^R(E) = (\epsilon^+ S_{MR} - H_{MR}) G_R^{0R}(E) (\epsilon^+ S_{RM} - H_{RM}), \quad (2.62)$$

where G_L^{0R} and G_R^{0R} are the retarded surface Green's functions of the left (right) semi-infinite leads corresponding to the unit cell adjacent to the EM.

¹¹The overlap matrix \mathcal{S} has the same structure of \mathcal{H} therefore we use the notation S_0 , S_1 , \mathcal{S}_{LM} , \mathcal{S}_{RM} , \mathcal{S}_L , \mathcal{S}_R and \mathcal{S}_M .

Because the information that comprises the electronic structure of a central region attached to left and right leads are contained in the retarded Green's functions G_M^R , now we can define the total transmission coefficient $T(E)$ using the Buttiker-Landauer-like formula [54]

$$T(E) = \text{Tr}[\Gamma_L G_M^{R\dagger} \Gamma_R G_M^R], \quad (2.63)$$

where

$$\Gamma_L(E) = i[\Sigma_L^R(E) - \Sigma_L^R(E)^\dagger], \quad (2.64)$$

$$\Gamma_R(E) = i[\Sigma_R^R(E) - \Sigma_R^R(E)^\dagger], \quad (2.65)$$

$\Gamma_{L/R}(E)$ are the coupling matrices. This transmission coefficient can be related to the conduction by the Fisher-Lee [55] formula

$$G = \lim_{V \rightarrow 0} \frac{2e^2}{\hbar} T(E_F), \quad (2.66)$$

where the factor 2 comes from the spin degeneracy and we can define a quantum of conductance $G_0 = \frac{2e^2}{h}$ which depends only on fundamental quantities [55]

Spin polarized scheme

In order to generalize the Green's functions method described previously for problems where non-collinear spins are important (in particular the spin-orbit interaction) we need to extend the matrices in the spin space, namely each matrix element from the non-spin formalism becomes a two-by-two matrix that specifies the spin-up, spin-down and the coupling between them.¹² For example any operator A will have the form

$$A_{ij}^{\sigma\sigma'} \longrightarrow \begin{pmatrix} A_{ij}^{\uparrow\uparrow} & A_{ij}^{\uparrow\downarrow} \\ A_{ij}^{\downarrow\uparrow} & A_{ij}^{\downarrow\downarrow} \end{pmatrix}, \quad (2.67)$$

¹²Except for the overlap matrix where the coupling between spin-up and spin-down vanishes.

Therefore the Green's functions in spin space is given by

$$G = \begin{pmatrix} G^{\uparrow\uparrow} & G^{\uparrow\downarrow} \\ G^{\downarrow\uparrow} & G^{\downarrow\downarrow} \end{pmatrix}, \quad (2.68)$$

where¹³

$$G^{\uparrow\uparrow} = \begin{pmatrix} ES_L^{\uparrow\uparrow} - H_L^{\uparrow\uparrow} - \Sigma_L^{\uparrow\uparrow} & ES_{LM}^{\uparrow\uparrow} - H_{LM}^{\uparrow\uparrow} & 0 \\ ES_{ML}^{\uparrow\uparrow} - H_{ML}^{\uparrow\uparrow} & ES_M^{\uparrow\uparrow} - H_M^{\uparrow\uparrow} & ES_{MR}^{\uparrow\uparrow} - H_{MR}^{\uparrow\uparrow} \\ 0 & ES_{RM}^{\uparrow\uparrow} - H_{RM}^{\uparrow\uparrow} & ES_R^{\uparrow\uparrow} - H_R^{\uparrow\uparrow} - \Sigma_R^{\uparrow\uparrow} \end{pmatrix}, \quad (2.69)$$

$$G^{\uparrow\downarrow} = \begin{pmatrix} -H_L^{\uparrow\downarrow} - \Sigma_L^{\uparrow\downarrow} & -H_{LM}^{\uparrow\downarrow} & 0 \\ -H_{ML}^{\uparrow\downarrow} & -H_M^{\uparrow\downarrow} & -H_{MR}^{\uparrow\downarrow} \\ 0 & -H_{RM}^{\uparrow\downarrow} & -H_R^{\uparrow\downarrow} - \Sigma_R^{\uparrow\downarrow} \end{pmatrix}, \quad (2.70)$$

$$G^{\downarrow\uparrow} = \begin{pmatrix} -H_L^{\downarrow\uparrow} - \Sigma_L^{\downarrow\uparrow} & -H_{LM}^{\downarrow\uparrow} & 0 \\ -H_{ML}^{\downarrow\uparrow} & -H_M^{\downarrow\uparrow} & -H_{MR}^{\downarrow\uparrow} \\ 0 & -H_{RM}^{\downarrow\uparrow} & -H_R^{\downarrow\uparrow} - \Sigma_R^{\downarrow\uparrow} \end{pmatrix}, \quad (2.71)$$

$$G^{\downarrow\downarrow} = \begin{pmatrix} ES_L^{\downarrow\downarrow} - H_L^{\downarrow\downarrow} - \Sigma_L^{\downarrow\downarrow} & ES_{LM}^{\downarrow\downarrow} - H_{LM}^{\downarrow\downarrow} & 0 \\ ES_{ML}^{\downarrow\downarrow} - H_{ML}^{\downarrow\downarrow} & ES_M^{\downarrow\downarrow} - H_M^{\downarrow\downarrow} & ES_{MR}^{\downarrow\downarrow} - H_{MR}^{\downarrow\downarrow} \\ 0 & ES_{RM}^{\downarrow\downarrow} - H_{RM}^{\downarrow\downarrow} & ES_R^{\downarrow\downarrow} - H_R^{\downarrow\downarrow} - \Sigma_R^{\downarrow\downarrow} \end{pmatrix}. \quad (2.72)$$

This way if we consider that there is no SO interaction in the electrodes then we can use $\Sigma_L^{\uparrow\downarrow} = \Sigma_L^{\downarrow\uparrow} = \Sigma_R^{\uparrow\downarrow} = \Sigma_R^{\downarrow\uparrow} = 0$ from the self energies, Γ_L , Γ_R and the Green's functions described before in the spin-space we also can write the transmission coefficients in the same spin-space by using the analogous formalism for the spin-degenerate case and define the total transmission coefficients as

¹³We assume the basis is the same so $S_L^{\uparrow\uparrow} = S_L^{\downarrow\downarrow}$.

$$T(E) = T^{\uparrow\uparrow}(E) + T^{\uparrow\downarrow}(E) + T^{\downarrow\uparrow}(E) + T^{\downarrow\downarrow}(E), \quad (2.73)$$

where

$$\begin{aligned} T^{\uparrow\uparrow}(E) &= Tr[\Gamma_L^{\uparrow\uparrow}(G_M^{\uparrow\uparrow})^\dagger \Gamma_R^{\uparrow\uparrow} G_M^{\uparrow\uparrow}], \\ T^{\uparrow\downarrow}(E) &= Tr[\Gamma_L^{\uparrow\uparrow}(G_M^{\uparrow\downarrow})^\dagger \Gamma_R^{\uparrow\uparrow} G_M^{\uparrow\downarrow}], \\ T^{\downarrow\uparrow}(E) &= Tr[\Gamma_L^{\downarrow\downarrow}(G_M^{\downarrow\uparrow})^\dagger \Gamma_R^{\downarrow\downarrow} G_M^{\downarrow\uparrow}], \\ T^{\downarrow\downarrow}(E) &= Tr[\Gamma_L^{\downarrow\downarrow}(G_M^{\downarrow\downarrow})^\dagger \Gamma_R^{\downarrow\downarrow} G_M^{\downarrow\downarrow}]. \end{aligned} \quad (2.74)$$

We can note that each of these terms can be associated by a type of scattering process. The terms $T^{\uparrow\uparrow}$ and $T^{\downarrow\downarrow}$ are spin conserving and $T^{\uparrow\downarrow}$ and $T^{\downarrow\uparrow}$ are spin-flip probabilities.

2.3.2 Multiple defects

The treatment for the problem of a disordered system[56] is similar to the previous one (single defect). In principle we can use the same equations to obtain the electronic transport properties of any 1-D device if we know its Hamiltonian H_M . However, our disordered problem entails the inversion of a Hamiltonian with 100's of thousands of degrees of freedom. Brute force inversion would simply be impossible.

The alternative to tackle a disordered problem is to assume that the large 1-D device (disordered system) is comprised of a large number of different blocks as is depicted in the figure 2.2¹⁴ where the on-site Hamiltonian H_i correspond to the i -th block and the terms $V_{i,j}$ correspond to the coupling between the two adjacent blocks¹⁵. Also, as usual, our huge scattering region H_M is attached to two electrodes represented by the left (right) self energies Σ_L and Σ_R .

Due to the use of a large numbers of blocks randomly distributed and the tridiagonal nature of H_M (equation 2.74) it is possible to apply a procedure known as Decimation[57] which is similar to the Gaussian elimination.

In order to visualize the procedure we write down the Hamiltonian for the central region

¹⁴We assume that the disordered system is assembled by using different box size and colors.

¹⁵In our particular case, these blocks are a set of single defect scattering regions (Fig.2.1) and pristine units.

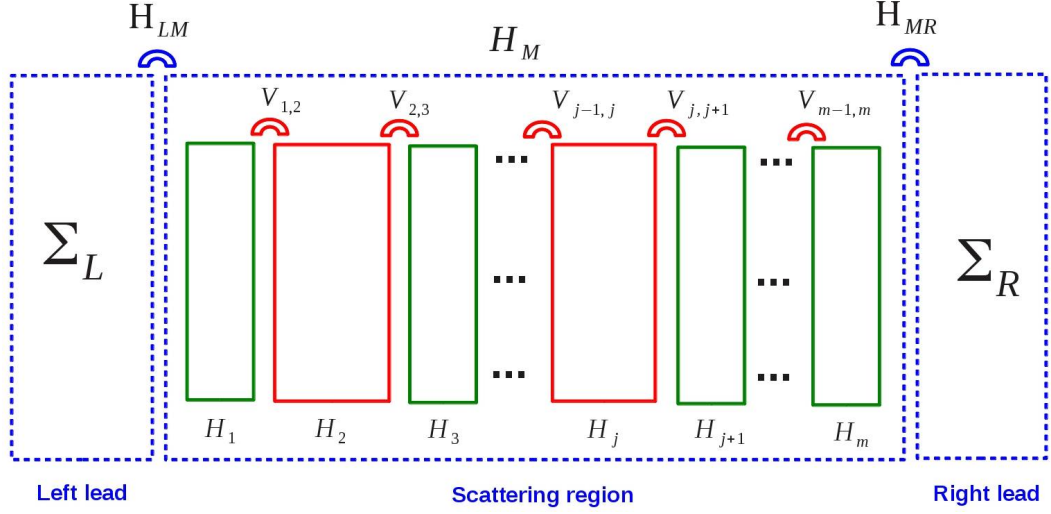


Figure 2.2: Schematic representation for a multiple defects transport problem at nano-scale. We assumed that the device was built by using different blocks (red and green) and each block is described by H_i and by the coupling V_{ij} .

$$H_M = \begin{pmatrix} H_1 & V_{1,2} & 0 & 0 & 0 & \cdots & 0 \\ V_{2,1} & H_2 & V_{2,3} & \cdots & 0 & \cdots & 0 \\ 0 & V_{3,2} & \ddots & V_{j-1,j} & 0 & \cdots & 0 \\ \vdots & \vdots & V_{j,j-1} & H_j & V_{j,j+1} & \cdots & \vdots \\ 0 & 0 & 0 & V_{j+1,j} & \ddots & \ddots & 0 \\ \vdots & \vdots & \vdots & \vdots & \ddots & H_{m-1} & V_{m-1,m} \\ 0 & 0 & 0 & 0 & 0 & V_{m,m-1} & H_m \end{pmatrix}. \quad (2.75)$$

While the Hamiltonian H_M is clearly block-tridiagonal the same can not be said about the Green's function which is generally a dense matrix. Therefore, the complete Green's function equation for our disordered system is given by¹⁶

¹⁶To simplify we redefine $\tilde{H}_i = [ES_i - H_i]$ and $\tilde{V}_{i,j} = [ES_{i,j} - H_{i,j}]$.

$$\begin{pmatrix}
\bar{H}_1 - \Sigma_L & \bar{V}_{1,2} & 0 & \cdots & 0 & \cdots & 0 & 0 \\
\bar{V}_{2,1} & \bar{H}_2 & \bar{V}_{2,3} & \cdots & 0 & \cdots & 0 & 0 \\
0 & \bar{V}_{3,2} & \bar{H}_3 & \ddots & \vdots & 0 & \cdots & 0 \\
\vdots & \vdots & \ddots & \ddots & \bar{V}_{j-1,j} & 0 & \vdots & \vdots \\
0 & 0 & \cdots & \bar{V}_{j,j-1} & \bar{H}_j & \bar{V}_{j,j+1} & \cdots & 0 \\
\vdots & \vdots & 0 & 0 & \bar{V}_{j+1,j} & \ddots & \ddots & \vdots \\
0 & 0 & 0 & \cdots & \vdots & \ddots & \bar{H}_{m-1} & \bar{V}_{m-1,m} \\
0 & 0 & 0 & \cdots & 0 & \cdots & \bar{V}_{m,m-1} & \bar{H}_m - \Sigma_R
\end{pmatrix} \times$$

$$\begin{pmatrix}
\mathcal{G}_1 & \mathcal{G}_{1,2} & \mathcal{G}_{1,3} & \cdots & \mathcal{G}_{1,j} & \cdots & \mathcal{G}_{1,m-1} & \mathcal{G}_{1,m} \\
\mathcal{G}_{2,1} & \mathcal{G}_2 & \mathcal{G}_{2,3} & \cdots & \mathcal{G}_{2,j} & \cdots & \mathcal{G}_{2,m-1} & \mathcal{G}_{2,m} \\
\mathcal{G}_{3,1} & \mathcal{G}_{3,2} & \mathcal{G}_3 & \ddots & \vdots & \mathcal{G}_{3,j} & \cdots & \mathcal{G}_{3,m} \\
\vdots & \vdots & \ddots & \ddots & \mathcal{G}_{j-1,j} & \mathcal{G}_{j-1,j+1} & \vdots & \vdots \\
\mathcal{G}_{j,1} & \mathcal{G}_{j,2} & \cdots & \mathcal{G}_{j,j-1} & \mathcal{G}_j & \mathcal{G}_{j,j+1} & \cdots & \mathcal{G}_{j,m} \\
\vdots & \vdots & \mathcal{G}_{j+1,3} & \mathcal{G}_{j+1,j-1} & \mathcal{G}_{j+1,j} & \ddots & \ddots & \vdots \\
\mathcal{G}_{m-1,1} & \mathcal{G}_{m-1,2} & \mathcal{G}_{m-1,3} & \cdots & \vdots & \ddots & \mathcal{G}_{m-1} & \mathcal{G}_{m-1,m} \\
\mathcal{G}_{m,1} & \mathcal{G}_{m,2} & \mathcal{G}_{m,3} & \cdots & \mathcal{G}_{m,j} & \cdots & \mathcal{G}_{m,m-1} & \mathcal{G}_m
\end{pmatrix}$$

$$= \begin{pmatrix}
I & 0 & 0 & \cdots & 0 & \cdots & 0 & 0 \\
0 & I & 0 & \cdots & 0 & \cdots & 0 & 0 \\
0 & 0 & I & \ddots & \vdots & 0 & \cdots & 0 \\
\vdots & \vdots & \ddots & \ddots & 0 & 0 & \vdots & \vdots \\
0 & 0 & \cdots & 0 & I & 0 & \cdots & 0 \\
\vdots & \vdots & 0 & 0 & 0 & \ddots & \ddots & \vdots \\
0 & 0 & 0 & \cdots & \vdots & \ddots & I & 0 \\
0 & 0 & 0 & \cdots & 0 & \cdots & 0 & I
\end{pmatrix}, \tag{2.76}$$

The decimation procedure comprises the Gaussian elimination starting from the second line all the way to the (m-1)-th line recursively. After applying the procedure [57] (m-2) times, the reduced Green's function becomes

$$\begin{pmatrix} H_{1,1}^{eff} - \Sigma_L & H_{1,m}^{eff} \\ H_{m,1}^{eff} & H_{m,m}^{eff} - \Sigma_R \end{pmatrix} \begin{pmatrix} \mathcal{G}_{1,1} & \mathcal{G}_{1,m} \\ \mathcal{G}_{m,1} & \mathcal{G}_{m,m} \end{pmatrix} = \begin{pmatrix} I & 0 \\ 0 & I \end{pmatrix}, \quad (2.77)$$

where

$$\begin{aligned} H_{1,1}^{eff} &= \bar{H}_1^{m-2} = \bar{H}_1 - \sum_{i=1}^{m-2} \bar{V}_{1,i+1}^{i-1} [\bar{H}_{i+1}^{i-1}]^{-1} \bar{V}_{i+1,1}^{i-1}, \\ H_{m,m}^{eff} &= \bar{H}_m^{m-2} = \bar{H}_m - \bar{V}_{m,m-1}^0 [\bar{H}_{m-1}^{m-3}]^{-1} \bar{V}_{m-1,m}^0, \\ H_{1,m}^{eff} &= \bar{V}_{1,m}^{m-2} = -\bar{V}_{1,m-1}^{m-3} [H_{m-1}^{m-3}]^{-1} \bar{V}_{m-1,m}^0, \end{aligned} \quad (2.78)$$

In summary, we can notice that the blocks of interest to calculate transport properties are those that effectively couple both electrodes. Thus, in terms of Green's function we only need to calculate the element $\mathcal{G}_{1,m}$ for a complete description of transport properties. Hence, The transmission coefficient for a disordered system is given by

$$T(E) = Tr[\Gamma_L \mathcal{G}_{1,m}^\dagger \Gamma_R \mathcal{G}_{1,m}], \quad (2.79)$$

Furthermore, for the case of non-collinear spin systems a similar expansion of matrices in the spin-space has been applied¹⁷.

Finally, we will define some additional equations used in this work. The concentration of Ni adatoms on the disordered device were calculated using

$$[Ni] = \frac{N_D \cdot A_{Ni}}{N_D \cdot (A_C \cdot n_C^D + A_H \cdot n_H^D) + (N_T - N_D)(A_C \cdot n_C^P + A_H \cdot n_H^P)}, \quad (2.80)$$

where:

N_D : total number of defects,

N_T : total number of blocks,

n_C^D : number of carbon atoms in the defect block,

¹⁷For simplicity we avoid to include all the equations in spin-space for a disordered system which is implemented in the SMEAGOL[53] package.

n_H^D : number of hydrogen atoms in the defect block,
 n_C^P : number of carbon atoms in the pristine block (electrode block),
 n_H^P : number of hydrogen atoms in the pristine block, and
 A_E : atomic mass of atom E (E: C, H, Ni).

In figure 2.3 we can see a typical arrangement of the disordered system used in our calculations. The number of atoms in the systems considered here range from 3255 to 35130. The length of the disordered device was obtained from

$$L = N_D \cdot L_D + (N_T - N_D)(L_P), \quad (2.81)$$

where L_D and L_P are the length of defect and pristine blocks, respectively.

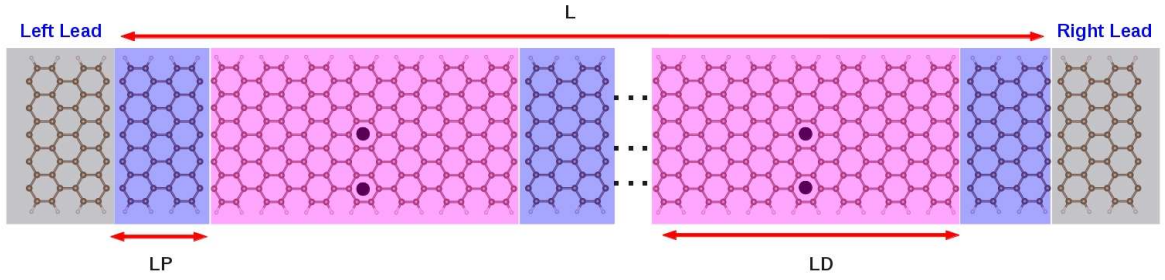


Figure 2.3: Disordered system scheme where the single defects are randomly separated by pristine segments. L is the total length of the device, L_D is the defect length and L_P is the pristine segment length.

The Total conductance is obtained by using

$$T_{Total}(E, L) = T^{\uparrow\uparrow} + T^{\uparrow\downarrow} + T^{\downarrow\downarrow} + T^{\downarrow\uparrow}, \quad (2.82)$$

where $T^{\uparrow\uparrow}$ is the spin-conserved transmission probability and $T^{\uparrow\downarrow}$ is the spin-flip transmission probability.

Finally, the polarization P is defined by the equation

$$P(E, L) = \frac{T^{\uparrow\uparrow}(E) - T^{\uparrow\downarrow}(E)}{T^{\uparrow\uparrow}(E) + T^{\uparrow\downarrow}(E)}, \quad (2.83)$$

As we can notice, the polarization gives an indication of the degree of coherence as one increases the device length a larger number of scattering events should yield

$$\lim_{L \rightarrow \infty} P(E, L) = 0, \quad (2.84)$$

Chapter 3

Results and discussions I : Single defect

In this chapter we will describe and discuss the effect of the relativistic spin-orbit interaction on the electronic structure and spin-polarized electron transport calculations of individual metal transition atoms adsorbed on armchair graphene nanoribbons (called hereafter single defect system). In particular, we used Nickel and Iridium atoms.

We will start this chapter describing and discussing the structural relaxation results for the pristine and single defect systems. Then, we will select the most stable and symmetric single defect system - after relaxation in both cases, and we will present and discuss the electronic structure results, namely, band structures, DOS and PDOS. Finally, the transport results of those arrangements will be presented and discussed.

3.1 Geometry relaxation

The chosen pristine AGNR is the 11-AGNR¹ [58]. For the sake of simplicity, we will use the simple notation AGNR throughout this work. It is composed of three unit cells where the periodicity is along the Z direction, as shown in figure 3.1. The unit cell is the shadow box with lattice vector \vec{a} , lattice constant of 4.33 Å and 1.238 nm wide. Each unit cell was passivated with 2 Hydrogen atoms at the edges, consequently it contains 22 Carbon and 4 Hydrogen atoms.

¹In agreement with standard notation, it has 11 carbon atoms in width.

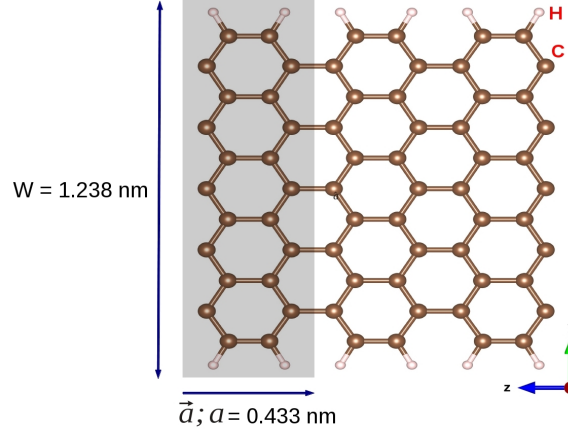


Figure 3.1: 11-AGNR type of ribbon with 1.238 nm of width and composed by three unit cells with lattice vector \vec{a} and lattice constant 4.33 Å.

Relative to each hexagon the adsorbed atoms were placed in three possible adsorption sites on the pristine AGNR, namely: the Hollow (H), Top (T) and Bridge (B) sites which are in positions above the center of the hexagon, the carbon atom and the carbon-carbon bond, respectively (as we can see in figure 3.2). The notation used in this work is Ni@AGNR- n (Ir@AGNR- n) which means n - th configuration of Ni (Ir) atom adsorbed on the pristine AGNR.

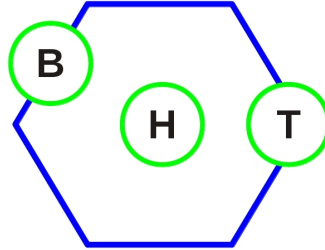


Figure 3.2: Top view of possible adsorption sites over the hexagon.

We considered adsorption sites in different hexagons of AGNR in such a manner that we generated 17 initial configurations to be relaxed for Ni and 25 for Ir, as shown simultaneously all adatoms in figures 3.3(a) for Ni and 3.3(b) for Ir. For the purpose of avoiding misunderstandings, keep in mind that every single defect system is composed by one adatom and the AGNR. Moreover, we imposed the periodic boundary conditions and performed the transport calculations along the Z axis.

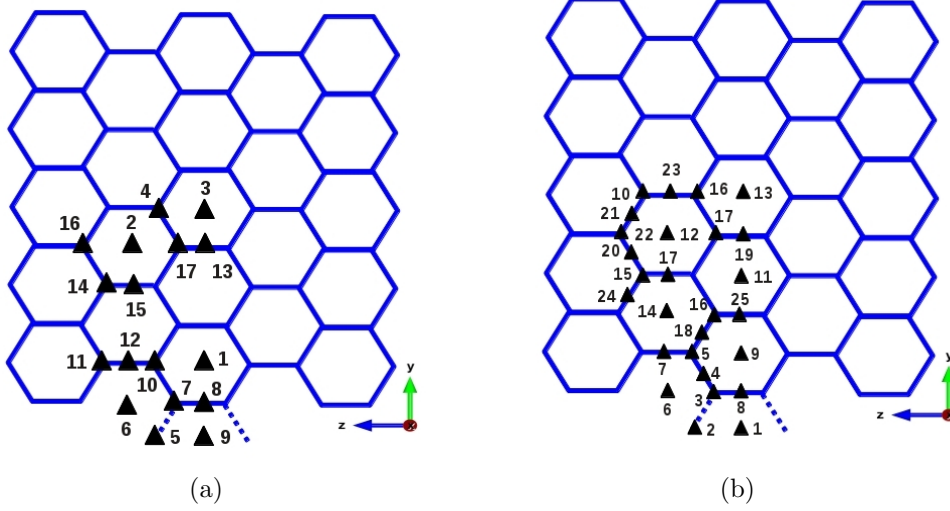


Figure 3.3: (a) Initial adsorption sites for Ni; (b) Initial adsorption sites for Ir.

All single defect systems were relaxed by means of the density functional theory (DFT) [47] using a localized atomic orbital basis set (LCAO) implemented in the SIESTA² package [59]. The local density approximation (LDA)³ parametrized by Ceperley-Alder was used for the exchange and correlation energy (E_{xc}) and the atomic-ion core described by Troullier-Martins pseudopotentials [60]. We employed a localized double zeta polarized basis set (DZP) and a density matrix and force convergence criterion of 10^{-6} eV and 0.02 eV/Å, respectively. The energy cut-off for the real space grid was 350 Ry, a 200 Monkhorst-Pack k-grid was used along the Z direction and we considered spin polarized calculations throughout this work.

3.1.1 Pristine AGNR

The geometry relaxation, the band structure and the total density of states of pristine AGNR were obtained according to the parameters described above. Figure 3.4 (left panel) shows the energy dispersion between high symmetry points along the path $Z - \Gamma - Z$. The total DOS (shown in figure 3.4 (b)), as mentioned previously, exhibits a gap which ultimately is achieved by cutting a graphene sheet in nanoribbons for nano-

²Spanish Initiative for Electronic Simulations with Thousands of Atoms.

³Even though GGA is typically used for calculations three main reasons support our choice of exchange and correlation approximation: 1) For adsorbed systems, due to a cancellation of errors, it gives a good description of the relaxed structures (even though the adsorption energies are underestimated). 2) Typically, LDA gives a good description of bulk transition metals, specially of the magnetic properties. 3) Most important a good non-collinear GGA (and SO interaction) is not available in any code to the best of our knowledge.

electronic and spintronic device applications. We also note the Van Hove singularities at the band edges.

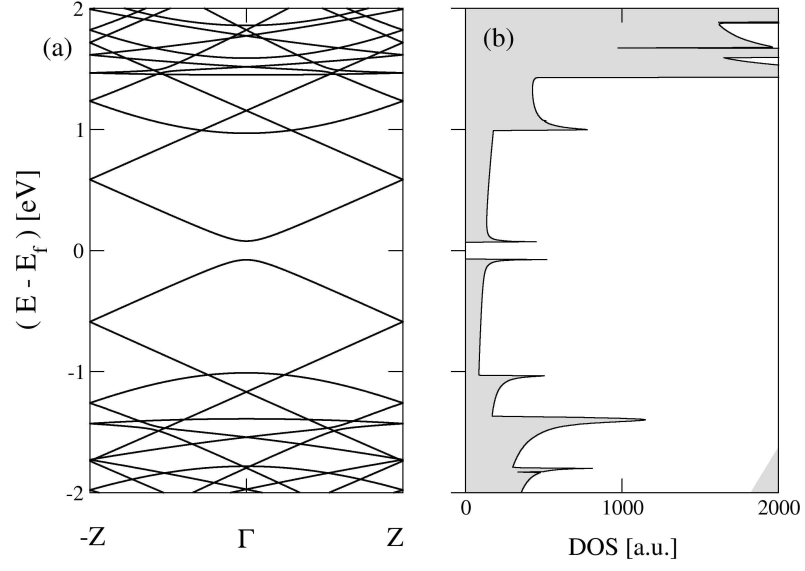


Figure 3.4: (a) Energy dispersion relation. (b) Total DOS of pristine AGNR around Fermi energy.

3.1.2 Nickel impurities

The initial 17 configurations formed by each individual Ni atom adsorbed on the AGNR are simultaneously shown in figure 3.5(a) and the relaxed structures are depicted in figure 3.5(b). We observed that Ni atom initially positioned on site 4 (Top site) relaxed to a hollow site on final configuration. This means (in agreement with our notation) that structures Ni@AGNR-4 and Ni@AGNR-3 are the same. For the sake of simplicity, we will call the structure Ni@AGNR-4 as the *symmetric* (s) and it will be renamed as Ni@AGNR-s from now on.

The most stable (Ni@AGNR-1) and the symmetric (Ni@AGNR-s) structures are represented schematically in figure 3.5(b) as red circles. Moreover, we found that those two structures have zero magnetic moment making it a perfect non-magnetic system to observe spin-flip scattering owing purely to the SO effect. A full table containing pictures of the initial and relaxed structures can be found in Appendix A.

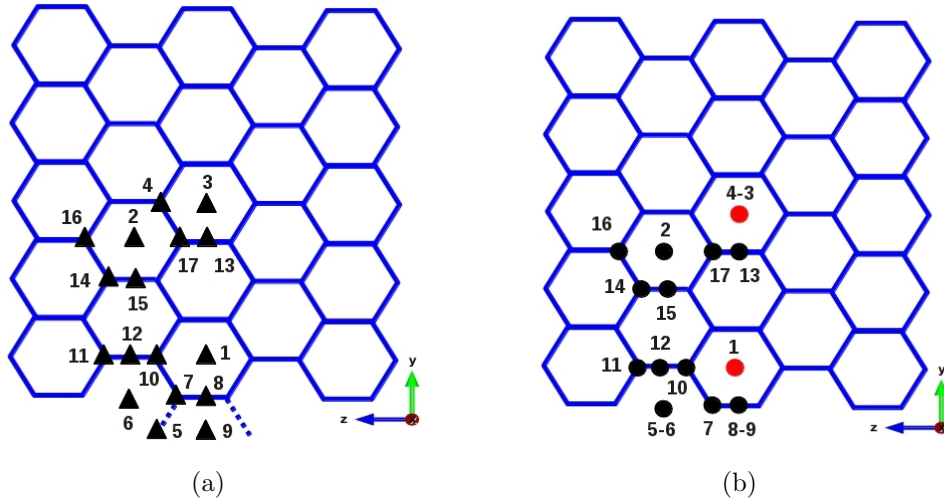


Figure 3.5: (a) Initial (triangles) Ni adsorption sites on AGNR; (b) Relaxed (circles) Ni adsorption sites on AGNR. Red circles indicate the systems studied in this work: the most stable (Ni@AGNR-1) and the symmetric (Ni@AGNR-4). From now on, $\text{Ni@AGNR-4} \Leftrightarrow \text{Ni@AGNR-s}$

All the relaxed structure arranged in ascending order with respect to the relative energy, the Ni adsorption distances of relaxed systems and the type of relaxed adsorption sites are listed in table 3.1. It is evident from these results that Ni adatoms prefer hollow sites particularly at the edge of the AGNR. Figure 3.6 shows the top view of the most stable and symmetric structures relaxed. These structures are the starting point of this project to later study the single defect spin-polarized electronic transport.

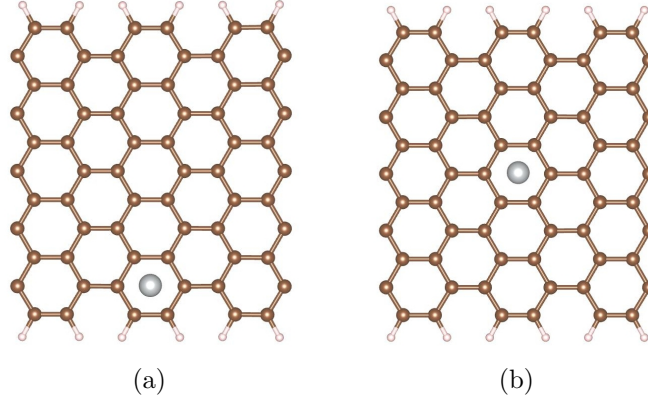


Figure 3.6: (a) The most stable structure: Ni@AGNR-1, (b) The symmetric structure: Ni@AGNR-s.

Ni adsorption site	Relaxed structure	Relative energy [eV]	D [\AA]
H	Ni@AGNR-1	0.000	1.5998
H	Ni@AGNR-2	0.152	1.4415
H	Ni@AGNR-3	0.176	1.3865
H	Ni@AGNR-4(s)	0.177	1.4295
H	Ni@AGNR-5	0.308	1.3344
H	Ni@AGNR-6	0.319	1.3773
T	Ni@AGNR-7	0.388	1.7509
B	Ni@AGNR-8	0.453	1.8039
B	Ni@AGNR-9	0.487	1.7189
T	Ni@AGNR-10	0.558	1.7621
T	Ni@AGNR-11	0.647	1.7623
B	Ni@AGNR-12	0.660	1.7627
B	Ni@AGNR-13	0.747	1.7761
T	Ni@AGNR-14	0.759	1.7527
B	Ni@AGNR-15	0.763	1.7617
T	Ni@AGNR-16	0.774	1.6816
T	Ni@AGNR-17	0.775	1.7303

Table 3.1: Ni adsorption sites, relative energies of relaxed structures and Ni adsorption distances of relaxed structures.

3.1.3 Iridium impurities

Similar to the Ni case, we consider 25 initial configurations composed of each individual Ir atom adsorbed on the AGNR. As shown in figure 3.7(a-b) for initial and relaxed structures, respectively. In this case we observed that structures Ir@AGNR-12 and Ir@AGNR-13 relax to the same hollow site, structures Ir@AGNR-15 and Ir@AGNR-17 relax to the same bridge site, the structures Ir@AGNR-2, Ir@AGNR-3 and Ir@AGNR-4 relax to the same top site and the structures Ir@AGNR-5, Ir@AGNR-6 and Ir@AGNR-7 relax to the same quasi-hollow site. In figure 3.5(b) we show in red circles the most stable (Ir@AGNR-1) and the symmetric (Ir@AGNR-13 or Ir@AGNR-s) structures.

In addition, we point out that Ir adatoms give us two different type of systems with respect to the observation of magnetic moment. While the most stable structure (Ir@AGNR-1) has a zero magnetic moment, the symmetric structure (Ir@AGNR-s) exhibit a non-zero magnetic moment. Similarly to the Ni impurity case a table including a complete representation for the initial and relaxed structures is presented in Appendix A.

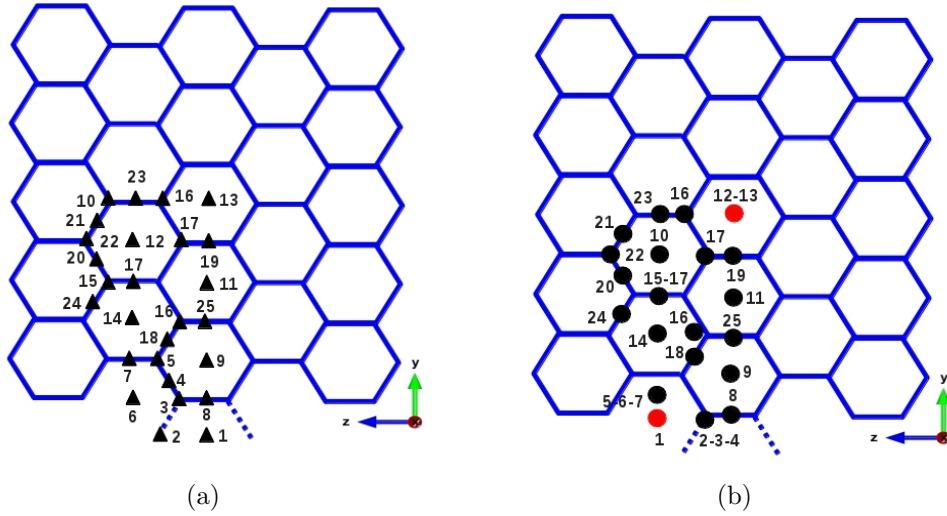


Figure 3.7: (a) Initial (triangles) Ir adsorption sites on AGNR; (b) Relaxed (circles) Ir adsorption sites on AGNR. Red circles indicate the systems studied in this work: the most stable (Ir@AGNR-1) and the symmetric (Ir@AGNR-13). From now on, $\text{Ir@AGNR-13} \Leftrightarrow \text{Ir@AGNR-s}$.

In table 3.2 we list all the relaxed structures (in ascending order with respect to the relative energy) the Ir adsorption distances to the graphene plane of the systems relaxed, and the type of relaxed adsorption site. Figure 3.8 shows the top view of the most stable and symmetric structures separately after relaxation. We notice that the Ir adatom in the most stable system prefers a hollow site and rest at the very edge of the AGNR. As usual, these structures are also the starting point to later perform single defect spin-polarized electron transport.

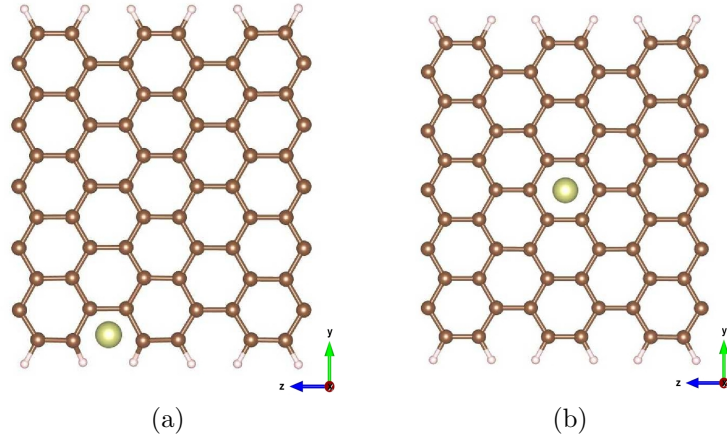


Figure 3.8: (a) The most stable structure: Ir@AGNR-1, (b) The symmetric structure: Ir@AGNR-s.

Ir ad-site	Relaxed structure	Relative energy [eV]	D [\AA]	Magnetic moment [μ_B]
H	Ir@AGNR-1	0.000	1.3739	0.0000
T	Ir@AGNR-2	0.009	1.7249	0.4770
T	Ir@AGNR-3	0.024	1.8145	0.6198
T	Ir@AGNR-4	0.038	1.8216	0.7142
H	Ir@AGNR-5	0.041	1.5438	0.0000
H	Ir@AGNR-6	0.042	1.5450	0.0000
H	Ir@AGNR-7	0.043	1.5449	0.0000
B	Ir@AGNR-8	0.102	1.8932	0.9994
H	Ir@AGNR-9	0.264	1.7388	0.9771
H	Ir@AGNR-10	0.513	1.6460	0.3770
H	Ir@AGNR-11	0.515	1.6450	0.0000
H	Ir@AGNR-12	0.516	1.6483	0.3845
H	Ir@AGNR-13(s)	0.516	1.6483	0.3845
H	Ir@AGNR-14	0.525	1.6446	0.3774
B	Ir@AGNR-15	0.640	1.9024	0.6930
T	Ir@AGNR-16	0.655	1.9220	0.6300
B	Ir@AGNR-17	0.692	1.9941	0.9927
B	Ir@AGNR-18	0.710	1.9993	0.9095
B	Ir@AGNR-19	0.758	1.9958	0.9813
B	Ir@AGNR-20	0.767	1.9981	0.8032
B	Ir@AGNR-21	0.784	1.9949	0.8011
T	Ir@AGNR-22	0.813	1.8138	0.0000
B	Ir@AGNR-23	0.822	1.9984	0.9585
B	Ir@AGNR-24	0.834	1.9968	0.7544
B	Ir@AGNR-25	0.838	1.9919	0.9735

Table 3.2: Ir adsorption sites, relative energies of relaxed structures and Ir adsorption distances of relaxed structures.

The next two sections are devoted to the discussion of the electronic structure results, such as band structures, total DOS and PDOS, subsequently we focus on the spin-polarized electron transport, in the first place for Ni single defect systems followed by Ir single defect systems. In both cases we considered for the most stable and symmetric cases, reminding that Spin-Orbit interaction was included in the computations.

3.2 Electronic structure and spin-polarized transport - Ni

3.2.1 Band structures

We start describing the energy dispersion results for the Ni adatom. As pointed out before, we performed calculations of our selected structures (Ni@AGNR-1 and Ni@AGNR-s) to observe the effect of the SO interaction in the dispersion relation. The band structure from high symmetry points follows the path - Z - Γ - Z . Those are presented in figure 3.9(a-c) for the no-SO interaction case for pristine AGNR, Ni@AGNR-1 and Ni@AGNR-s, respectively.

The energy dispersion relation for those structures of interest exhibits a direct band gap nature. Furthermore, additional bandlines are observed only below the Fermi energy for both Ni@AGNR-1 and Ni@AGNR-s systems (Figs.3.9(b) and (c)) whereas remain unchanged for energies above the Fermi level. On the other hand, those extra bandlines in Ni@AGNR-s structure are broader and somewhat shifted to negative energy values than in the Ni@AGNR-1 structure. As we will show later, these bands are associated with Ni d states⁴.

⁴Here we would like to caution the reader as to the gaps formed upon adsorption of Ni. While the gap at E_F is a true gap, the moving associated to the impure states are formed solely due to periodic nature of the calculation. On the true system - a single Ni atom on a nanoribbon - such gaps will not be present. In this sense, the gaps are only used to highlight the effect of the SO interaction [61].

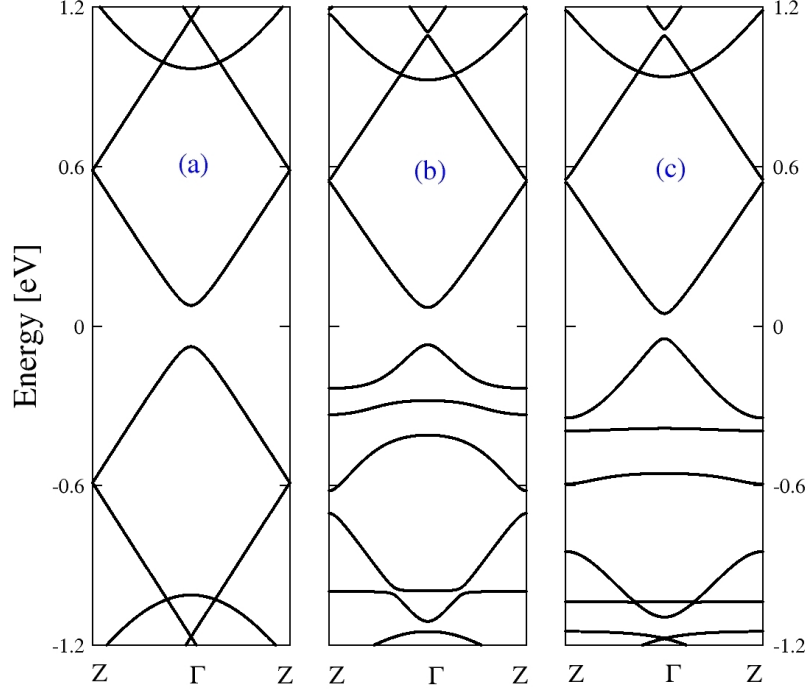


Figure 3.9: Energy dispersion of: (a) Pristine AGNR, (b) Ni@AGNR-1, and (c) Ni@AGNR-s without SO coupling.

The band structures for calculations considering SO for the same structures are shown in figures 3.10(a-c). Clearly, the splitting of bands below the Fermi level in Ni@AGNR-1 structure (Fig.3.10 (b)) is more pronounced than the splitting in the Ni@AGNR-s (Fig.3.10 (c)) structure while above the Fermi level the splitting is more or less the same. The splitting observed is a Rashba type which is a direct consequence of the lack of inversion symmetry of the structures [62] and manifested as a splitting of bands along the wave vector axis. In our structures of interest the Ni adatom break the inversion symmetry. Li et *al.* studied the Rashba splitting of graphene on Ni(111) substrate by using DFT [63] and Yu et *al.* used angle-resolved photo-emission spectroscopy technique (ARPES) [64]. Our results are in agreement with them in the sense that the SO interaction causes - Rashba - type splitting on the bands.

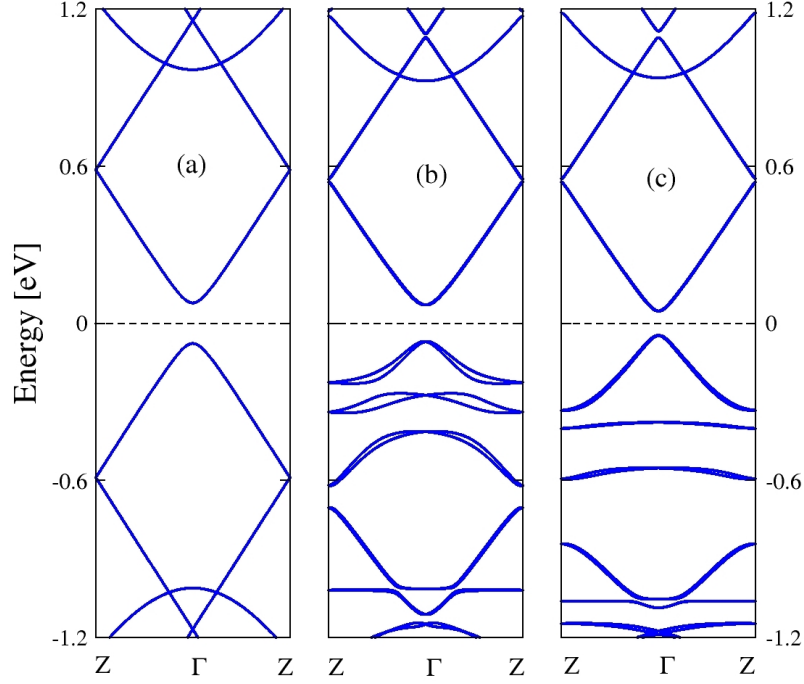


Figure 3.10: Energy dispersion of: (a) Pristine AGNR, (b) Ni@AGNR-1, and (c) Ni@AGNR-s with SO coupling.

In figures 3.11(a-b) a comparison between structures with and without SO interaction for Ni@AGNR-1 and Ni@AGNR-s, respectively, shows the splitting of bands due to the SO effect, as described previously. The two center panels show the dispersion energy from -1 to 1 eV where the splitting is observed in both structures (stable and symmetric). For the purpose of seeing the splitting in the region close to the Fermi level a magnification of the bands (dashed red line boxes) is placed on the side of the central panels. We should note that the splitting on the valence band is greater than the conductance band. Also, a magnification of the inner bands (dashed green line boxes) is shown. Finally, as discussed before, the splitting of the bands below the Fermi level is greater for the most stable structure compare to the symmetric one.

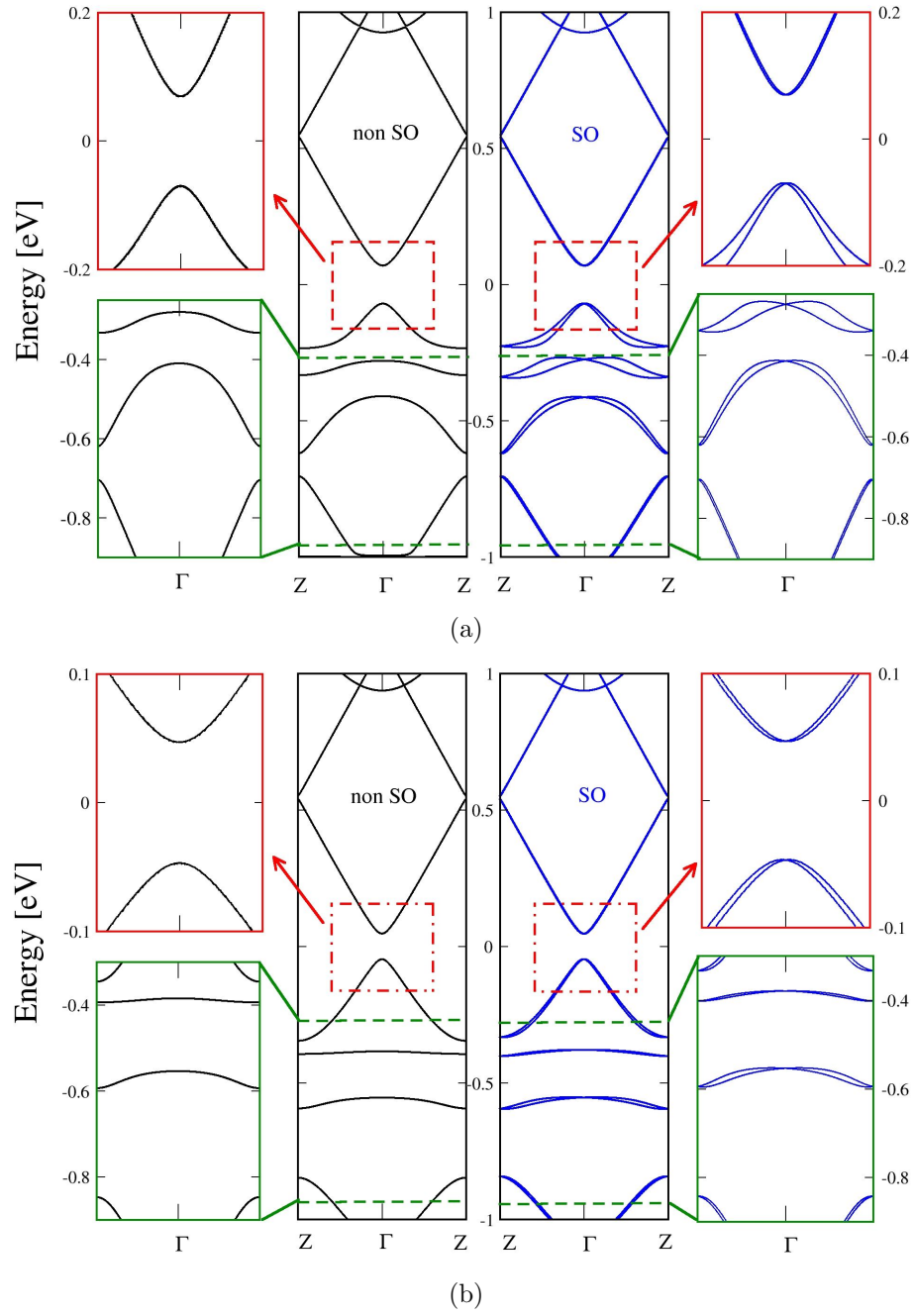


Figure 3.11: (a) Band structure around E_F for Ni@AGNR-1. (b) Band structure around E_F for Ni@AGNR-s. Blue lines correspond to SO and black lines to no-SO. The insets show the regions between dashed lines.

3.2.2 Total DOS and PDOS

The total DOS and PDOS were obtained from calculations using the Green's function formalism in order to avoid problems arising from the periodic boundary conditions⁵. As we have seen from the band structure, the effect of the SO interaction only causes a shift in the wave vector direction. Such an effect will be integrated out in the DOS. Figures 3.12(a-c) show the total DOS for pristine AGNR, Ni@AGNR-1 and the Ni@AGNR-s are shown, respectively. We can clearly notice that upon addition of Ni, the Van Hove singularities at the top of the valence band and bottom of conduction band are washed away. Furthermore, states below the Fermi level appears, which are apparently broad in the Ni@AGNR-s case and more localized in the Ni@AGNR-a case. This effect is caused by Ni the adatom on pristine AGNR.

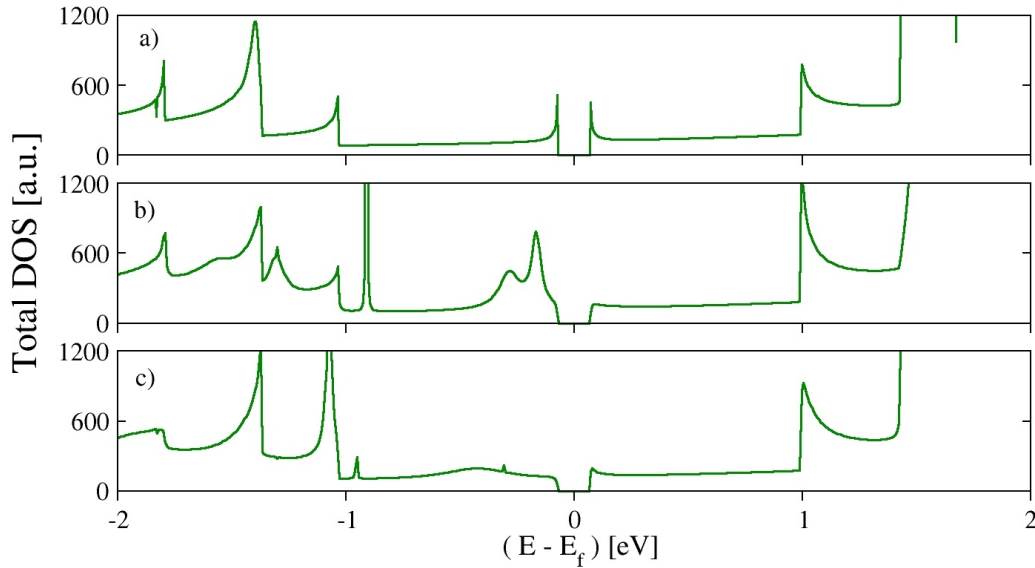


Figure 3.12: Total DOS around Fermi energy of: (a) Pristine AGNR, (b) Ni@AGNR-1 and (c) Ni@AGNR-s.

In order to determine the character of these states we project the DOS onto specific orbitals/atoms. In figure 3.13 we show the carbon atoms selected to plot the PDOS as well as the Ni atom. The carbon atoms that were selected were the non commensurate ones - for symmetric reasons - closest to Ni atom.

⁵Here we will show only the PDOS of the non-SO system

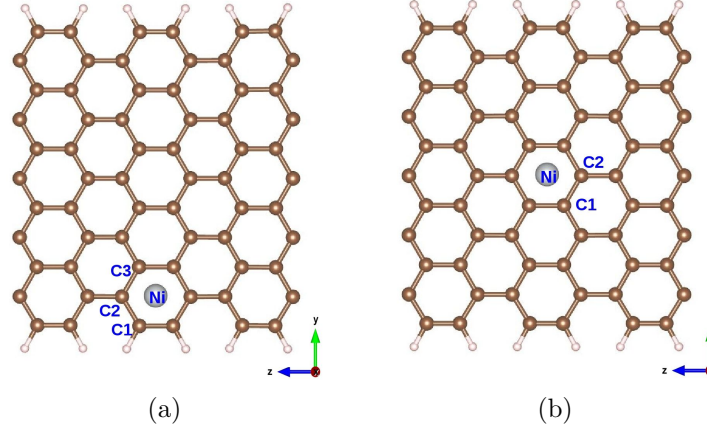


Figure 3.13: Atoms Ni, C1, C2 and/or C3 considered to obtain PDOS of each structures: (a) Ni@AGNR-1 and (b) Ni@AGNR-s.

The total DOS, the PDOS of Ni, C(1-3) atoms and the PDOS of the different d orbitals of Ni atom for structure Ni@AGNR-1 are shown in figures 3.15(a-c), respectively. As we can see the additional states observed in total DOS of Ni@AGNR-1 come from Ni atom states. Particularly, we notice that the contribution due to carbon is much smaller (and broader) in the energy window being considered.

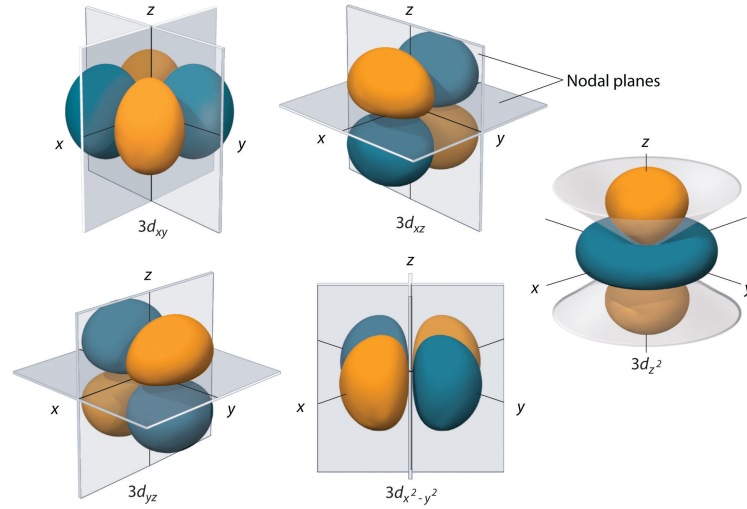


Figure 3.14: Four of the five $3d$ orbitals consist of four lobes arranged in a plane that is intersected by two perpendicular nodal planes. These four orbitals have the same shape but different orientations. The fifth $3d$ orbital, $3d_{z^2}$, has a distinct shape even though it is mathematically equivalent to the others. The phase of the wave function for the different lobes is indicated by color: orange for positive and blue for negative [2].

More interestingly, if one looks at PDOS of different $3d$ orbitals of Ni (Fig. 3.15(c)) it is possible to identify which ones correspond to each peak in the total PDOS of Ni. It is observed that only the $4s$ orbital of Ni has a significant contribution to the total DOS for energies greater than 1.5 eV (above the Fermi level) whereas $3d$ orbitals give a larger contribution for energies below the Fermi level. In our case, the z -direction is the direction of transport.

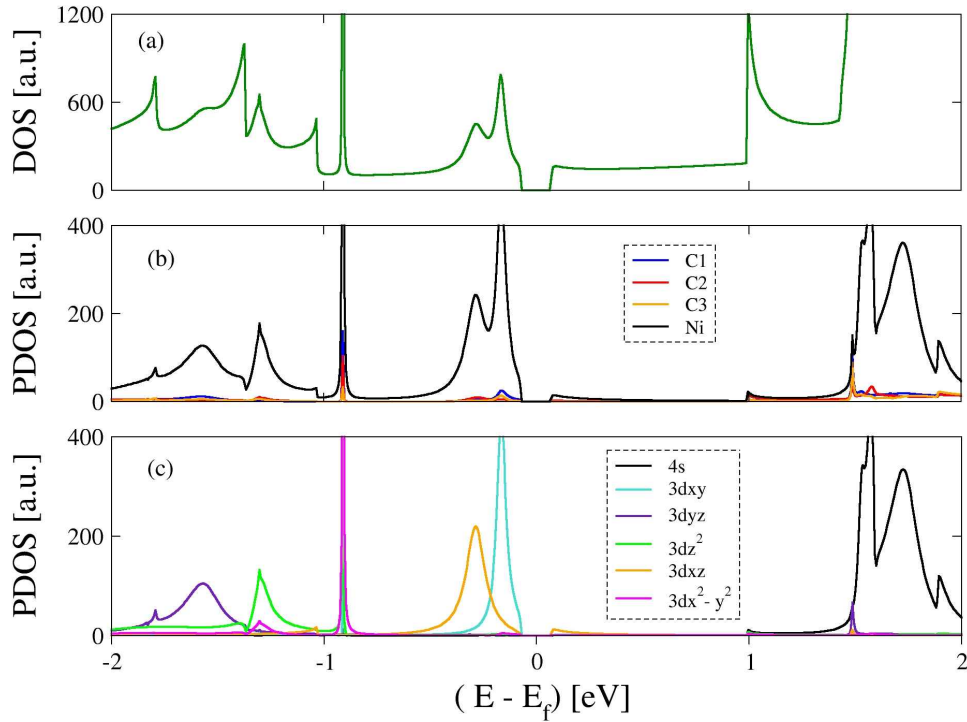


Figure 3.15: For Ni@AGNR-1 : (a) Total DOS. (b) PDOS of Ni, C1, C2, and C3 atoms. (c) PDOS of $3d$ orbitals of Ni atom. These orbitals are: $4s$ (black line), $3d_{xy}$ (turquoise line), $3d_{yz}$ (indigo line), $3d_{z^2}$ (green line), $3d_{xz}$ (orange line) and $3d_{x^2-y^2}$ (magenta line).

In a similar manner for the symmetric structure Ni@AGNR-s, the total DOS, the PDOS of Ni, carbon C1 and C2 and the PDOS of each $3d$ orbital of Ni are shown in figure 3.16(a-c). Similarly, additional states observed in the total DOS of Ni@AGNR-s (symmetric) come from nickel (see Fig.3.12). If we look at the PDOS of Ni (black line) compared with the PDOS of carbon atoms C1 (blue line) and C2 (red line) in figure 3.16(b) we can clearly distinguish that the contribution of Ni is much larger than carbon for energies below the Fermi level and for energies greater than 1.5 eV. Again, by looking only at the PDOS of Ni- $3d$ orbitals (figure 3.16(c)) we can identify which orbitals correspond to each peak observed in the PDOS. Against, only the orbital $4s$

of Ni contributes highly at energies above 1.5 eV whereas 3d orbitals contribute at energies below the Fermi level.

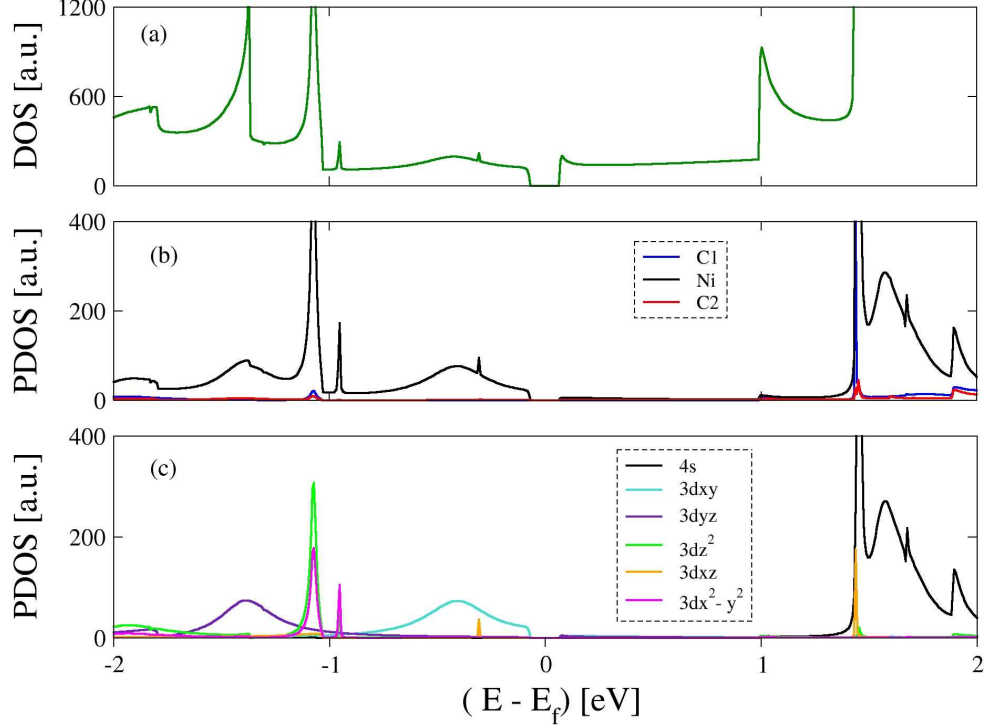


Figure 3.16: For Ni@AGNR-s : (a) Total DOS. (b) PDOS of Ni, C1, and C2 atoms. (c) PDOS of 3d orbitals of Ni atom. These orbitals are: 4s (black line), 3dxy (turquoise line), 3dyz (indigo line), 3dz² (green line), 3dxz (orange line) and 3dx²-y² (magenta line).

Comparing both structures (stable and symmetric), we should note that orbitals 3dxy and 3dxz are close to E_F , the 3dxy is narrower and higher in structure Ni@AGNR-1 compared to Ni@AGNR-s. Also the 3dxz state is very similar to the 3dxy state in Ni@AGNR-1 which is not the case in Ni@AGNR-s. Moreover, we can observe that 3dyz state are quite similar in both structures and 3dx²-y² state has 2 narrow peaks in Ni@AGNR-s while in Ni@AGNR-1 it has only one.

Finally, we can conclude that the nature of the bonds are slightly similar in both structures except with those bonds around the E_F and -1 eV, as it was described above. This difference in nature of d states, as we can see, comes from the adsorption site of the Ni adatom on the pristine AGNR system.

3.2.3 Single defect transport - Ni

The two-probe device used in this work to perform transport calculations (as it was pointed out in section 2.3) is represented in figure 3.17. It comprises a central region attached to two semi-infinite leads. The adatom adsorption sites for both single defect structures (Ni@AGNR-1 and Ni@AGNR-s) are shown in figure 3.17 simultaneously.

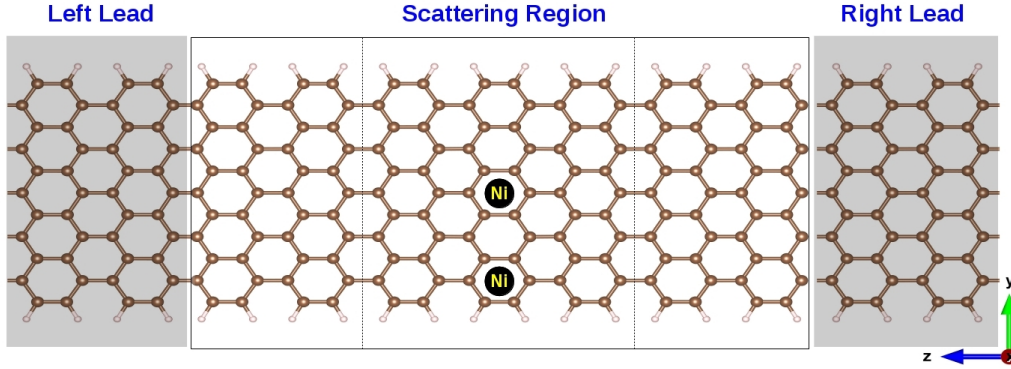


Figure 3.17: Scheme of a two-probe setup used for transport computations. A central region (scattering region) is connected to two semi-infinite leads (shadow region). Scattering region is an assemble of the single defect structure sandwiched between two electrodes.

The PDOS of orbitals of Ni, the transmission probabilities without SO and the transmission probabilities with SO are presented in figure 3.18(a-c), respectively. The curves of the transmission coefficients show us the probability for different incoming and outgoing electron spin states. The dashed lines correspond to transport in the pristine AGNR (it counts the number of available bands).

In the graphs spin-conserved ($T_{\uparrow\uparrow} = T_{\downarrow\downarrow}$; blue line) corresponds to the probabilities of incoming electrons with spin up (spin down) being transmitted with spin up (spin down) while spin-flip ($T_{\uparrow\downarrow} = T_{\downarrow\uparrow}$; red line) corresponds to the probability of electrons with spin up (spin down) being transmitted with spin down (spin up).

First analyse the case without SO, in figures 3.18(b) one observes that the spin-conserved transmissions decrease only in certain energy regions, namely: a region slightly below Fermi energy, a region between -2 and -1 eV, a sharp region close to -1 eV and a region above 1.5 eV. In particular, close to the Fermi level we observe a complete suppression of the transmission. From the PDOS in figure 3.18(a) we can associate these dips to Fano resonances [65] due to the Ni-*d* orbitals. Definitely, the orbitals of Ni atom have a strong influence in the transmission, decreasing the spin-conserved current. Interestingly, when the SO interaction is turned on we notice the appearance of spin-flip processes in the energy regions associated with the Ni-*d* states. More interesting still, these effects prevent the transmission from going to zero at the

Fano resonances. In essence regions where perfect backscattering was observe have non-vanishing transmission probability assisted by spin-flip process.

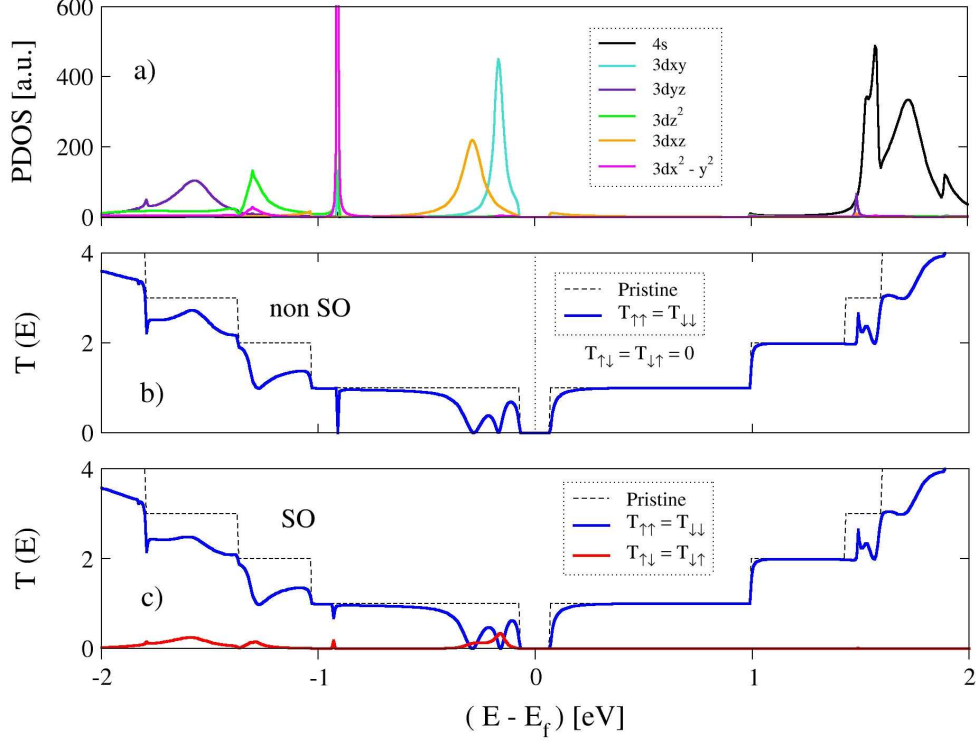


Figure 3.18: For Ni@AGNR-1: (a) PDOS of Ni orbitals, (b) Spin-conserved ($T_{\uparrow\uparrow} = T_{\downarrow\downarrow}$) and spin-flip ($T_{\uparrow\downarrow} = T_{\downarrow\uparrow} = 0$) transmission probabilities without SO coupling and (c) Spin-conserved ($T_{\uparrow\uparrow} = T_{\downarrow\downarrow}$) and spin-flip ($T_{\uparrow\downarrow} = T_{\downarrow\uparrow}$) transmission probabilities with SO coupling. Dashed lines correspond to transport in the pristine AGNR.

In case of the symmetric adsorption configuration (Ni@AGNR-s), we show that spin-conserved transmission probabilities decreased even more than in the stable case (Ni@AGNR-1) principally at energies below the Fermi level as indicated in figure 3.19(b) and (c). This large decrease can be associated to the non-localized nature of orbitals $3dxy$ and $3dyz$. Although the state is broader it also leads to complete suppression of the transmission. The appearance of additional dips in the energy conductance can be ascribed to the orbitals $3dz^2$ and $3dx^2-y^2$ at energies around -1 eV and $3dxz$ at energy close to the E_F . One thing to note regards orbital $3dxz$: although it is very small notice that the SO effect does not come from the broad. The case without SO is qualitatively similar.

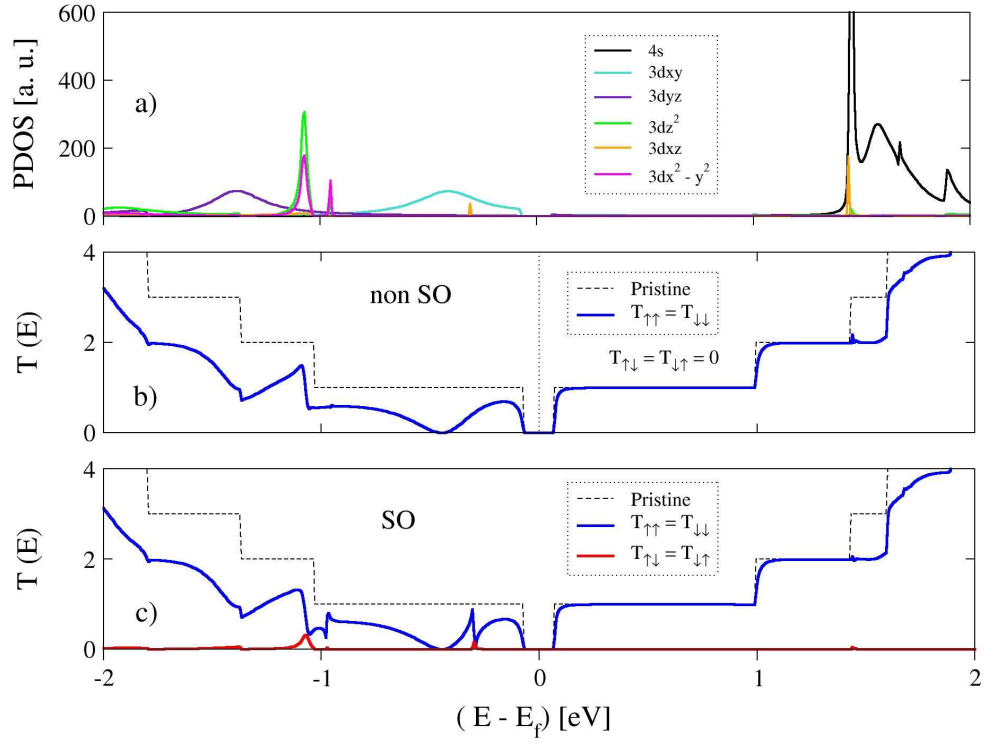


Figure 3.19: For Ni@AGNR-s: (a) PDOS of Ni orbitals, (b) Spin-conserved ($T_{\uparrow\uparrow} = T_{\downarrow\downarrow}$) and spin-flip ($T_{\uparrow\downarrow} = T_{\downarrow\uparrow} = 0$) transmission probabilities without SO coupling and (c) Spin-conserved ($T_{\uparrow\uparrow} = T_{\downarrow\downarrow}$) and spin-flip ($T_{\uparrow\downarrow} = T_{\downarrow\uparrow}$) transmission probabilities with SO coupling. Dashed lines correspond to transport in the pristine AGNR.

3.3 Electronic structure and spin-polarized transport - Ir

3.3.1 Band structures

We performed band structures calculations for the Ir@AGNR-1 (most stable) and Ir@AGNR-s (symmetric) adsorption configurations to observe the effect of the SO interaction in the energy band dispersion. The band structure following high symmetry lines along the path $Z - \Gamma - Z$, are presented in figure 3.20(a-c) for the pristine AGNR, Ir@AGNR-1 and Ir@AGNR-s, respectively. As before, these results do not include the SO interaction. The energy dispersion exhibits additional bandlines below and above the Fermi level for both Ir@AGNR-1 and Ir@AGNR-s systems (Figs.3.20(b) and (c)). Furthermore, the Ir@AGNR-s system shows splitting in the bands owing to the resultant magnetic moment ($0.3845 \mu_B$) of the system. We also note that the symmetric case has two localized states close to the Fermi level.

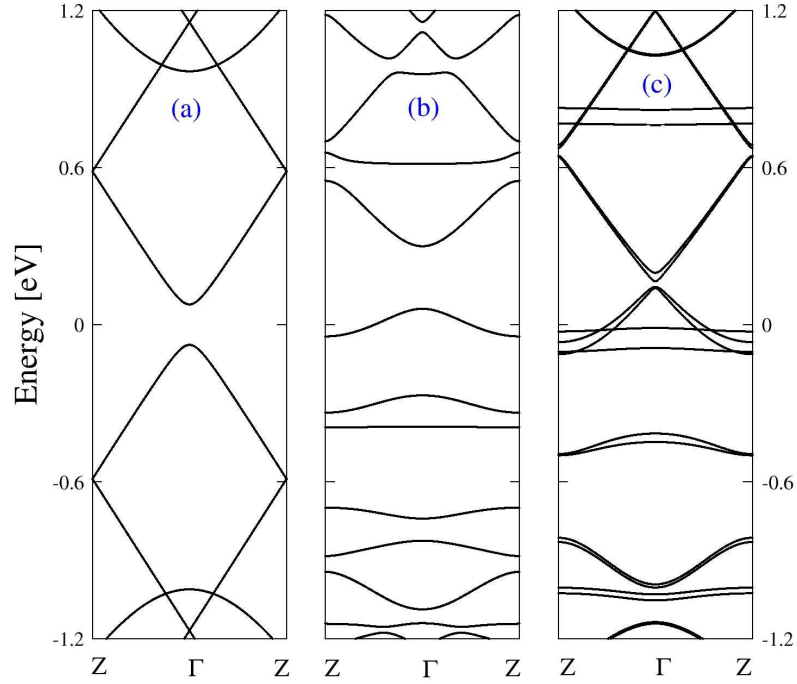


Figure 3.20: Energy dispersion of: (a) Pristine AGNR, (b) Ir@AGNR-1, and (c) Ir@AGNR-s without SO coupling.

Band structure calculations considering SO interaction are shown in figures 3.21(a-c). In both configurations the splitting occurs mostly at energies below E_F and to smaller extent at energies above Fermi level. The magnitude of splitting is comparable in those structures exhibiting wave vector displacement to a structure Ir@AGNR-1(Fig.3.21 (b)) whereas structure Ir@AGNR-s shows both wave vector and energy displacements (Fig.3.21 (c)). The level of splitting is a direct consequence of the lack of inversion symmetry of the structures (Rashba SO interaction) in both cases and additionally a Zeman type splitting is observed in Ir@AGNR-s due to the non-zero magnetic moment.

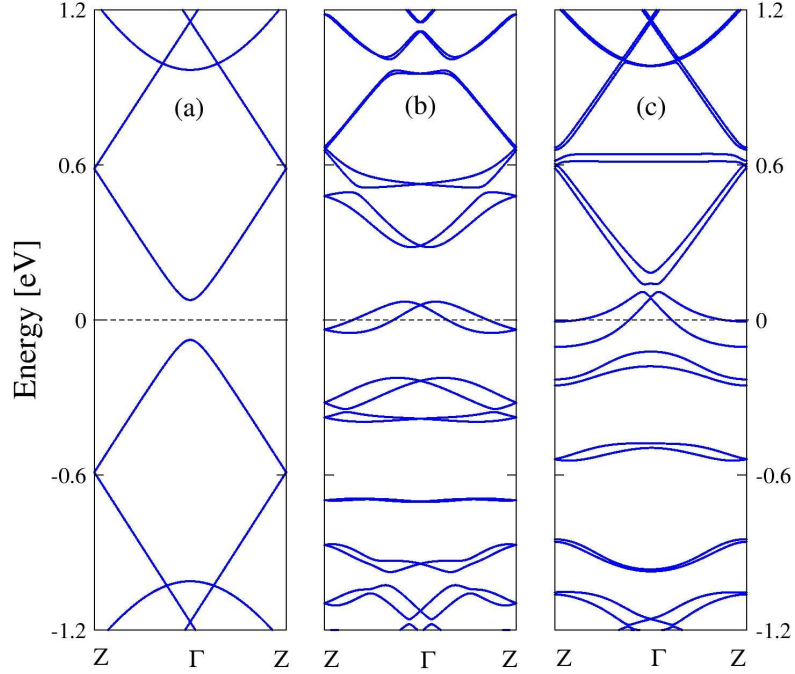


Figure 3.21: Energy dispersion of: (a) Pristine AGNR, (b) Ir@AGNR-1, and (c) Ir@AGNR-s with SO coupling.

For comparison, figures 3.22(a-b) present the energy bands with and without SO interaction for systems Ir@AGNR-1 and Ir@AGNR-s, respectively. The two central-most panels show the dispersion energy from -1 to 1 eV where a large splitting is observed in structure Ir@AGNR-1 whereas the splitting is significantly reduced in the symmetric structure. Moreover, the insets show a magnified region. Finally, we should note that the splitting is high in valence and conduction bands for stable the structure compared with Ni stable case (Ni@AGNR-1). So, while the SO interaction seems like a small perturbation in the case of Ni, the same can not be said about Ir where the SO effect

plays a major role in the electronic structure.

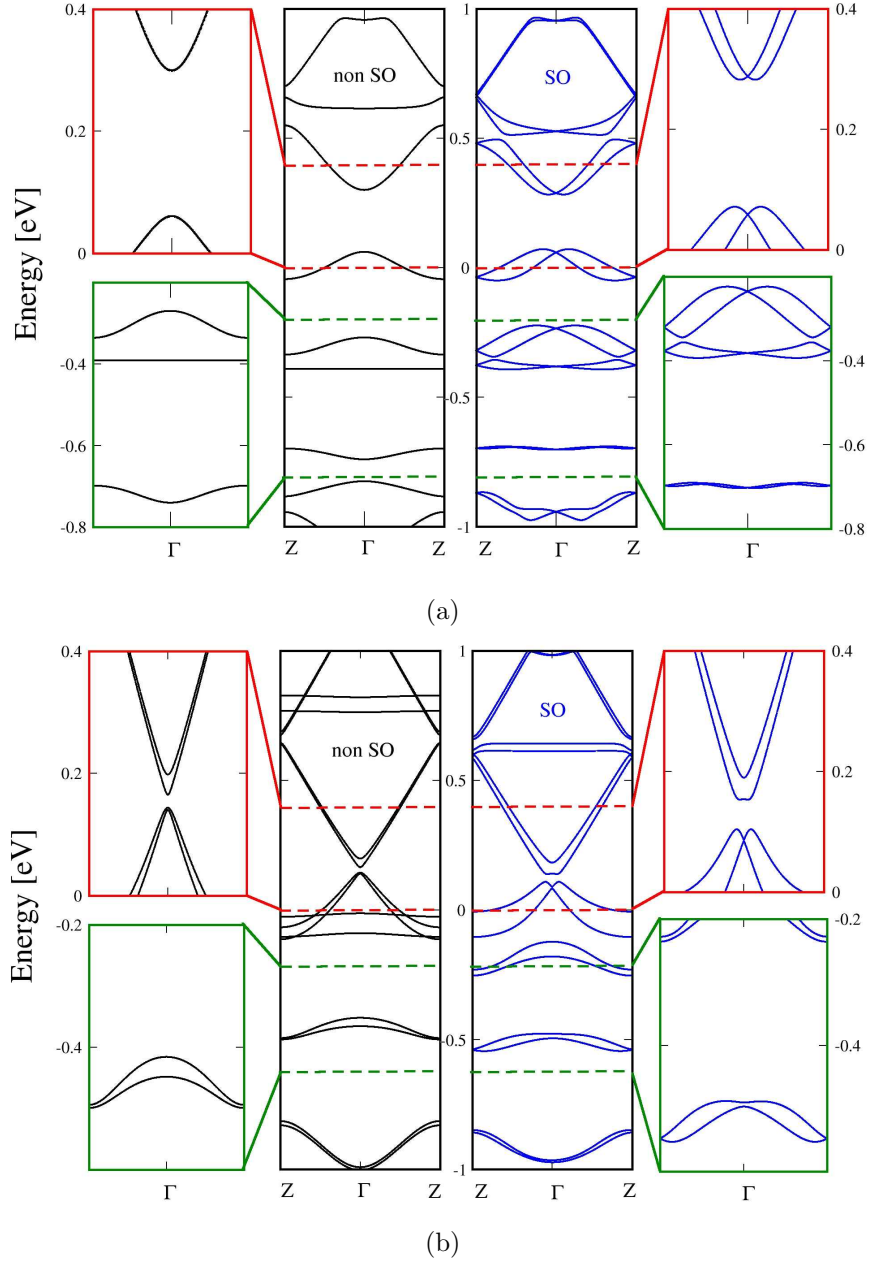


Figure 3.22: (a) Band structure around E_F for Ir@AGNR-1. (b) Band structure around E_F for Ir@AGNR-s. Blue lines correspond to SO and black lines to no-SO. The insets show the regions between dashed lines.

3.3.2 Total DOS and PDOS

Figures 3.23(a-c) shows the total DOS of pristine AGNR, Ir@AGNR-1 and Ir@AGNR-s, respectively. We can infer that states from Ir contribute to the total DOS at specific regions. In case of Ir@AGNR-s a very small spin polarization of $0.3845 \mu_B$ was found (Fig. 3.23(c)).

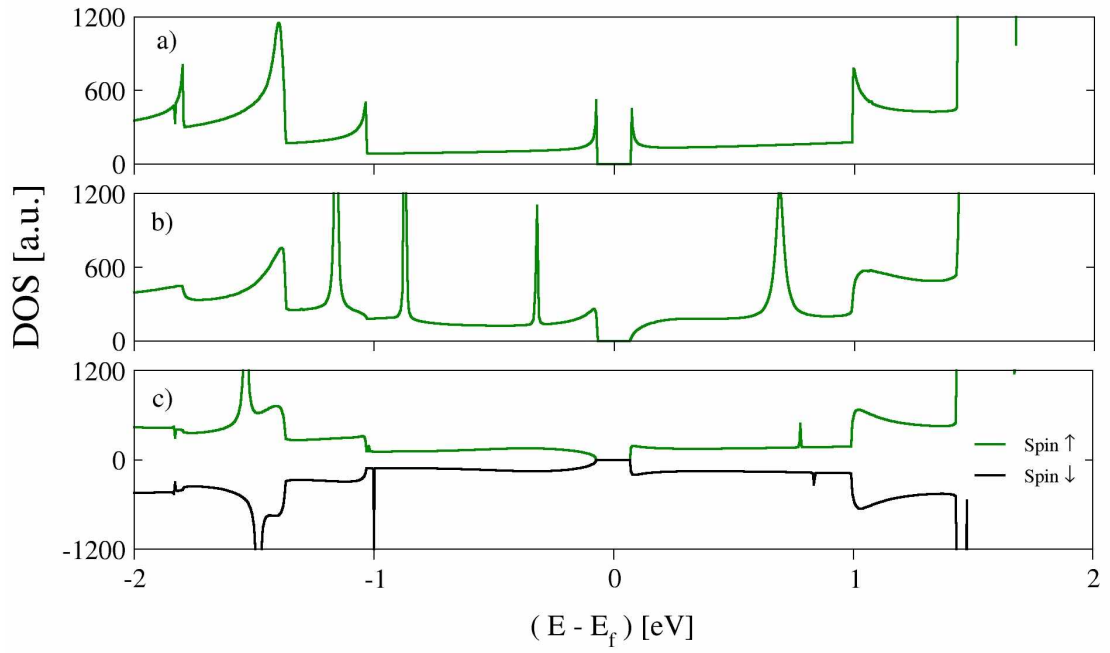


Figure 3.23: Total DOS around Fermi energy of: (a) Pristine AGNR, (b) Ir@AGNR-1 and (c) Ir@AGNR-s.

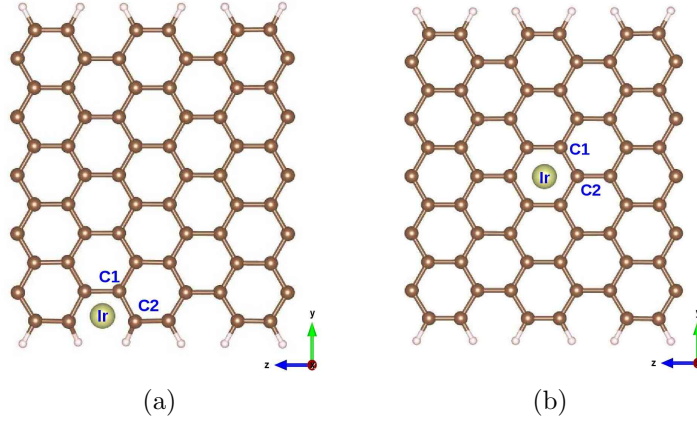


Figure 3.24: Ir and Carbon atoms for PDOS calculations in stable (a) and symmetric (b) systems.

The total DOS, the PDOS of Ir and C atoms and the PDOS of $5d$ and s orbitals of Ir for structure Ir@AGNR-1 are shown in figures 3.25(a), (b) and (c-1(2)), respectively. The calculations of the PDOS for both structures are based on the Ir and Carbon atoms as depicted in figure 3.24. The criteria to select them was the same used in the Ni case. The states of the Ir atom contribute to the total DOS as can be observed clearly in the PDOS of the Ir atom (dotted black line) in figure 3.25(b) at energies between -1 and 1 eV showing mostly a localized nature. With the exception of $5d_{xy}$ and $5d_{xz}$ orbitals the remaining ones are highly localized and make a large contribution to the Ir PDOS (even the $6s$ orbital, which, in the case of Ni adatom was delocalized at energies above 1.5 eV (Fig.3.25(c-1))). In addition, the polarization orbital $6p_x$ has a height comparable with $5d_{xy}$ and $5d_{xz}$ orbitals at different energies (Fig.3.25(c-2)).

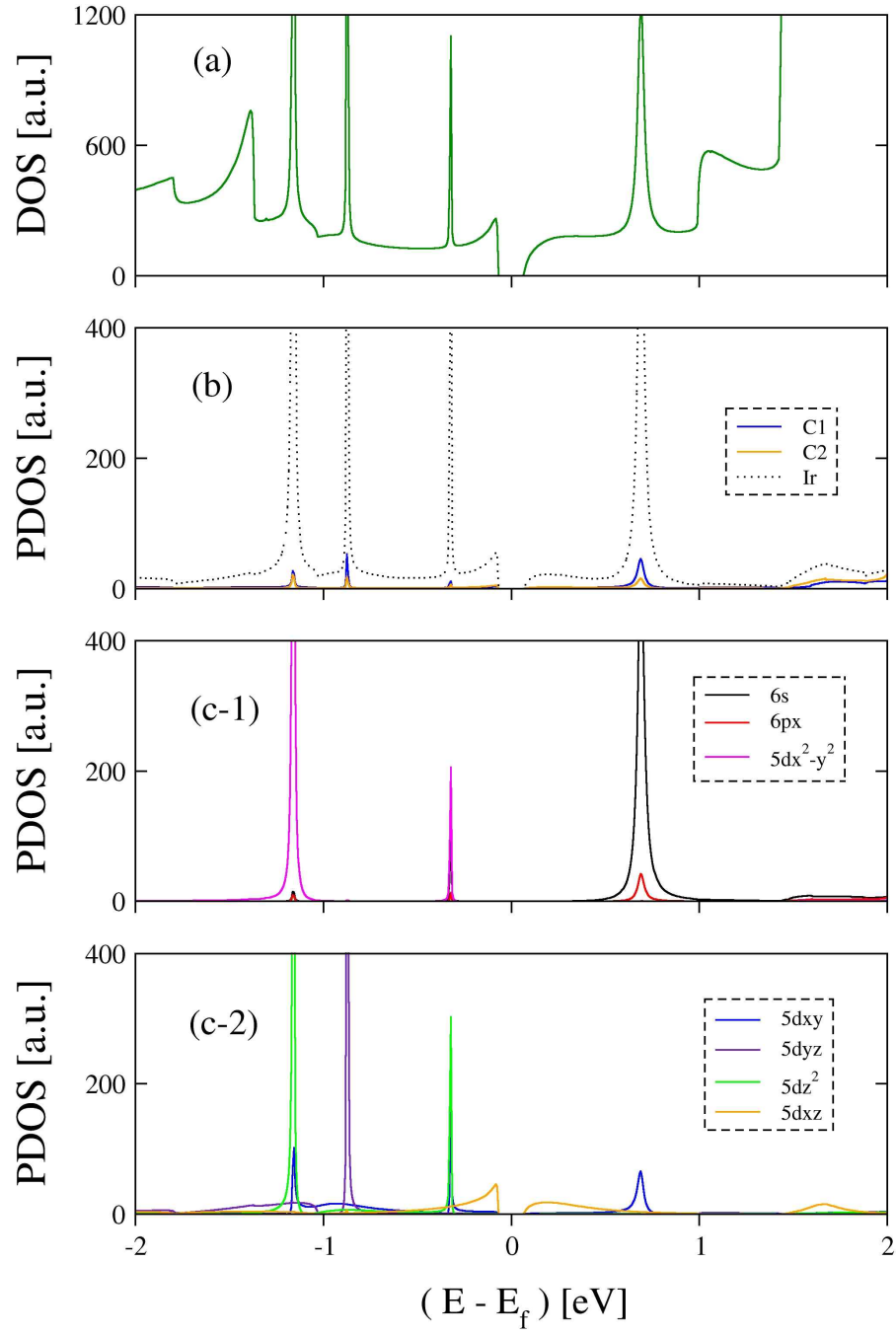


Figure 3.25: For Ir@AGNR-1 : (a) Total DOS. (b) PDOS of Ir and carbons C1 and C2. (c-1) PDOS of $6s$, $6p_x$ and $5d$ orbitals of Ir. (c-2) PDOS of $5d$ orbitals of Ir.

The behaviour in case of the symmetric adsorption configuration (Ir@AGNR-s) is completely different in the sense that the Ir states become delocalized, and the presence of spin polarization of few Ir states. For instance, by looking PDOS of Ir and carbon atoms (See Fig. 3.26(b)) we realized that the spin polarization observed in total DOS comes only from Ir states. If we turn to the orbital-separated PDOS results for Ir states we can identify which states are spin-polarized. For example, $6s$ (Fig.3.26(c-1)) and $5dz^2$ (Fig.3.26(c-2)) display spin-polarized behaviour mainly owing to the resultant magnetic moment found for this symmetric structure.

In summary the nature of the bond is significantly different in each structure. In one case - for stable system - it leads to localized orbitals with two peaks for $5dx^2-y^2$ and dz^2 and one peak for $5dyz$ states and in the other case (symmetric system) the localized orbitals are also $5dx^2-y^2$ and dz^2 but exhibit only one peak each.

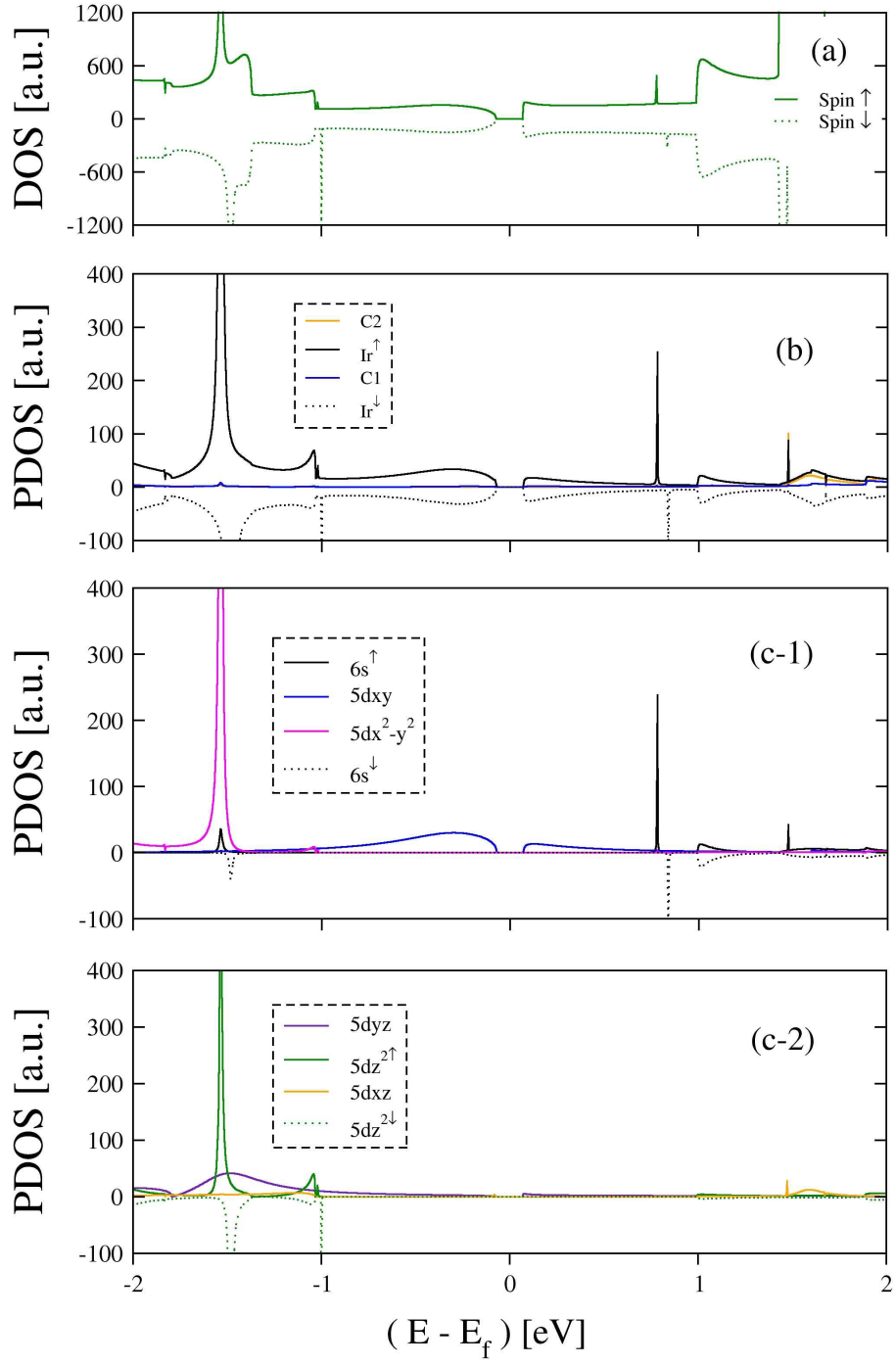


Figure 3.26: For Ir@AGNR-s : (a) Total DOS. (b) PDOS of Ir and carbons C1 and C2. (c-1) PDOS of 6s and 5d orbitals of Ir. (c-2) PDOS of 5d orbitals of Ir.

3.3.3 Single defect transport - Ir

The transport setup for Ir is similar to the one used for nickel with the two possible positions for the adatom shown in figure 3.27. The calculations of spin-polarized transport for both structures - stable (Ir@AGNR-1) and symmetric (Ir@AGNR-s) - shows a substantial reduction of the spin-conserved transmission probabilities in both cases (with and without SO interaction). Without SO, these reductions of spin-conserved transmission - in the case of Ir@AGNR-1 - occur at energies below and above the Fermi level (see Figs.3.28(b)), conversely to reductions in system Ir@AGNR-s where spin-conserved current was affected mostly at energies below E_F (see Figs.3.29(b)). This difference can be understood in terms of a state approximately 0.5 eV above E_F which leads to a Fano resonance in the case of Ir@AGNR-1. This state is pretty much uncoupled in the symmetric case (if it is so sharp it gives no contribution to transport).

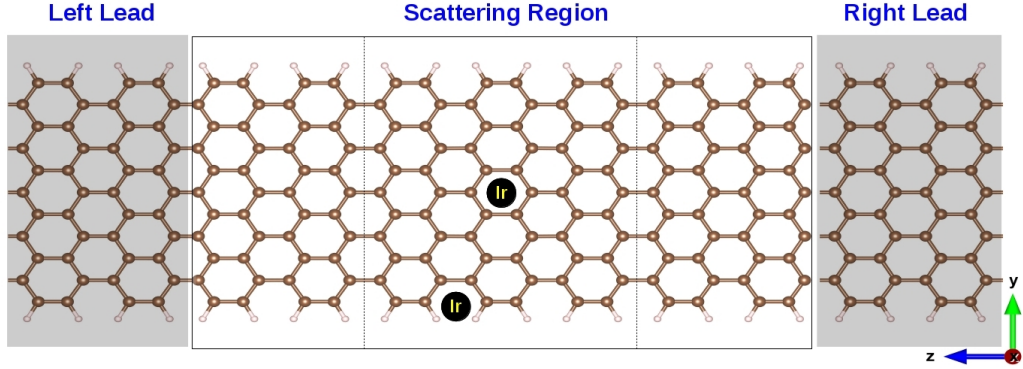


Figure 3.27: Scheme of a two-probe setup used for transport computations. A central region (scattering region) is connected to two semi-infinite leads (shadow region). Scattering region is an assemble of the single defect structure sandwiched between two electrodes.

In case of transport with SO, the reduction of the spin-conserved current follow similar tendencies with particular exceptions at energies close to the Fermi level where the spin-conserved transmission increases as illustrated in figures 3.28(c) and Figs.3.29(c). In the case of Ir@AGNR-1 we also notice the strong suppression of the Fano resonance.

The spin-flip transmission probabilities shows similar tendencies to the spin-conserved case. For instance, we can observe spin-flip current at energies below and above the Fermi level in structure Ir@AGNR-1 (see Figs.3.28(c)), while in structure Ir@AGNR-s the spin-flip current is mostly below and also nearby the Fermi energy (see Figs.3.29(c)).

Finally, we notice that the introduction of the SO interaction significantly changes the conduction in the single channel. There we notice that the introduction of the SO interaction actually enhances the transmission.

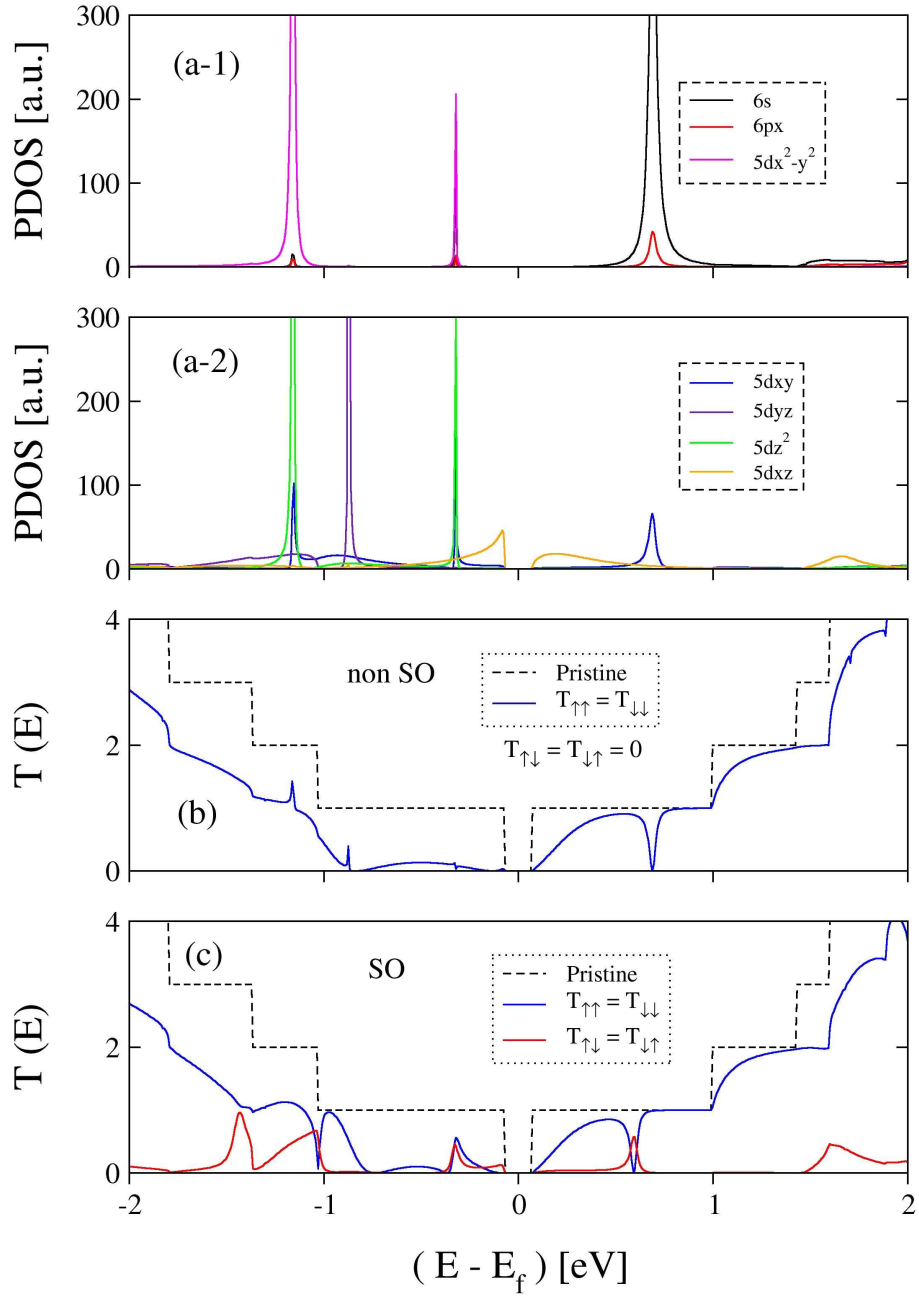


Figure 3.28: For Ir@AGNR-1: (a-1) and (a-2) PDOS of Ir orbitals, (b) Spin-conserved ($T_{\uparrow\uparrow} = T_{\downarrow\downarrow}$) and spin-flip ($T_{\uparrow\downarrow} = T_{\downarrow\uparrow} = 0$) transmission probabilities without SO coupling and (c) Spin-conserved ($T_{\uparrow\uparrow} = T_{\downarrow\downarrow}$) and spin-flip ($T_{\uparrow\downarrow} = T_{\downarrow\uparrow}$) transmission probabilities with SO coupling. Dashed lines correspond to transport in the pristine AGNR.

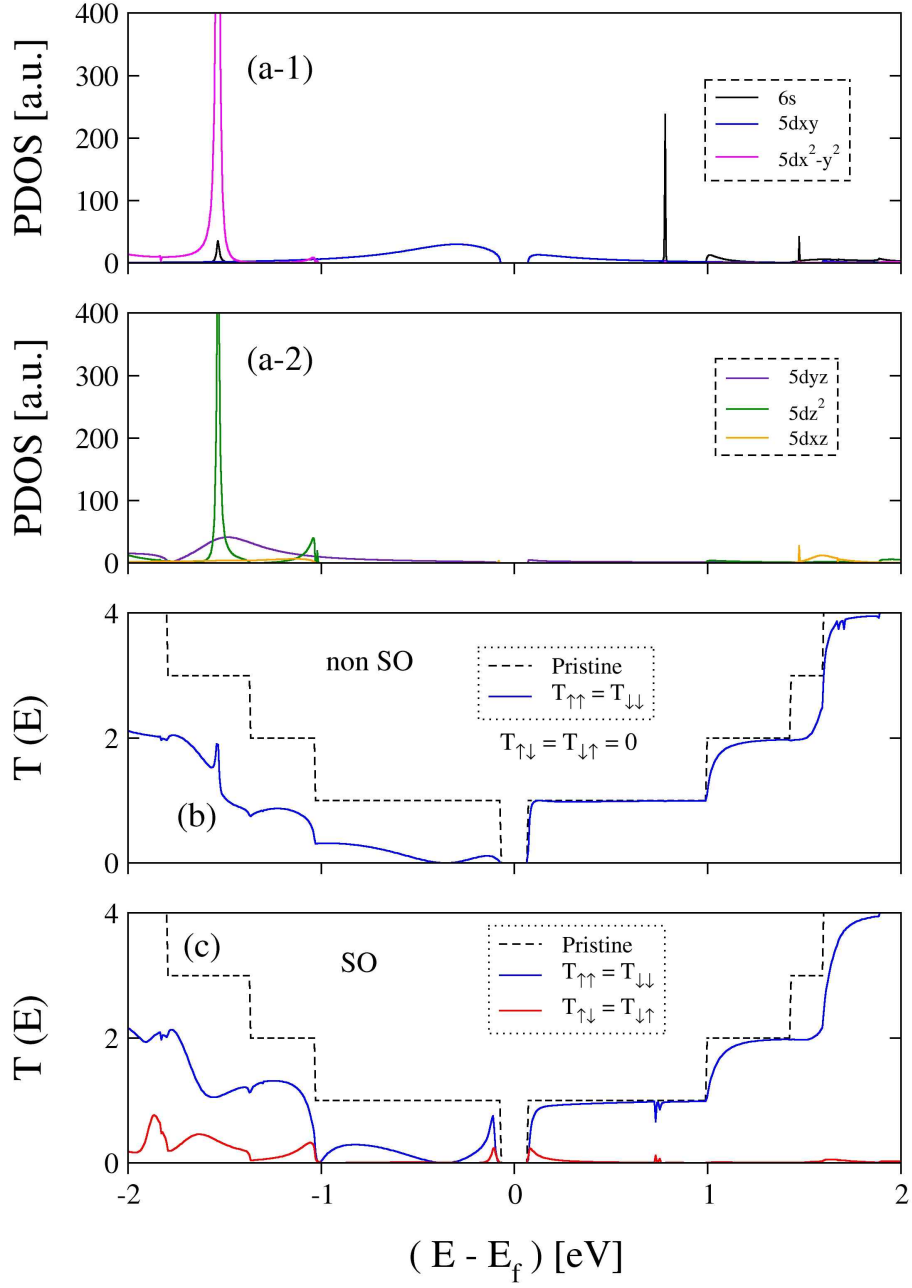


Figure 3.29: For Ir@AGNR-s: (a-1) and (a-2) PDOS of Ir orbitals, (b) Spin-conserved ($T_{\uparrow\uparrow} = T_{\downarrow\downarrow}$) and spin-flip ($T_{\uparrow\downarrow} = T_{\downarrow\uparrow} = 0$) transmission probabilities without SO coupling and (c) Spin-conserved ($T_{\uparrow\uparrow} = T_{\downarrow\downarrow}$) and spin-flip ($T_{\uparrow\downarrow} = T_{\downarrow\uparrow}$) transmission probabilities with SO coupling. Dashed lines correspond to transport in the pristine AGNR.

It is clear that the stronger SO interaction in Ir has a larger effect. While in Ni we notice only a perturbation compared to the non-SO case. Definitely the reduction or increment of the spin-conserved and spin-flip currents can be ascribed directly to the Ni or Ir orbitals, and their intensity depends on their localized nature. It is also related to the adsorption site of Ni or Ir atom on the AGNR structure. In particular, we point out that $3d$ orbitals of Ni and $5d$ of Ir result in strong dependences on the spin-conserved and spin-flip transmission probabilities. Moreover, It is clearly observed that the lack of inversion symmetry owing to the adsorption impurity led to different SO coupling intensities.

Chapter 4

Results and discussions II : Multiple defects

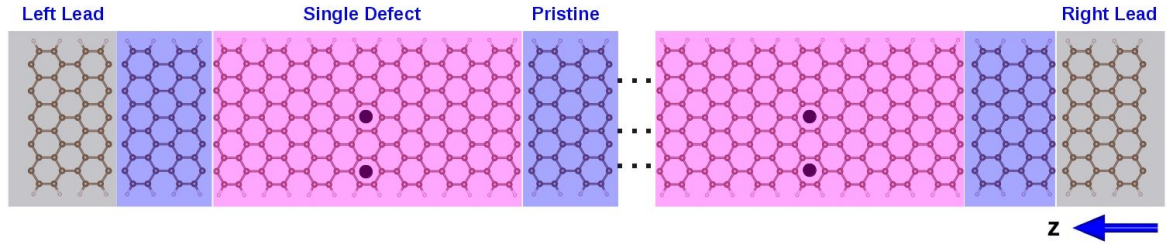


Figure 4.1: Schematic view of the typical setup for a disordered transport calculations. The left and right electrodes (grey shadow) consist of two semi-infinite segments of the pristine AGNR. The one dimensional realistic disordered nanoribbon attached to the electrodes consists of a randomly intercalation of pristine AGNR (blue shadow) and single defect (pink shadow) segments.

We now turn to a more realistic setup where a number of impurities are randomly distributed along a nanoribbon. This chapter is focused on the particular cases of Ni adsorption configurations, the most stable and the symmetric ones. The typical device used to calculate disordered transport is depicted in figure 4.1, where it was assembled using a few single defects segments, Ni@AGNR-1 or Ni@AGNR-s¹ (pink shadow boxes), separated by a random number of pristine AGNR (blue shadow boxes) segments. We established two types of calculations described as follow: a) first, given a fixed concentrations we varied the length of the device. For this setup we have fixed two concentrations $[\text{Ni}]_1 = 0.48 \%$ and $[\text{Ni}]_2 = 0.87 \%$ and varied the device length².

¹Figure 4.1 shows the most stable and symmetric Ni adsorption sites simultaneously.

²As a reference, a concentration of 0.48 % corresponds to approximately 29700 Carbon atoms and 5400 Hydrogen atoms.

(b) second, given a fixed length of the device we varied the concentrations. For this setup we have fixed two lengths $L_1 = 97.425$ nm and $L_2 = 194.85$ nm. The number of atoms contained in the disordered systems range from 3255 to 35130 atoms. A typical calculation goes as follow: (1) We select the types of segments that will be present; the pristine segment and segments containing the impurity. (2) We then fixed the total number of segments (and consequently fix the concentration and length). The device is then assembled by randomly arranging the building blocks.

Given the disordered nature of the system the results presented here are an average of up to 100 such calculations. We organized this chapter starting with the presentation and discussions of the disordered transport results based on the Ni@AGNR-1 structure, followed by the Ni@AGNR-s structure. Finally, results and discussions of transport at certain energies of interest based on the Ni@AGNR-1 system, followed by the Ni@AGNR-s system are presented.

4.1 Disordered transport based on Ni@AGNR-1

An overview of transmission calculations performed for the two setups described before are presented in figures 4.2 (without SO) and 4.3 (with SO). Let us start by analysing figure 4.2. It shows a set of plots of transmission coefficients as a function of energy for fixed concentrations of $[\text{Ni}]_1 = 0.48$ % (column a), $[\text{Ni}]_2 = 0.87$ % (column b) and fixed device lengths of $L_1 = 97.425$ nm (column c) and $L_2 = 194.85$ nm (column d). The spin-conserved transmission coefficients ($T_{\uparrow\uparrow} = T_{\downarrow\downarrow}$) compared by columns display similarities except for the two last plots (see Figs.4.2 (c-3) and (c-4)) belonging to the L_1 setup where a very high and sharp peak of spin-conserved transmission appears slightly below the Fermi level in Fig. 4.2 (c-3), whereas Fig. 4.2 (c-4) exhibit two peaks below E_F ³. If we analyse each column according to the increase of concentration or length we can observe that the spin-conserved transmission probabilities decrease slightly in each setup, which is a tendency expected since the number of Ni impurities in the ribbon increases, resulting in smaller transmission probabilities due to the large numbers of scattering events. Finally, we notice a transmission for energies close to -1 eV and above the Fermi level in all plots. This means that the conduction band is close to transparent. As it happened in the single impurity case, this can be associated with the lack of Ni-*d* states in this energy region.

Let us now turn our attention to figure 4.3 where the SO effect was taken into consideration for all calculations. It shows the spin-conserved ($T_{\uparrow\uparrow} = T_{\downarrow\downarrow}$) and spin-flip ($T_{\uparrow\downarrow} = T_{\downarrow\uparrow}$) transmission probabilities curves as a function of energy for fixed concentrations of $[\text{Ni}]_1 = 0.48$ % (column a), $[\text{Ni}]_2 = 0.87$ % (column b) and fixed device lengths; $L_1 = 97.425$ nm (column c) and $L_2 = 194.85$ nm (column d). For all

³We believe, that in these case, the density of defects is so large that there is very little room for randomly organize the defects. If this gives rise to a mini-band.

setups (columns a, b and c) both transmission curves are rather similar except for the last column ($L_2 = 194.85$ nm) which displays significantly reduced transmission intensities. Once again, transmission curves are slightly different in Fig. 4.2 (c-3) and Fig. 4.2 (c-4) since those plots exhibit sharp peaks at energies slightly below the Fermi level. Moreover, we observe that spin-conserved curves between energies -1 and 1 eV decline with the increase of concentration or length of the device while spin-flip curves become greater in the same energy range for all plots, in particular, a larger tendency can be seen in Fig. 4.2 (c-3) and Fig. 4.2 (c-4).

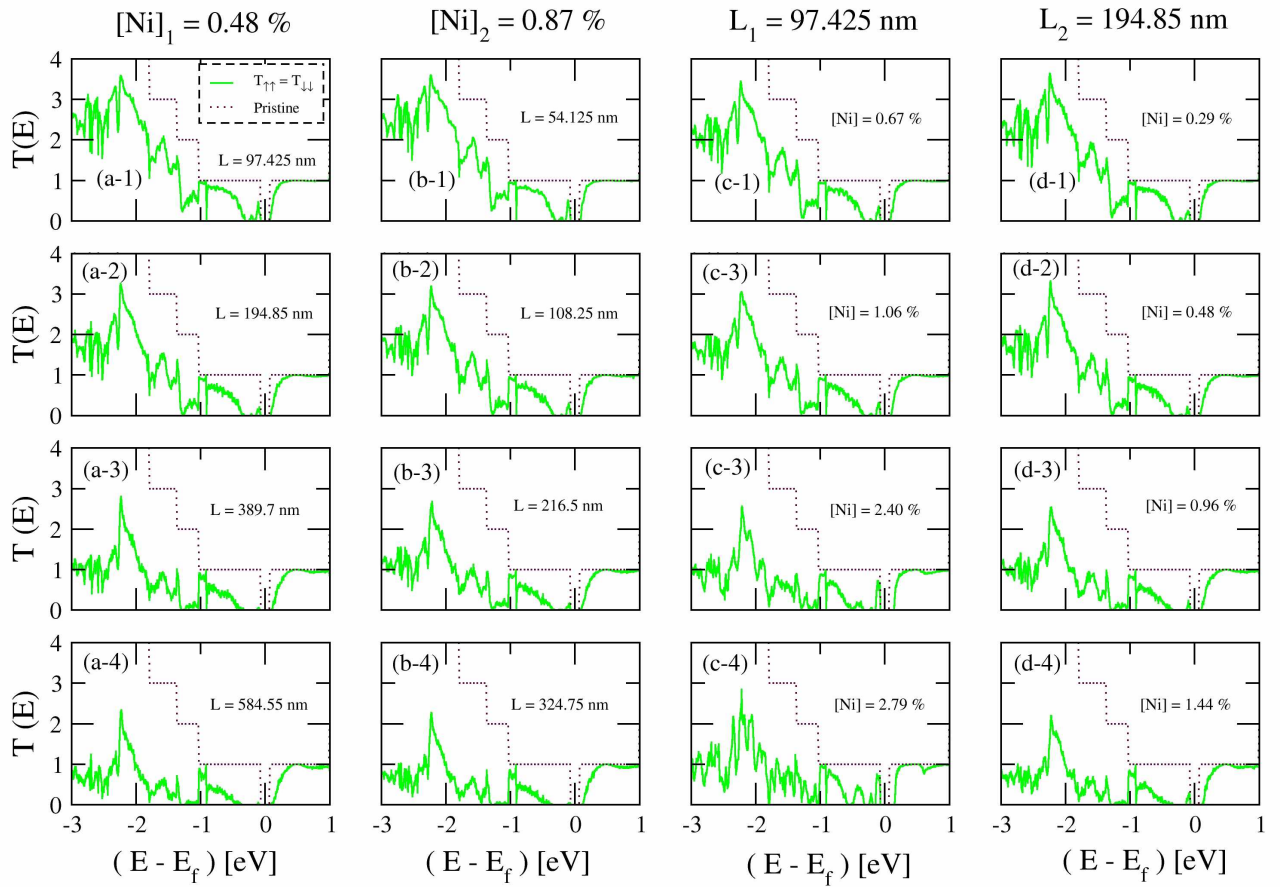


Figure 4.2: Spin-conserved transmission coefficients ($T_{\uparrow\uparrow} = T_{\downarrow\downarrow}$) without spin-orbit coupling as a function of energy of disordered ribbon based on Ni@AGNR-1 structure. (a) At fixed concentration of $[\text{Ni}]_1 = 0.48$ %; (b) At fixed concentration of $[\text{Ni}]_2 = 0.87$ %; (c) At fixed nanoribbon length of $L_1 = 97.425$ nm and (d) At fixed nanoribbon length of $L_2 = 194.85$ nm. Dashed lines correspond to the transmission coefficients for a pristine AGNR.

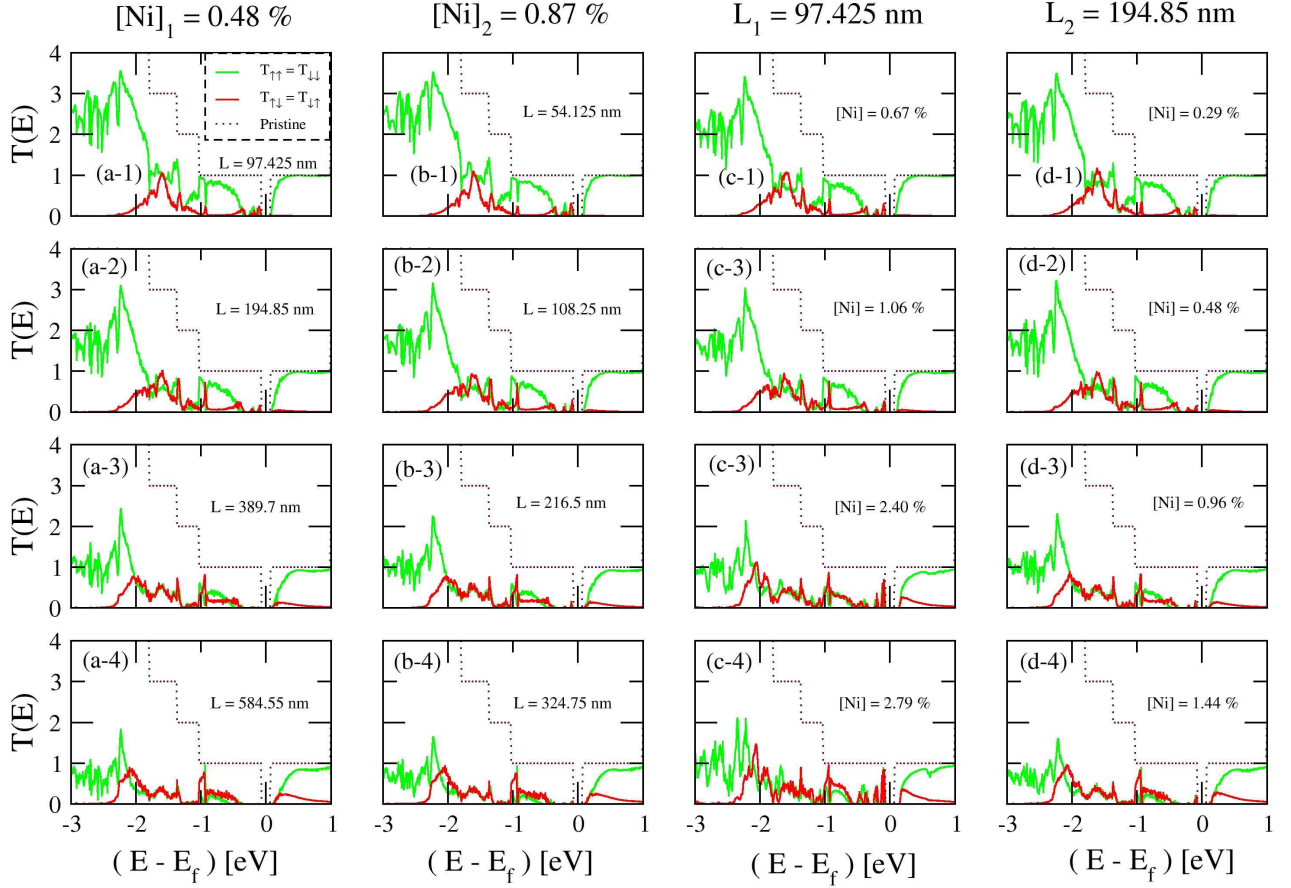


Figure 4.3: Spin-conserved transmission coefficients ($T_{\uparrow\uparrow} = T_{\downarrow\downarrow}$) with spin-orbit coupling as a function of energy of disordered ribbon based on Ni@AGNR-1 structure. (a) At fixed concentration of $[\text{Ni}]_1 = 0.48 \%$; (b) At fixed concentration of $[\text{Ni}]_2 = 0.87 \%$; (c) At fixed nanoribbon length of $L_1 = 97.425 \text{ nm}$ and (d) At fixed nanoribbon length of $L_2 = 194.85 \text{ nm}$. Dashed lines correspond to the transmission coefficients for a pristine AGNR.

Thusfor we have discussed superficially transport results to observe general tendencies of transmission curves for calculations with and without SO effect. We found that the behaviour of transmission curves are almost non-dependent on the setups used except for a few particular cases. In order to make a better comprehension of the effect of SO coupling over the transmission curves we have chosen a representative setup to be analysed in the next subsection, at fixed concentration of $[\text{Ni}]_1 = 0.48 \%$, leaving the other setups to be seen in the Appendix.

4.1.1 Transmission versus Length at fixed concentration of 0.48 %

Figure 4.5 shows the transmission coefficients for $[\text{Ni}]_1 = 0.48 \%$, comparing the cases with (column a and c) and without (column b) SO. Overall, what can be noticed from the picture is that the total conduction is approximately the same with or without SO. This means that the SO interaction does not introduce a new source of backscattering (at least not significantly), except at those energies where Fano resonances were observed (approximately between 0 and -1 eV). A pictorial view of this effect can be considered as shown in Fig.4.4. In the case of no-SO interaction (Fig.4.4(a)) electrons incoming (say with spin up) can either be transmitted or reflected without having its spin flipped. In the case of SO interaction (Fig.4.4(b)), during the scattering process, the electron can be elastically scattered conserving its spin or it smoothly precesses to flip its spin (either transmitted or reflected). In that sense total up (down) transmission at the drain has a contribution from in-coming down (up) spin electrons. At the same time, by analysing the spin-conserved and spin-flip transmission coefficients separately there are significant changes.

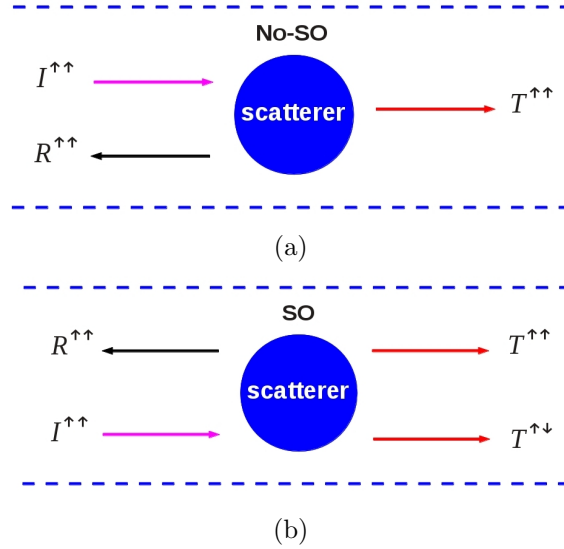


Figure 4.4: Scattering process in presence of a scatter element; (a) Without influence of SO interaction; (b) With influence of SO interaction.

In summary, we observed that the trend of reduction of the spin-conserved transmission probabilities without SO takes place when the device length increases, this behaviour is expected as the number of impurities and thus the number of scattering events has been increased. Moreover, it is observed that at -1 eV and between 1 to

0 eV the spin-conserved rather constant. On the other hand, it has been observed that spin-flip curve with SO increases above the Fermi level when the device length was increased while at energies below the Fermi level the spin-flip either increases or reduces its intensity.

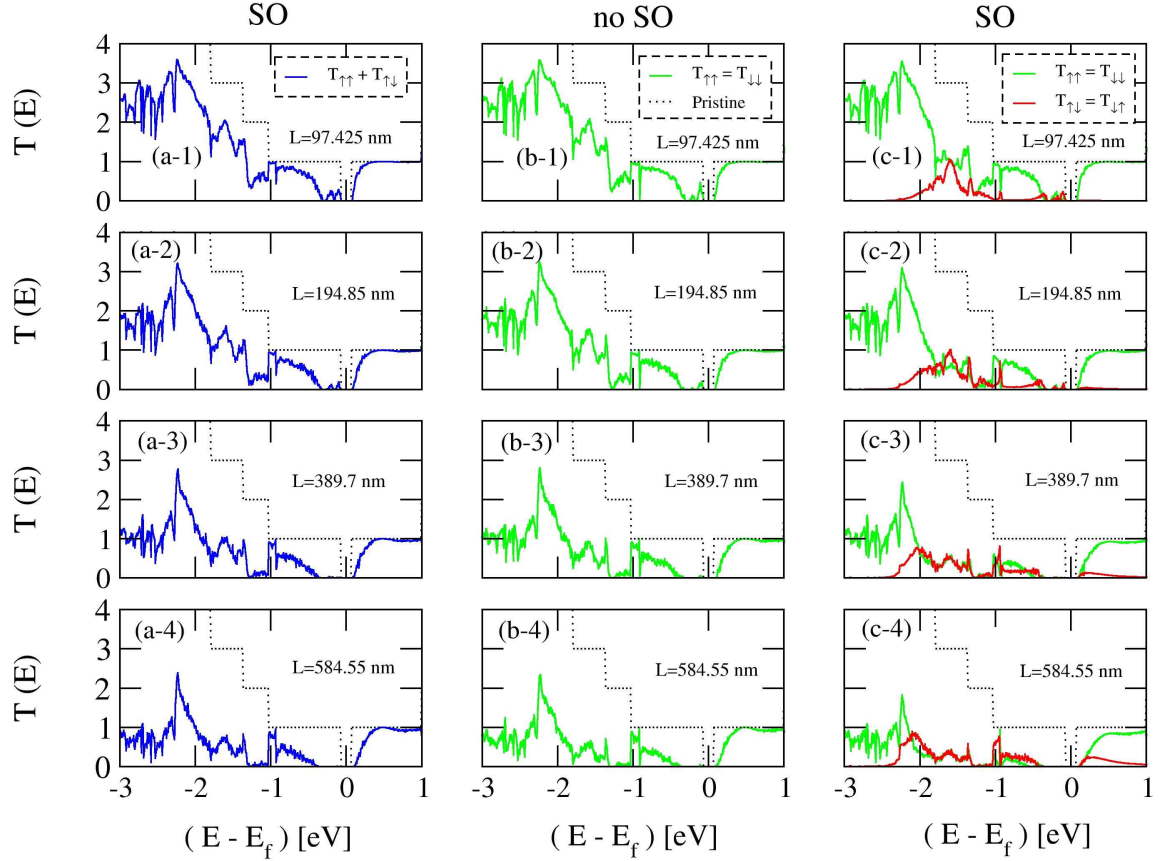


Figure 4.5: Disordered transport of nanoribbon at fixed concentration of $[\text{Ni}]_1 = 0.48 \%$. (a) Total conductance ($T_{\uparrow\uparrow} + T_{\downarrow\uparrow}$); (b) Spin-conserved ($T_{\uparrow\uparrow} = T_{\downarrow\downarrow}$) transmission probabilities without SO coupling; (c) Spin-conserved ($T_{\uparrow\uparrow} = T_{\downarrow\downarrow}$) and spin-flip ($T_{\uparrow\downarrow} = T_{\downarrow\uparrow}$) transmission probabilities with SO coupling. Dashed lines correspond to transport in the pristine AGNR.

We will close this section with a comparison of transmission probabilities based on the most stable and symmetric single defect blocks. For this purpose we plotted the setup at fixed concentration of 0.48 % and also we considered the cases with and without SO interaction as is depicted in figure 4.6. The column a and b illustrate transmissions with SO for the stable and symmetric cases, respectively. On the other hand column c and d display transmissions without SO for the stable and symmetric cases, respectively.

We conclude that the type of defect, which the disordered device is based, lead to strong influence in the total transmission coefficients. Furthermore, if the SO effect is considered it is observed that spin-conserved curve in columns b and c (based on symmetric blocks) tends to be zero at energies between -1.5 and 0 eV which is not the case in columns a and c (based on stable blocks). This means there is a complete suppression of the conduction channel (localized regime), a feature that has been observed before by Lewenkopf [66]. The inclusion of SO interaction does not alter this trend.

The total transmission is significantly smaller and it can be explained from the single impurity case where the d state is strongly hybridized with the AGNR and causes significant decrease of the conductance over the wider energy range.

Finally, according to the results discussed recently it is interesting to study which tendency would be followed by the spin-flip transmission curve at specific intervals of energy since as we have seen it has distinct behaviours.

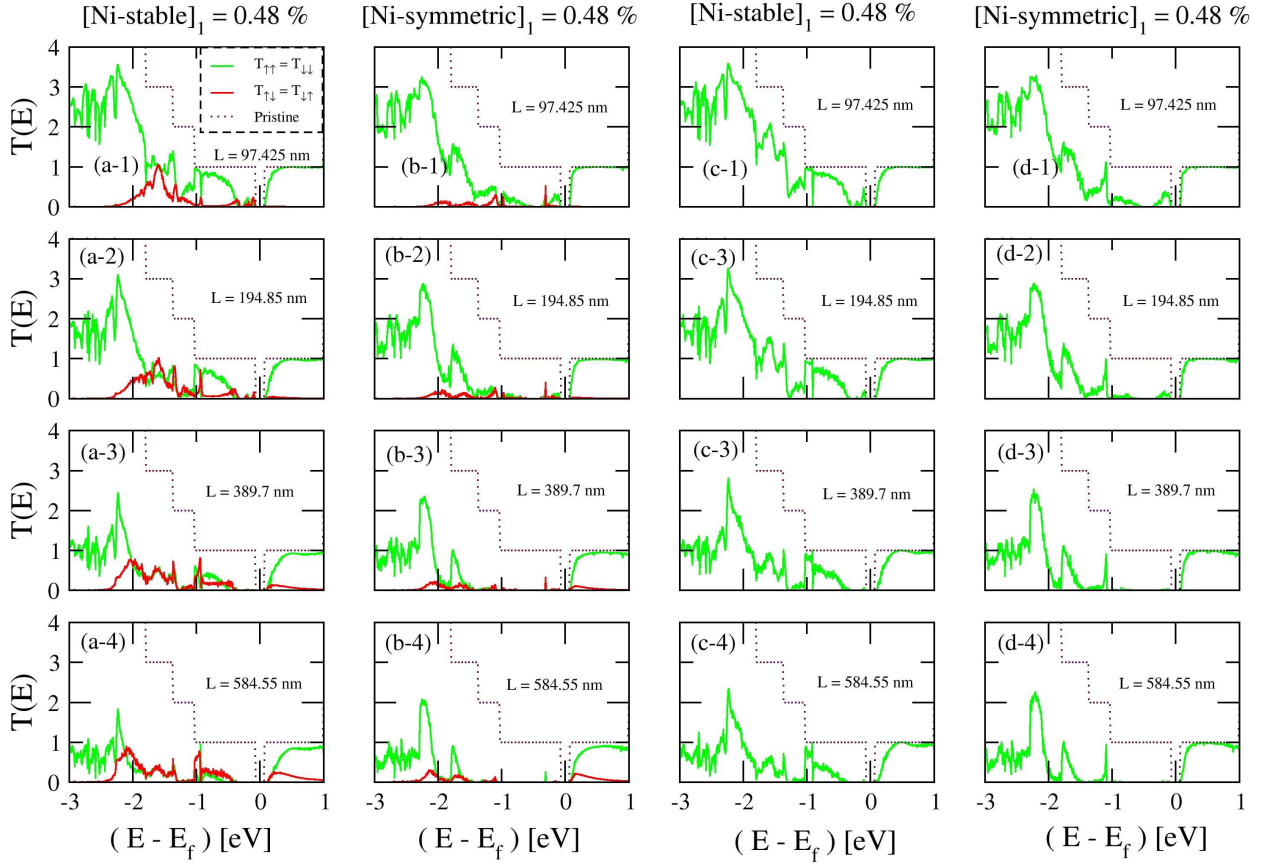


Figure 4.6: Spin-flip ($T_{\uparrow\downarrow} = T_{\downarrow\uparrow}$) and spin-conserved ($T_{\uparrow\uparrow} = T_{\downarrow\downarrow}$) transmission coefficients as a function of energy of disordered ribbon based on Ni@AGNR-1 and Ni@AGNR-s structures at fixed concentration of $[\text{Ni}]_1 = 0.48 \%$. (a) Based on Ni@AGNR-1 with SO; (b) Based on Ni@AGNR-s with SO; (c) Based on Ni@AGNR-1 without SO and (d) Based on Ni@AGNR-s without SO. Dashed lines are the transmission coefficients for pristine AGNR.

4.2 Transport at energies of interest - Ni@AGNR-1

The aim of this section is to divide the total energy spectrum in representative intervals of energy to study the trend of the spin-conserved and spin-flip transmission coefficients at those specific energy regions when the device length is increased, as usual we considered the SO effect in those calculations.

In figure 4.7 we show eight regions of energy, one above the Fermi level (E_0) and the others below the Fermi energy (E_1, \dots, E_7). Table 4.1 shows the minimum and maximum values in eV of every energy interval illustrated in figure 4.7

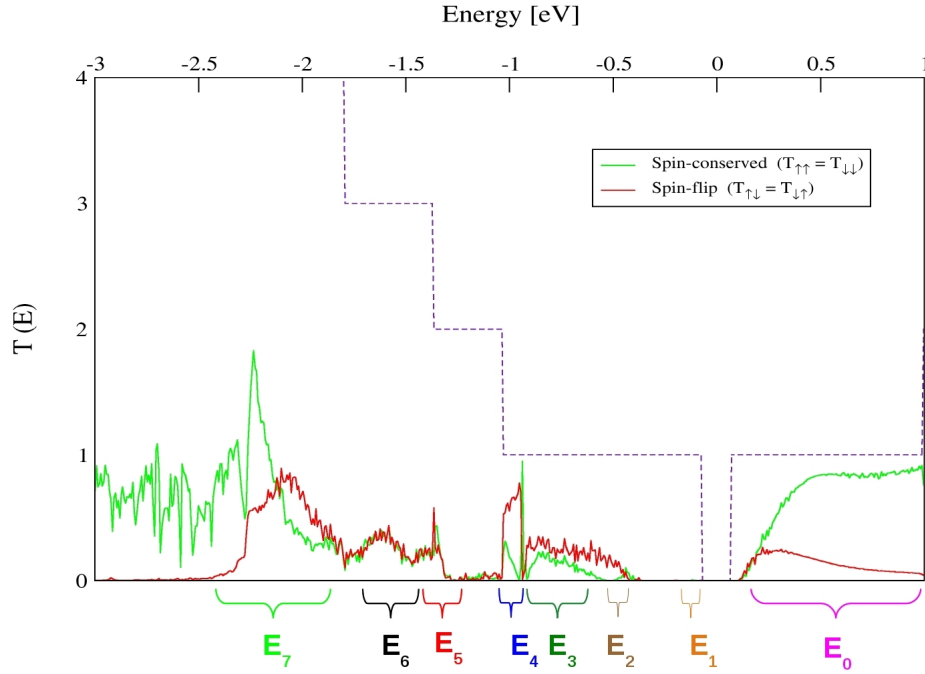


Figure 4.7: Schematic illustration of energy intervals chosen to study the trend of the spin-conserved and spin-flip transmissions.

Energy region	$[E_{min}, E_{max}]$ [eV]
E_0	[0.1485, 0.4639]
E_1	[-0.1459, -0.0758]
E_2	[-0.5104, -0.4122]
E_3	[-0.9309, -0.5805]
E_4	[-1.0506, -0.9309]
E_5	[-1.4075, -1.1622]
E_6	[-1.7159, -1.4075]
E_7	[-2.4169, -1.8001]

Table 4.1: Values of the energy regions considered in Fig. 4.7.

As we pointed out in the previous section, the transmission curves mostly followed the same trend for each setup described at the beginning of this chapter, so in this section we chose as a sample one of them: the case at fixed concentration of 0.48 % - in order to perform the transport calculations at those specific energy ranges of interest and including the SO interaction too.

In figure 4.8 we can see the spin-conserved transmission coefficients without SO effect as a function of the device length for the set of energy intervals. By a rough inspection we found that all of them tended to decrease in intensity when the device length was increased. These results were expected because in our setup the fact that the device grows in size means that the number of impurities also has increased so we have a large number of scattering events and as a consequence the reduction of transmission probabilities.

Clearly, we identified that transmission in E_7 (green circle) and E_6 (black triangle right) decreased equally between each other and faster than the other intervals of energy. Moreover, we can observe that in E_2 (brown diamond), E_5 (red triangle left) and E_1 (orange square) transmission were practically suppressed when the device length is the maximum one considers (~ 600 nm). Another interesting observation is that in E_3 (green triangle up) and E_6 (black triangle right) the spin-conserved converged to almost the same transmission intensity.

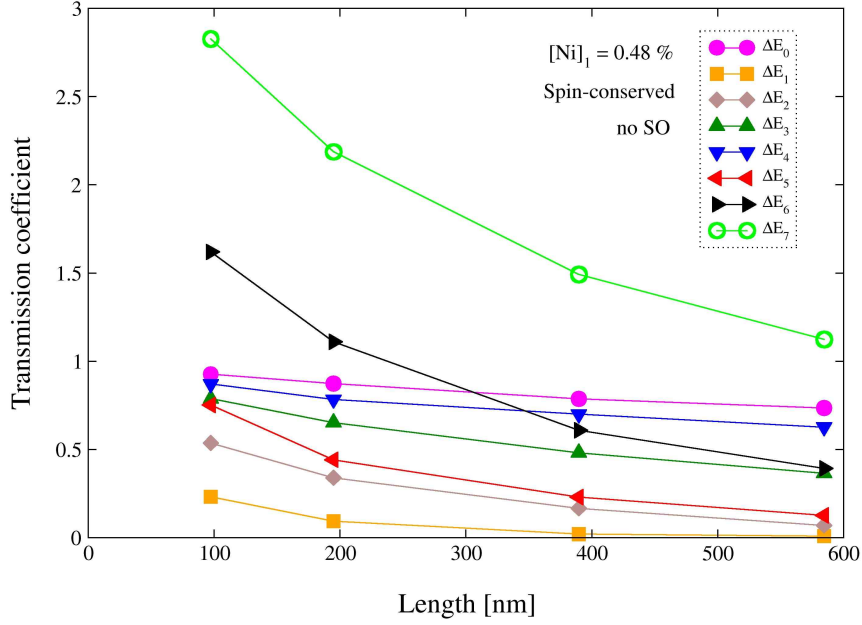


Figure 4.8: Spin-conserved transmission coefficients versus length of the disordered device for the set of energy ranges of interest calculated without take into consideration the SO interaction.

In figure 4.9 (a) and (b) we can see the spin-conserved and spin-flip transmission coefficients with SO interaction, respectively, as function of the device length for the set of energy ranges. In case of spin-conserved we found that all energy ranges follow almost the same trend compared with case without SO but with a little bit changes except in E_6 which now behaves more like in E_4 and not like in E_7 as the no SO case. By looking more carefully we can notice that in E_6 , E_5 , E_4 and E_3 spin-conserved converged to around a point which is lower and slightly faster than without SO case while in E_2 and E_1 the transmission practically disappeared when the device length is ~ 600 nm. Also, in E_7 it decreased until lower levels compared with case where the SO is not considered while in E_1 it is almost zero at each device length.

In case of the spin-flip transmission coefficients (see Fig.4.9 (b)) we observe that the energy intervals in E_0 , E_3 , E_4 and E_7 it increased and in E_1 and E_6 it decreased when the device length grew in size. A particular tendency is observed in E_2 and E_5 in which it began at different transmission coefficients then increased at ~ 200 nm and finally decreased at the same transmission intensity at ~ 600 nm. In E_0 and E_3 it started at the same point then increased with almost the same rates but different transmission intensity and converged to approximately the same transmission point. In E_2 and E_4 it started also at the same transmission level but tended to different

transmission intensities where in E_2 it converged to values similar to the ones in E_5 whereas in E_4 it converged to the same transmission intensity as in E_7 . Also, in E_7 and E_1 it went from the same transmission level but while in E_7 it increased to the same transmission coefficient as in E_4 at ~ 600 nm, in E_1 it decreased fast to zero transmission. Finally, E_6 is the unique energy range where it began at higher level and decreased fast until the same transmission coefficient as in E_3 at device length of ~ 600 nm.

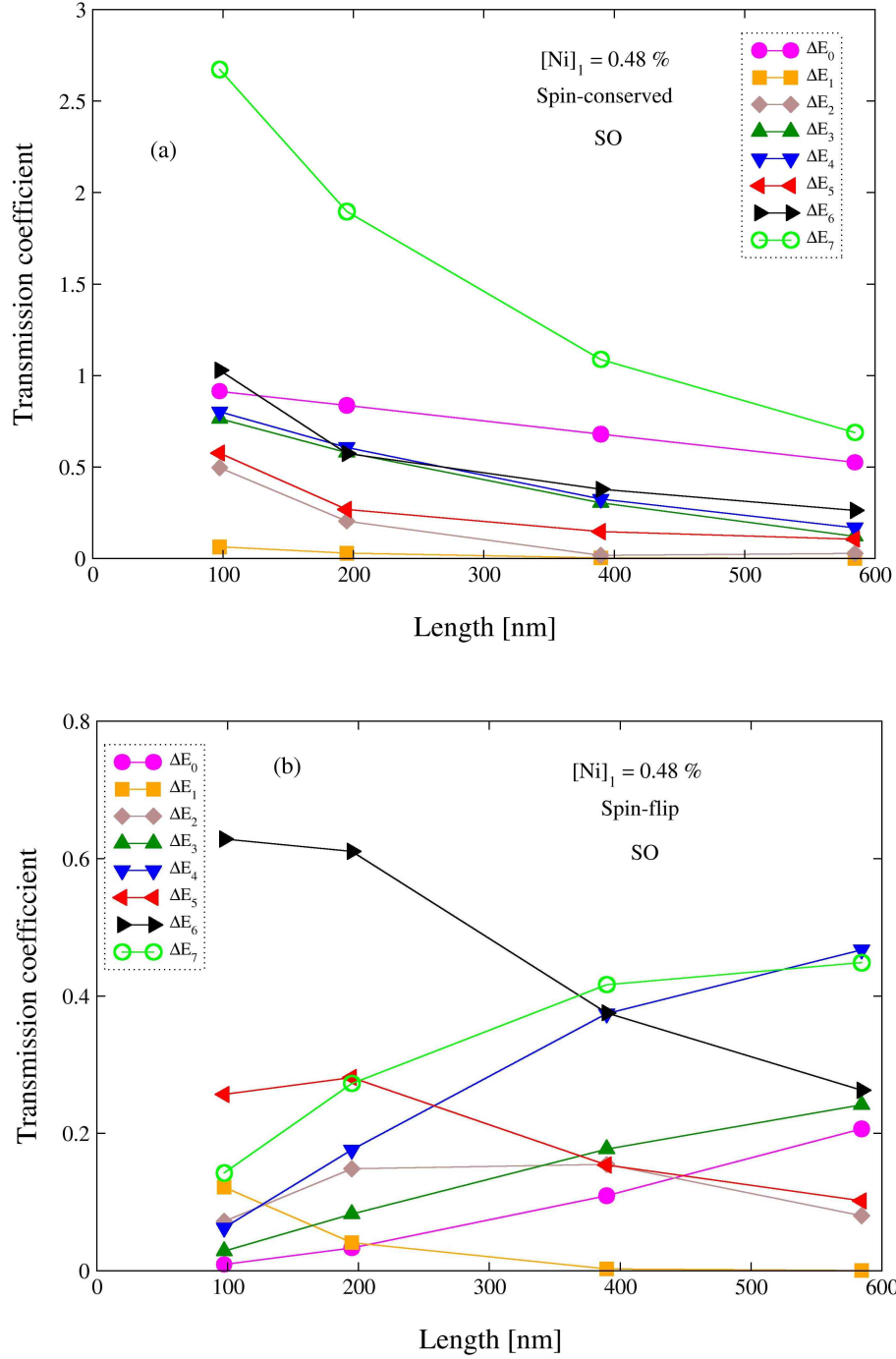


Figure 4.9: Transmission coefficients versus length of the disordered device for the set of energy ranges of interest calculated considering the SO interaction. (a) Spin-conserved transmission coefficients. (b) Spin-flip transmission coefficients.

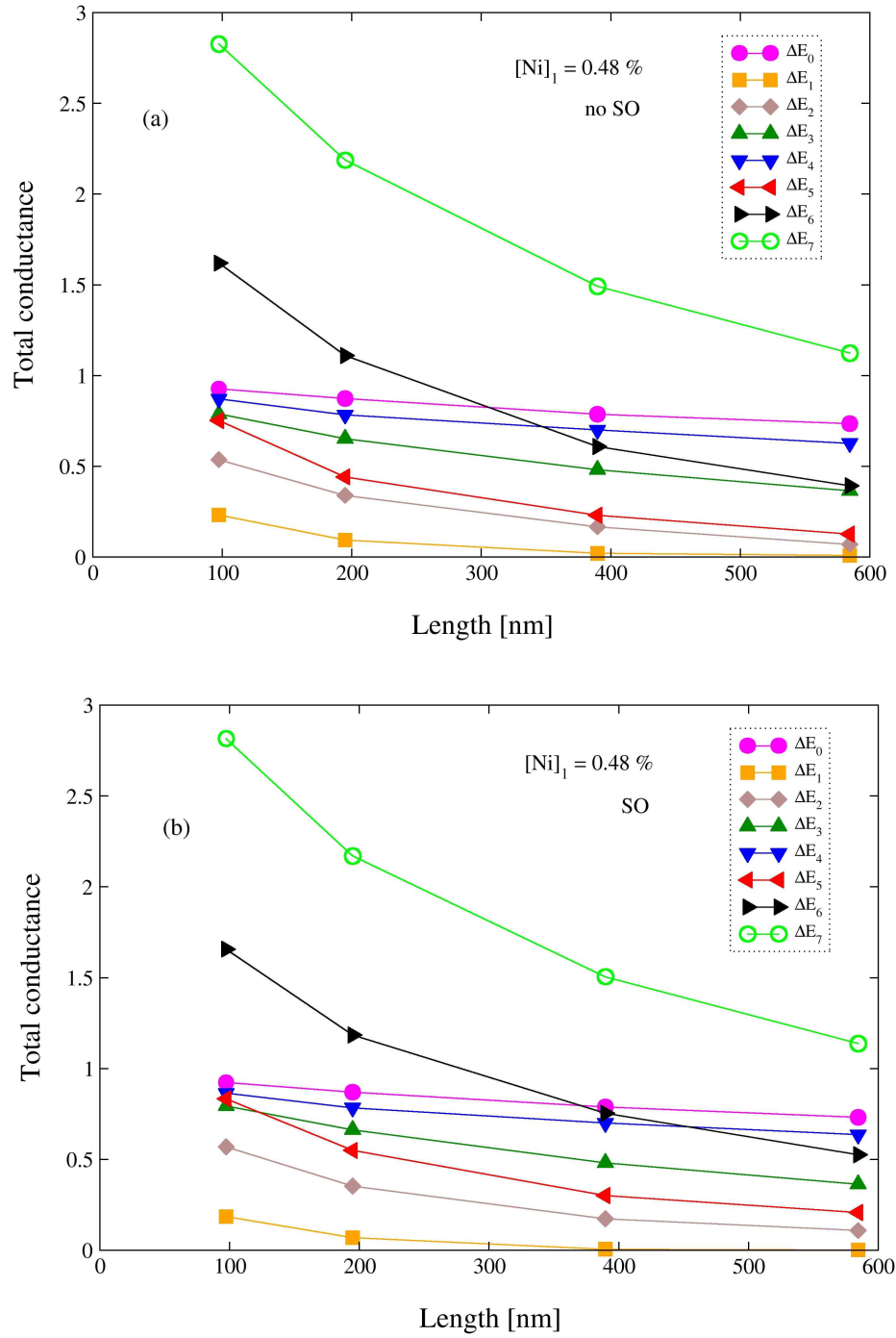


Figure 4.10: (a) Total conductance versus length of the disordered device with no SO effect. (b) Total conductance versus disordered device length with SO effect.

In figures 4.10 (a) and (b) we show the total conductance as function of the device length for cases without and with SO interaction, respectively. Both cases are very similar except in interval E_6 where the total conductance was slightly shifted to a high transmission coefficients at ~ 400 nm and ~ 600 nm as well as in interval E_5 . Furthermore, we should note that total conductance where the SO effect was not considered is equal to the spin-conserved transmission without taking into account the SO, shown early (see Fig. 4.8).

In figure 4.11 we presented the polarization (P) as a function of the disordered system length. This property serve as a reference to observe simultaneously the behaviour of the spin-conserved and spin-flip transmission probabilities of each energy ranges since it was defined as the normalized differences between both transmissions. For instance, $P = 0$ means that spin-conserved and spin-flip transmission coefficients are the same, $P > 0$ means spin-conserved is greater than spin-flip taking $P = 1$ as the upper limit where there is no spin-flip transmission coefficients and conversely $P < 0$ means spin-flip is greater than spin-conserved taking $P = -1$ as the lower limit where there is no spin-conserved transmission coefficients.

P in interval E_0 began at ~ 400 nm practically without spin-flip (\sim pure spin-conserved) transmission then it increased at low growth rates until becomes the third part of the spin-conserved at ~ 600 nm. In E_7 , P has shown a similar behaviour. In E_3 spin-flip transmission began with almost zero then it grew at higher rates than in E_7 to becomes greater than the spin-conserved transmission at ~ 600 nm. Also, in interval E_4 has shown a very similar trend. A particular behaviour was observed in E_2 in which spin-flip transmission began with small intensity then it increased at very high rates until becomes almost purely spin-flip at ~ 400 nm then it decreased until the same level of transmission as in E_4 at ~ 600 nm. Another peculiar trend was observed in energy ranges E_5 and E_6 in which spin-flip began with high transmission but at ~ 200 nm both transmissions (spin-flip and spin-conserved) become equivalent and keep that level until the end. Finally, contrary to all cases seen before E_1 is the only one energy range where there is an opposite behaviour which means that spin-flip began with higher intensity than spin-conserved then the spin-flip decreased until becomes less than the spin-conserved transmission coefficients.

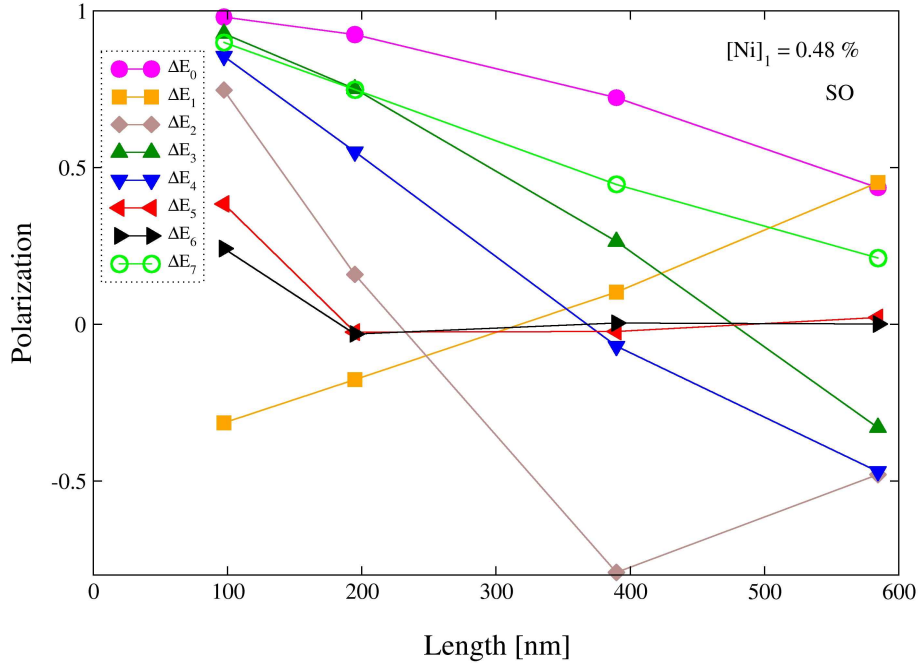


Figure 4.11: Polarization versus length of the disordered device with SO effect for the set of energy ranges of interest.

Spin relaxation length

In Fig.4.11 we observed different polarization trends of specific energy regions, some of them with expected tendencies - those which tend to zero when the device length increase - and others not expected. To compute the spin relaxation length we used the polarization for specific intervals of energy where the polarization follow expected tendencies, as depicted in Fig. 4.12. We should mention that further calculations where the device length have to be increased even more is necessary for those remaining energy regions where the polarization seems to oscillates before tend to zero.

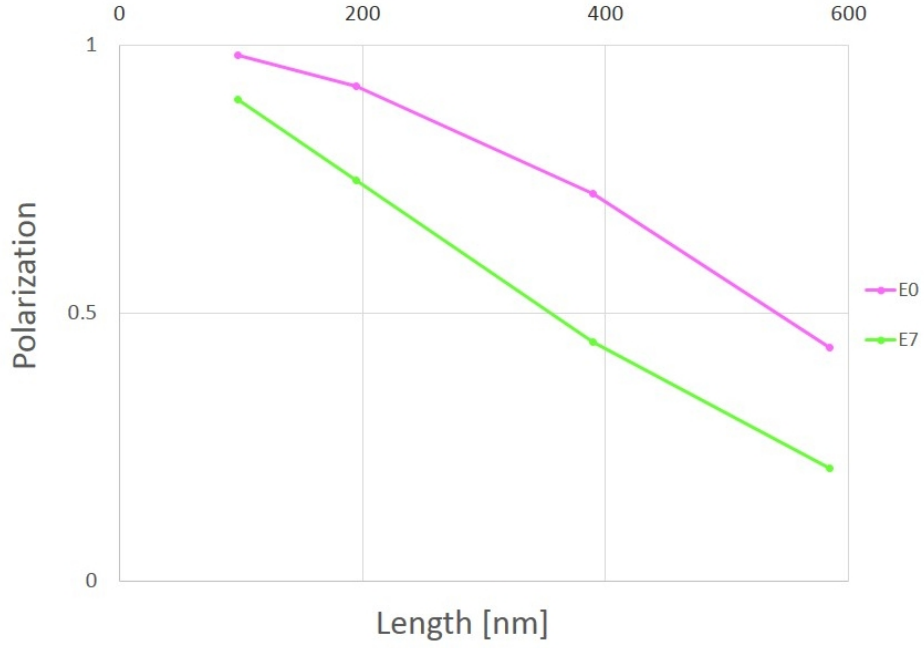


Figure 4.12: Polarization as a function of the device length for two energy regions (E_0 and E_7).

The transport regime of our disordered system is the Anderson localization regime because of the adatoms impurities. We calculated the spin relaxation length by fitting the data showed in Fig. 4.13 which show the natural logarithm of polarization as a function of the device length. In table 4.2 we showed the spin relaxation length obtained from Fig. 4.13.

Energy region	Spin relaxation length [nm]
E_0	588
E_7	333.3

Table 4.2: Spin relaxation length of the energy regions E_0 and E_7 .

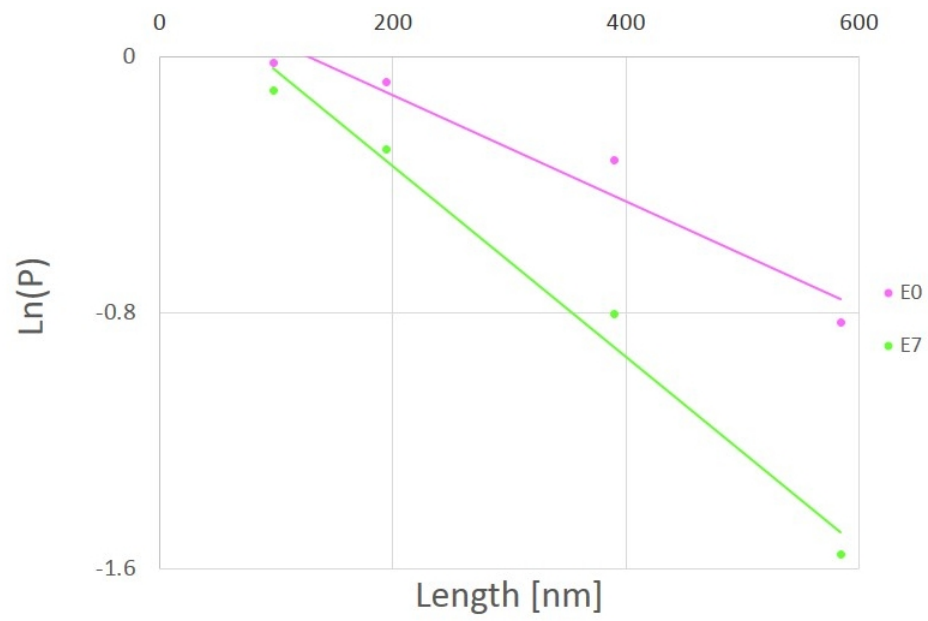


Figure 4.13: Natural logarithm of polarization versus the length of the device showing the data fitting curve.

4.3 Transport at energies of interest - Ni@AGNR-s

Now let us analyse the specific energy ranges for the disordered device based on the symmetric structure (Ni@AGNR-s). In figure 4.14 we have shown seven regions of energy for this case which is analogous but not identical to the case based on Ni@AGNR-1.

Table 4.3 shows the minimum and maximum values in eV of every energy interval as depicted in figure 4.7

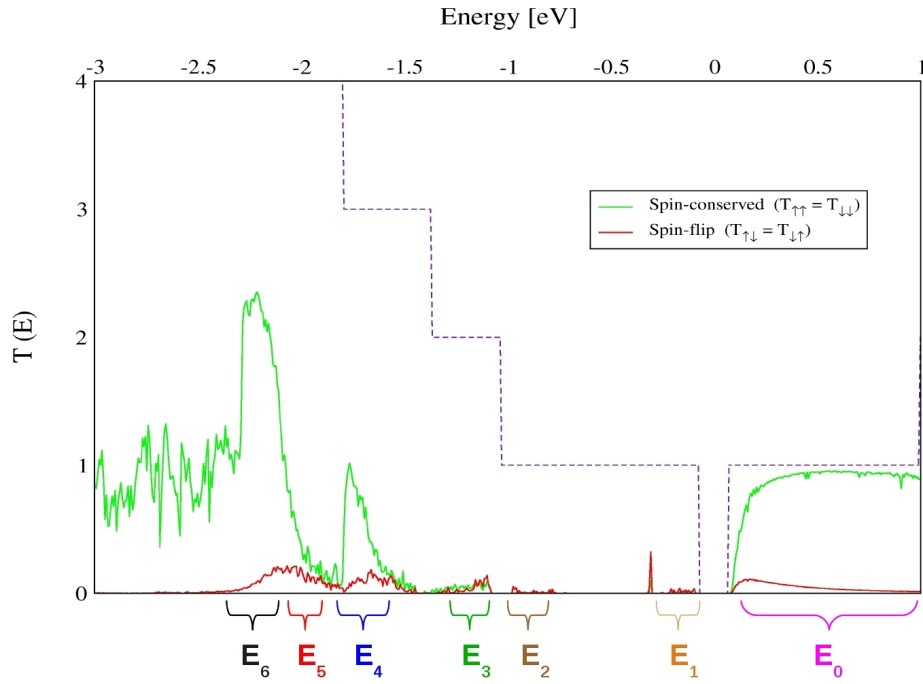


Figure 4.14: Schematic illustration of energy intervals chosen to study the trend of the spin-conserved and spin-flip transmissions.

Energy region	$[E_{min}, E_{max}]$ [eV]
E_0	[0.1345, 1.4172]
E_1	[-0.2440, -0.0688]
E_2	[-0.9710, -0.7837]
E_3	[-1.2533, -1.0641]
E_4	[-1.8000, -1.5267]
E_5	[-2.0325, -1.8912]
E_6	[-2.3327, -2.0303]

Table 4.3: Values of the energy regions considered in Fig. 4.14.

In figure 4.15 we observe the spin-conserved transmission coefficients without SO effect versus the device length for every energy regions. As expected, all of them tend to decrease in more or less intensity when the device grow in size. For example, in E_1 and E_2 it began with small transmission coefficients then were practically suppressed at ~ 400 and ~ 600 nm. In E_0 it experienced a very small reduction of transmission and can be considered constant. In E_6 , E_4 and E_3 it have approximately the same trend and decreased more quickly than in E_1 and E_2 . The differences of spin-conserved in those energy regions were in the initial and final transmission coefficient, to wit, in E_6 it ended at higher transmission than in E_4 and E_3 .

In E_5 it decreased quickly from ~ 100 nm to ~ 200 nm then decreased like in E_6 even though at different transmission coefficients. Also, It is interesting observe that besides in E_1 , E_2 , E_3 and E_5 it began at different transmission it converged to almost the same very small transmission (~ 0) at ~ 600 nm in those energy regions. Finally, beside in E_0 and E_4 it began at same transmission it diverged at the end in these energy intervals.

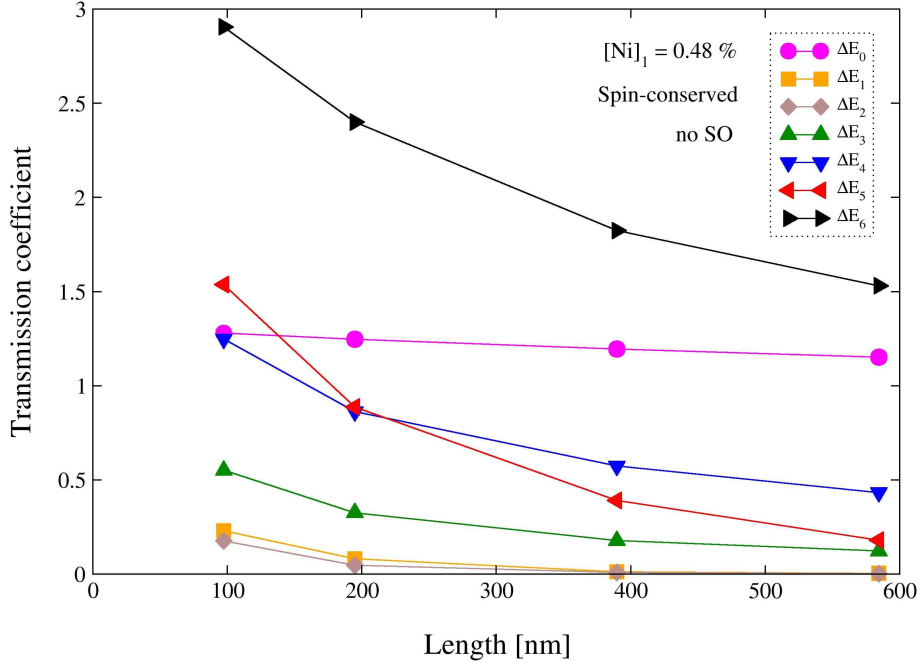


Figure 4.15: Spin-conserved transmission coefficients versus length of the disordered device for the set of energy ranges of interest calculated without take into consideration the SO interaction.

In figures 4.16 (a) and (b) we can see, for each energy intervals, the spin-conserved and spin-flip transmission coefficients as a function of the device length, respectively, obtained considering the SO coupling. In case of the spin-conserved transmission all energy ranges are very similar to the case with no SO.

In case of the spin-flip transmission coefficients in ranges E_0 , E_4 , and E_6 it tends to increase. In E_3 it tends to decrease and in E_1 , E_2 , and E_5 it exhibited mixed trends. Let us describe this in more details: in E_0 it began with no spin-flip transmission then it increased quickly until almost reach same transmission coefficients as in E_4 and E_5 at ~ 600 nm. In E_1 and E_2 it began at similar transmission then in these intervals it increased a little bit at ~ 200 nm and finally it decreased slowly until practically disappear at ~ 600 nm. In E_3 it experienced quickly reduction of transmission. In E_4 it increased slowly until reach similar transmission level as in E_5 at ~ 600 nm. In E_5 it began at similar transmission like in E_3 then it increased at ~ 200 nm and at the end it decreased slowly to the same transmission as in E_4 . Lastly, in E_6 it exhibited the fastest increasing beginning from equal transmission as in E_2 and reaching the highest transmission at ~ 600 nm.

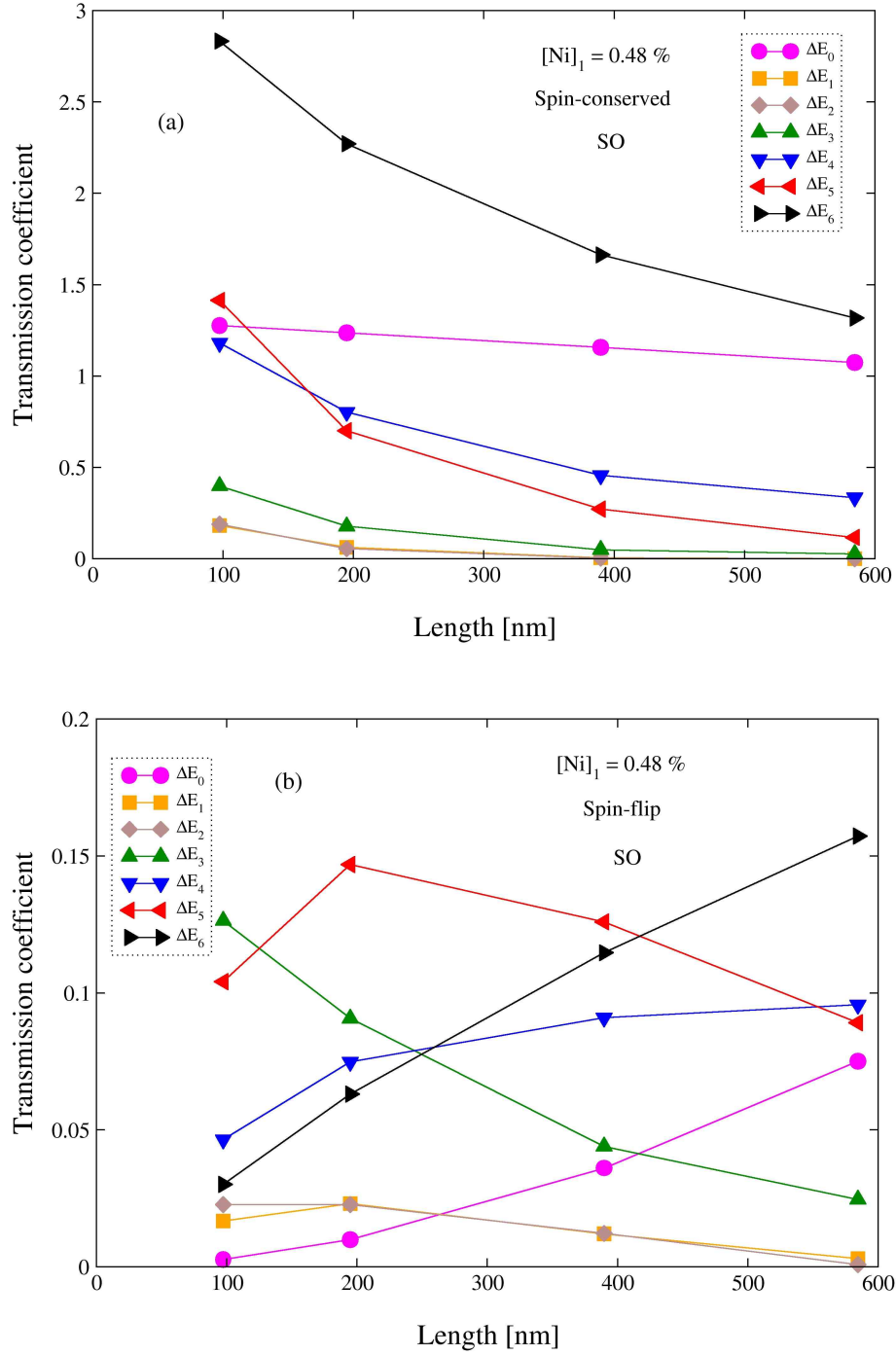


Figure 4.16: Transmission coefficients versus length of the disordered device for the set of energy ranges of interest calculated considering the SO interaction. (a) Spin-conserved transmission coefficients. (b) Spin-flip transmission coefficients.

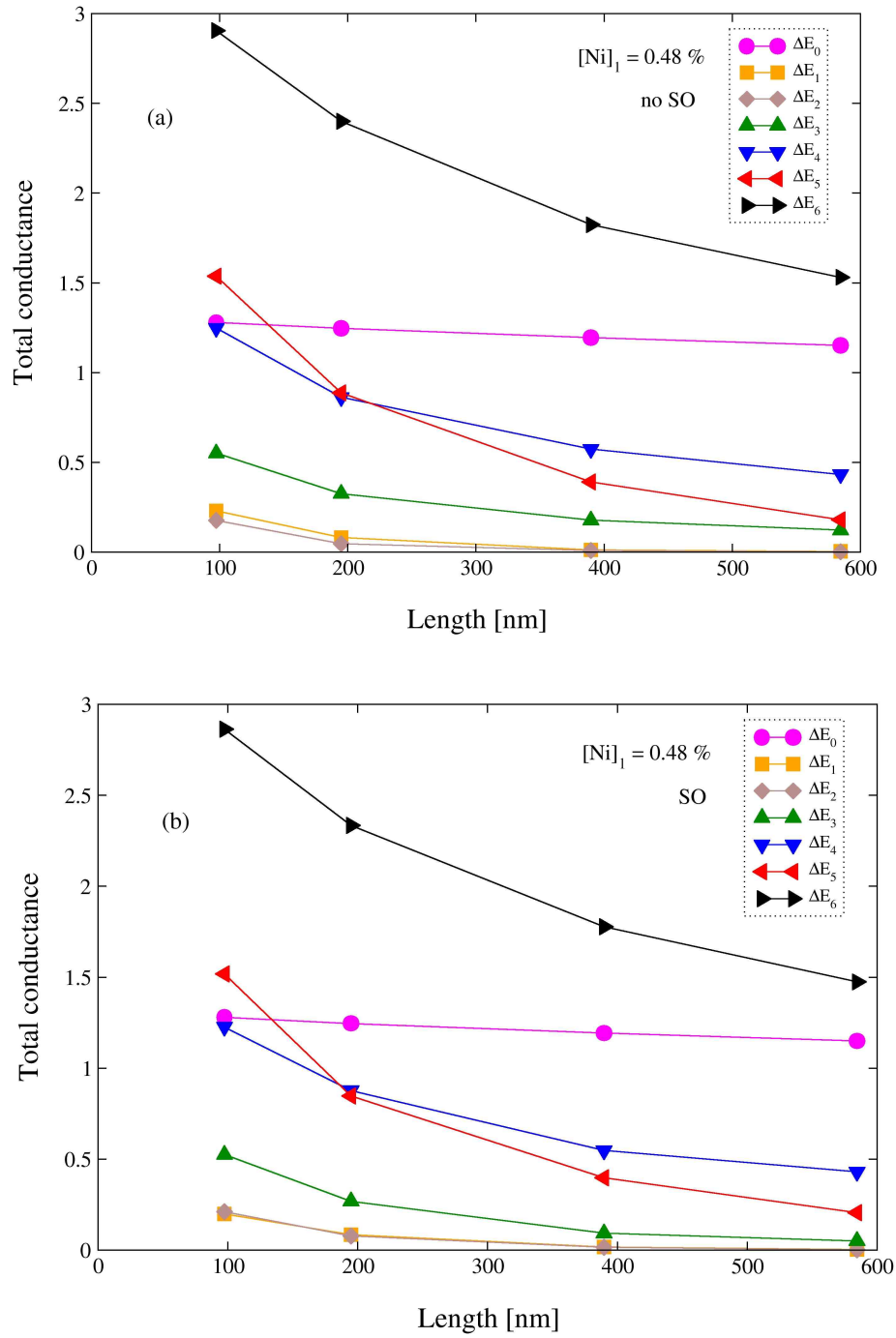


Figure 4.17: (a) Total conductance versus length of the disordered device with no SO effect. (b) Total conductance versus disordered device length with SO effect.

In figures 4.17 (a) and (b) the total conductance as a function of the disordered device length for cases without and with SO effect are shown, respectively. Both plots for the total conductance are very similar to each other.

In figure 4.18 is presented the polarization (P) versus the device length. We found that except for E_5 in the others P began with very small spin-flip transmission (in E_1 , E_2 , E_4 and E_5) and almost zero spin-flip transmission (in E_0 and E_6). In E_0 and E_6 the spin-flip increased slowly and reached small transmission. A similar behaviour was experienced by E_4 but with a bit more transmission intensity at the end (~ 600 nm). In E_5 we observe that it increased quickly until transmission level close to E_3 . In E_1 was displayed a very interesting behaviour starting from almost nothing spin-flip and reaching almost purely spin-flip at ~ 600 nm. E_2 exhibit a peculiar trend where it began with small spin-flip then it increased quickly until high spin-flip (~ 400 nm) and at the end decreased fast to spin-flip transmission close to E_3 . Finally, E_3 is the only which began with higher spin-flip transmission than others then it increased slowly until be comparable to the spin-conserved at ~ 400 nm and ~ 600 nm.

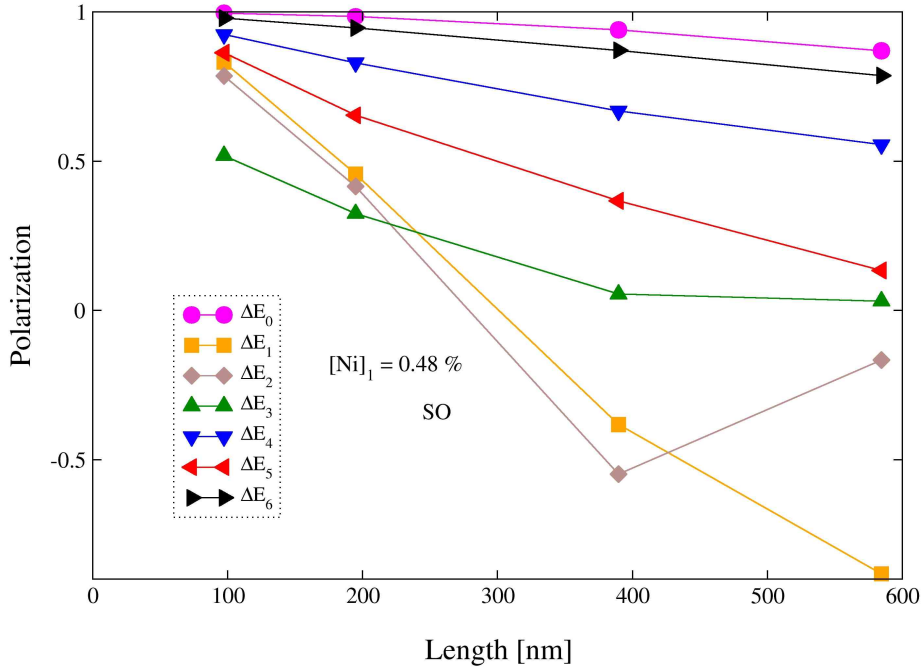


Figure 4.18: Polarization versus disordered device length with SO effect for the set of energy ranges of interest.

Spin relaxation length

In this case, we also observed in Fig.4.18 different polarization trends of the specific energy regions. To compute the spin relaxation length we used the polarization for specific intervals of energy where the polarization follow expected tendencies, as depicted in Fig. 4.19, in this case we identified 5 intervals of energy.

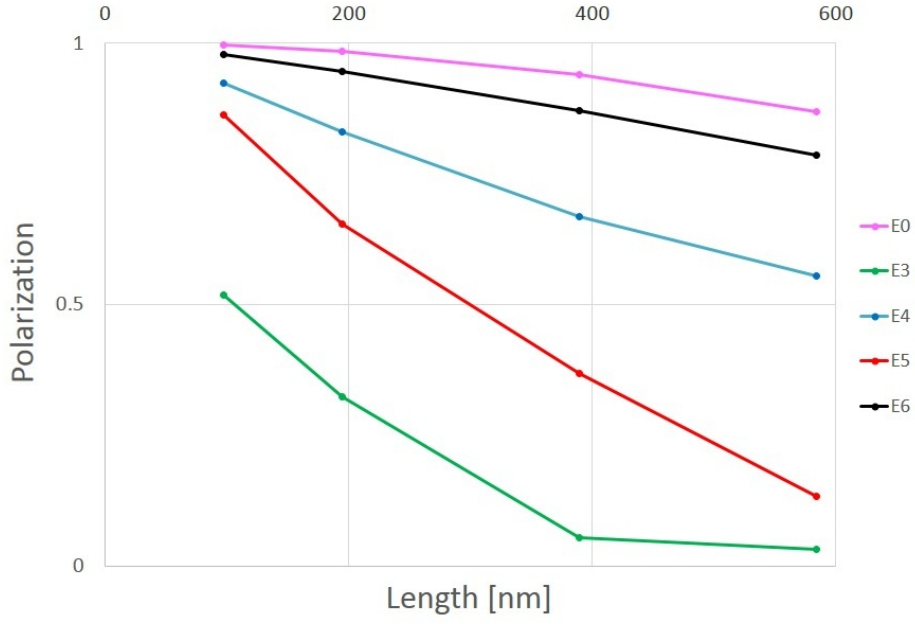


Figure 4.19: Polarization as a function of the device length for five energy regions (E_0 , E_3 , E_4 , E_5 and E_6).

We calculated the spin relaxation length by fitting the data showed in Fig. 4.20 which show the natural logarithm of polarization as a function of the device length. In table 4.4 we showed the spin relaxation length obtained from Fig. 4.20.

Energy region	Spin relaxation length [nm]
E_0	3333.3
E_3	163.9
E_4	909
E_5	263.2
E_6	2500

Table 4.4: Spin relaxation length of the energy regions E_0 , E_3 , E_4 , E_5 and E_6 .

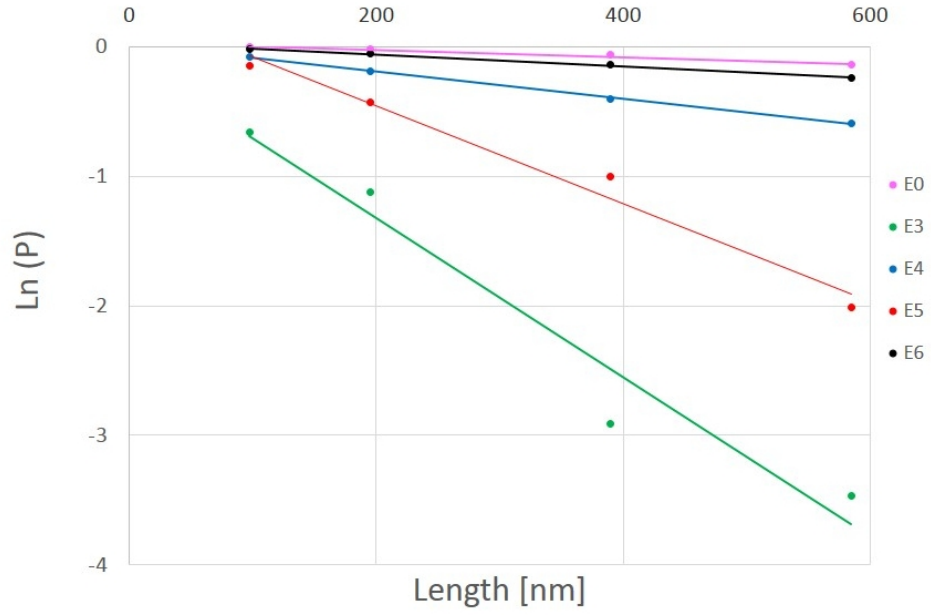


Figure 4.20: Natural logarithm of polarization versus the length of the device showing the data fitting curve.

Chapter 5

Conclusions

In this dissertation we studied the electronic and spin-dependent transport properties of graphene nanoribbons of type armchair with single adsorbed transition metal atoms as defects, as well as, spin-dependent transport of realistic graphene nanoribbons devices built based on the single adatom structure by means of a combination of DFT and NEGFs methods. We focused on nickel and iridium as adatoms for the single defect case and only nickel adatom for the disordered case. We have demonstrated that it is possible to study from first-principles the electronic transport properties of disordered systems in the presence of SO interaction.

At the equilibrium geometry we have shown that Ni and Ir adatoms prefer hollow sites closed to the edge of AGNR. The band structure results showed (for both Ni and Ir single defect systems) that the splitting in the stable structure are greater than in the symmetric structure which are in agreement with the fact of the band splitting is a direct consequence of the lack of inversion symmetry of the structures (Rashba SO interaction) and manifested itself by a displacement of the bands along the wave vector axis.

The intensity of the spin-conserved (SC) and spin-flip (SF) transmission coefficients are a direct consequence of the relaxed adsorption sites of the adatoms which in turn causes the orbitals to change their localized nature. In particular, we point out that d orbitals of Ni and Ir result in strong dependences on the spin-conserved and spin-flip transmission probabilities specially around the valence energy region. Moreover, the lack of inversion symmetry owing to the adatom led to different SO coupling intensities observed as spin-flip transmission. Thus, in this work we conclude that it is worth studying Ni adatom as single defect on AGNR since even the reduction in spin-conserved transmission probabilities it is still greater than the exhibited by Ir adatom structures.

In case of disordered systems the transmission coefficients (SC and SF) for different setups - fixed concentration and device length varying length and concentration, respectively - have trends very close to each other. From transmission at specific energy

regions of interest even though in both cases (based on stable and symmetric single defect systems) the energy intervals are not the same we found similar tendencies.

Furthermore, from the Polarization (P) results we found that some energy regions are well behaved - P tends to zero when the device length increase - whereas the others exhibit unusual trends. We have shown that the spin relaxation lengths for those energy regions with well behaved polarization are very small compared with Graphene's spin relaxation length which is around 4500 nm. In case of the remaining intervals of energy where the polarization exhibit do not expected trends we need to address future works in order to get a better comprehension of the physics involved. We suggest further calculations where the device length have to be increased even more for those remaining energy regions where the polarization seems to oscillates before tend to zero.

Finally, we can conclude that even though disordered systems with Nickel as impurities exhibit large transmission coefficients compared with Iridium we still need very small concentrations of Ni impurities in a real device to get useful transmittance and large spin relaxation lengths, as well as, further study to understand the real transport regime in those disordered materials.

Bibliography

- [1] A. H. C. Neto and K. Novoselov, “New directions in science and technology: two-dimensional crystals,” *Rep. Prog. Phys.* **74** (2011) .
- [2] <http://2012books.lardbucket.org/books/principles-of-general-chemistry-v1.0/index.html>.
- [3] <http://www.intel.com/content/www/us/en/silicon-innovations/moores-law-technology.html>.
- [4] “The international technology roadmap for semiconductors: 2012,” .
<http://www.itrs.net/>.
- [5] M. N. Baibich, J. M. Broto, A. Fert, F. N. Van Dau, F. Petroff, P. Etienne, G. Creuzet, A. Friederich, and J. Chazelas, “Giant magnetoresistance of (001)fe/(001)cr magnetic superlattices,” *Phys. Rev. Lett.* **61** (1988) 2472–2475.
- [6] A. F. A. R. Rocha, Thiago B. Martins and A. J. R. da Silva, “Disorder-based graphene spintronics,” *Nanotechnology* **21** (2010) 345202.
- [7] P. R. Wallace, “The band theory of graphite,” *Phys. Rev.* **71** (1947) 622–634.
- [8] L. D. Landau, “Zur theorie der phasenumwandlungen ii. phys,” *Z. Sowjetunion* **11** (1937) 26–35.
- [9] R. E. Peierls, “Bemerkungen ber umwandlungstemperaturen,” *Helv. Phys.* **7** (1937) 81–83.
- [10] K. S. Novoselov, A. K. Geim, S. V. Morozov, D. Jiang, Y. Zhang, S. V. Dubonos, I. Grigorieva, and A. Firsov, “Electric field effect in atomically thin carbon films,” *Science* **306** no. 5696, (2004) 666–669.
- [11] A. H. Castro Neto, F. Guinea, N. M. R. Peres, K. S. Novoselov, and A. K. Geim, “The electronic properties of graphene,” *Rev. Mod. Phys.* **81** (2009) 109–162.

- [12] L. Pauling, “The nature of the chemical bond. application of results obtained from the quantum mechanics and from a theory of paramagnetic susceptibility to the structure of molecules,” *Journal of the American Chemical Society* **53** no. 4, (1931) 1367–1400.
- [13] N. Ashcroft and N. Mermin, *Solid State Physics*. Saunders College, Philadelphia, 1976.
- [14] N. Stander, B. Huard, and D. Goldhaber-Gordon, “Evidence for klein tunneling in graphene p - n junctions,” *Phys. Rev. Lett.* **102** (2009) 026807.
- [15] C. L. Kane and E. J. Mele, “Quantum spin hall effect in graphene,” *Phys. Rev. Lett.* **95** (2005) 226801.
- [16] N. Nemec and G. Cuniberti, “Hofstadter butterflies of bilayer graphene,” *Phys. Rev. B* **75** (2007) 201404.
- [17] A. V. Shytov, M. I. Katsnelson, and L. S. Levitov, “Atomic collapse and quasi-rydberg states in graphene,” *Phys. Rev. Lett.* **99** (2007) 246802.
- [18] S. Yiğen, V. Tayari, J. O. Island, J. M. Porter, and A. R. Champagne, “Electronic thermal conductivity measurements in intrinsic graphene,” *Phys. Rev. B* **87** (2013) 241411.
- [19] J. W. S. S. Lili Sun, Peng Wei and S. Hou, “From zigzag to armchair: the energetic stability, electronic and magnetic properties of chiral graphene nanoribbons with hydrogen-terminated edges,” *J. Phys.: Condens. Matter* **23** (2011) .
- [20] S. Dutta and S. K. Pati, “Novel properties of graphene nanoribbons: a review,” *J. Mater. Chem.* **20** (2010) 8207–8223.
- [21] Y.-W. Son, M. L. Cohen, and S. G. Louie, “Energy gaps in graphene nanoribbons,” *Phys. Rev. Lett.* **97** (2006) 216803.
- [22] O. V. Y. Y.-C. C. J. F. X. Z. R. B. C. J. M. T. A. Z. S. G. L. H. D. . M. F. C. Chenggang Tao, Liying Jiao, “Spatially resolving edge states of chiral graphene nanoribbons,” *Nature Physics* **7** (2011) 616–620.
- [23] M. Y. Han, B. Özyilmaz, Y. Zhang, and P. Kim, “Energy band-gap engineering of graphene nanoribbons,” *Phys. Rev. Lett.* **98** (2007) 206805.
- [24] Z. C. P. Avouris and V. Perebeinos, “Carbon-based electronics,” *Nat. Nano.* **2** (2007) 605–615.

- [25] P. L. L. Tapaszt , G. Dobrik and L. P. Biro, “Tailoring the atomic structure of graphene nanoribbons by scanning tunnelling microscope lithography,” *Nat. Nano.* **3** (2007) 397–401.
- [26] S. S. Datta, D. R. Strachan, S. M. Khamis, and A. T. C. Johnson, “Crystallographic etching of few-layer graphene,” *Nano Letters* **8** no. 7, (2008) 1912–1915. PMID: 18570483.
- [27] L. Ci, Z. Xu, L. Wang, W. Gao, F. Ding, K. Kelly, B. Yakobson, and P. Ajayan, “Controlled nanocutting of graphene,” *Nano Research* **1** (2008) 116–122.
- [28] Y. Guo, W. Guo, and C. Chen, “Semiconducting to half-metallic to metallic transition on spin-resolved zigzag bilayer graphene nanoribbons,” *The Journal of Physical Chemistry C* **114** (2010) 13098–13105.
- [29] H. et al., “Direct evidence for atomic defects in graphene layers,” *Nature* **430** (2004) 870–873.
- [30] P. W. Anderson, “Localized magnetic states in metals,” *Phys. Rev.* **124** (1961) 41–53.
- [31] M. P. Lima, A. R. Rocha, A. J. R. da Silva, and A. Fazzio, “Mimicking nanoribbon behavior using a graphene layer on sic,” *Phys. Rev. B* **82** (2010) 153402.
- [32] C. L. Kane and E. J. Mele, “Quantum spin hall effect in graphene,” *Phys. Rev. Lett.* **95** (2005) 226801.
- [33] Z. Qiao, S. A. Yang, W. Feng, W.-K. Tse, J. Ding, Y. Yao, J. Wang, and Q. Niu, “Quantum anomalous hall effect in graphene from rashba and exchange effects,” *Phys. Rev. B* **82** (2010) 161414.
- [34] Y. Yao, F. Ye, X.-L. Qi, S.-C. Zhang, and Z. Fang, “Spin-orbit gap of graphene: First-principles calculations,” *Phys. Rev. B* **75** (2007) 041401.
- [35] M. Gmitra, S. Konschuh, C. Ertler, C. Ambrosch-Draxl, and J. Fabian, “Band-structure topologies of graphene: Spin-orbit coupling effects from first principles,” *Phys. Rev. B* **80** (2009) 235431.
- [36] D. Huertas-Hernando, F. Guinea, and A. Brataas, “Spin-orbit coupling in curved graphene, fullerenes, nanotubes, and nanotube caps,” *Phys. Rev. B* **74** (2006) 155426.

- [37] M. P. H. T. J. N. Tombros, C. Jozsa and B. J. van Wees, “Spin-orbit coupling in curved graphene, fullerenes, nanotubes, and nanotube caps,” *Nature* **448** (2007) 571574.
- [38] H. Ochoa, A. H. Castro Neto, and F. Guinea, “Elliot-yafet mechanism in graphene,” *Phys. Rev. Lett.* **108** (2012) 206808.
- [39] M. I. Dýakonov and V. I. Perel *Sov. Phys. Solid State* **13** (1972) 3023.
- [40] R. J. Elliott, “Theory of the effect of spin-orbit coupling on magnetic resonance in some semiconductors,” *Phys. Rev.* **96** (1954) 266–279.
- [41] Y. Yafet, “g-factors and spin-lattice relaxation of conduction electrons,” vol. 14 of *Solid State Physics*, pp. 1 – 98. Academic Press, 1963.
- [42] E. Merzbacher, *Quantum mechanics; 2nd ed.* Wiley, New York, NY, 1998.
- [43] M. Born and R. Oppenheimer, “Zur quantentheorie der molekeln,” *Annalen der Physik* **389** no. 20, (1927) 457–484.
- [44] P. Hohenberg and W. Kohn, “Inhomogeneous electron gas,” *Phys. Rev.* **136** (1964) B864–B871.
- [45] W. Kohn and L. J. Sham, “Self-consistent equations including exchange and correlation effects,” *Phys. Rev.* **140** (1965) A1133–A1138.
- [46] J. C. Slater, “The theory of complex spectra,” *Phys. Rev.* **34** (1929) 1293–1322.
- [47] R. G. Parr and Y. Weitao, *Density-Functional Theory of Atoms and Molecules*. Oxford University Press, 1994.
- [48] J. P. Perdew, “Density-functional approximation for the correlation energy of the inhomogeneous electron gas,” *Phys. Rev. B* **33** (1986) 8822–8824.
- [49] P. Gill and P.-F. Loos, “Uniform electron gases,” *Theoretical Chemistry Accounts* **131** (2011) 1–9.
- [50] D. M. Ceperley and B. J. Alder, “Ground state of the electron gas by a stochastic method,” *Phys. Rev. Lett.* **45** (1980) 566–569.
- [51] S. S. L Fernández-Seivane, M A Oliveira and J. Ferrer, “On-site approximation for spinorbit coupling in linear combination of atomic orbitals density functional methods,” *J. Phys.: Condens. Matter* **18** (2006) .
- [52] P. N. C. Caroli, R. Combescot and D. Saint-James, “Direct calculation of the tunneling current,” *J. Phys. C: Solid State Phys.* **4** (1971) .

- [53] A. R. Rocha, V. M. Garc´-Su´arez, S. Bailey, C. Lambert, J. Ferrer, and S. Sanvito, “Spin and molecular electronics in atomically generated orbital landscapes,” *Phys. Rev. B* **73** (2006) 085414.
- [54] M. Bttiker, Y. Imry, R. Landauer, and S. Pinhas, “Generalized many-channel conductance formula with application to small rings,” *Phys. Rev. B* **31** (1985) 6207–6215.
- [55] S. Datta, *Electronic Transport in Mesoscopic Systems*. Cambridge University Press, Cambridge, 1995, 1995.
- [56] A. J. R. d. S. A. R. Rocha, Mariana Rossi and A. Fazzio, “Realistic calculations of carbon-based disordered systems,” *J. Phys. D: Appl. Phys.* **43** (2010) .
- [57] S. Sanvito, C. J. Lambert, J. H. Jefferson, and A. M. Bratkovsky, “General green’s-function formalism for transport calculations with spd hamiltonians and giant magnetoresistance in co- and ni-based magnetic multilayers,” *Phys. Rev. B* **59** (1999) 11936–11948.
- [58] Y.-W. Son, M. L. Cohen, and S. G. Louie, “Erratum: Energy gaps in graphene nanoribbons,” *Phys. Rev. Lett.* **98** (2007) 089901.
- [59] J. D. G. A. G. J. J. P. O. Jos M Soler, Emilio Artacho and D. Snchez-Portal, “The siesta method for ab initio order-n materials simulation,” *J. Phys.: Condens. Matter* **14** (2002) .
- [60] N. Troullier and J. L. Martins, “Efficient pseudopotentials for plane-wave calculations,” *Phys. Rev. B* **43** (1991) 1993–2006.
- [61] A. R. Rocha, J. E. Padilha, A. Fazzio, and A. J. R. da Silva, “Transport properties of single vacancies in nanotubes,” *Phys. Rev. B* **77** (2008) 153406.
- [62] R. Winkler, “Rashba spin splitting in two-dimensional electron and hole systems,” *Phys. Rev. B* **62** (2000) 4245–4248.
- [63] S. Q. J. H. Z Y Li, Z Q Yang and R. Q. Wu, “Spinorbit splitting in graphene on metallic substrates,” *J. Phys.: Condens. Matter* **23** (2011) .
- [64] Y. S. Dedkov, M. Fonin, U. Rdiger, and C. Laubschat, “Rashba effect in the graphene/ni(111) system,” *Phys. Rev. Lett.* **100** (2008) 107602.
- [65] T. O. Wehling, H. P. Dahal, A. I. Lichtenstein, M. I. Katsnelson, H. C. Manoharan, and A. V. Balatsky, “Theory of fano resonances in graphene: The influence of orbital and structural symmetries on stm spectra,” *Phys. Rev. B* **81** (2010) 085413.

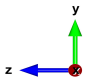
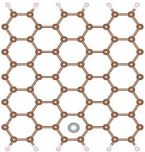
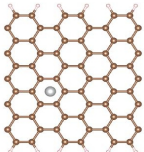
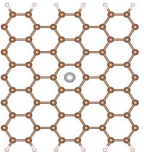
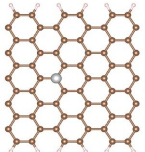
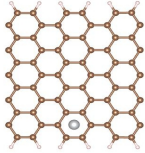

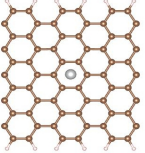
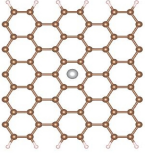
- [66] L. R. F. Lima, F. A. Pinheiro, R. B. Capaz, C. H. Lewenkopf, and E. R. Mucciolo, “Effects of disorder range and electronic energy on the perfect transmission in graphene nanoribbons,” *Phys. Rev. B* **86** (2012) 205111.

Appendix A

Geometry relaxation

A.1 Nickel relaxation

In this section we present a full table of initial and relaxed structures for Ni adatoms in graphene nanoribbon.

		Ni@AGNR-1	Ni@AGNR-2	Ni@AGNR-3	Ni@AGNR-4
Initial structure					
Relaxed structure					
Relative energy [eV]		0.000	0.152	0.176	0.177

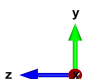
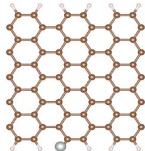
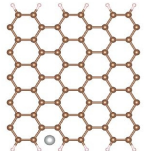
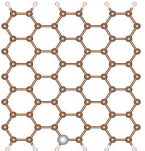
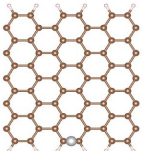
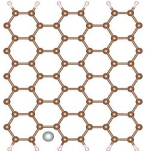
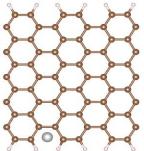
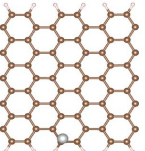

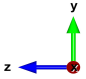
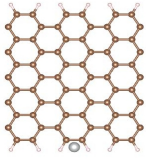
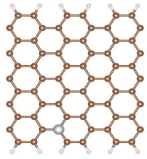
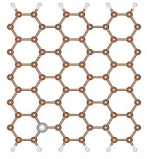
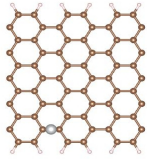
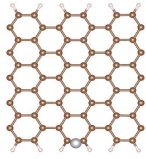
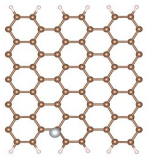
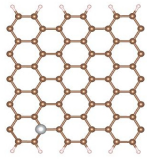
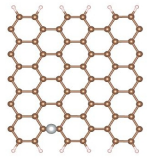
		Ni@AGNR-5	Ni@AGNR-6	Ni@AGNR-7	Ni@AGNR-8
Initial structure					
Relaxed structure					
Relative energy [eV]		0.308	0.314	0.388	0.458

Table A.1: Initial and relaxed structures from Ni@AGNR-1 to Ni@AGNR-8 with their respective relative energy in eV after relaxation.

		Ni@AGNR-9	Ni@AGNR-10	Ni@AGNR-11	Ni@AGNR-12
Initial structure					
Relaxed structure					
Relative energy [eV]		0.487	0.558	0.647	0.660

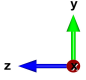
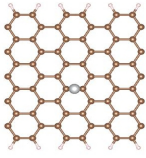
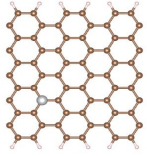
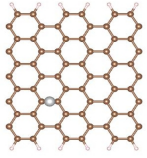
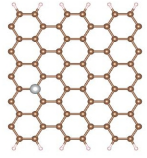
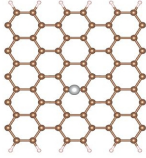
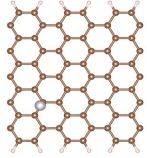
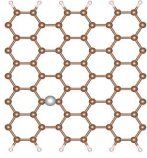
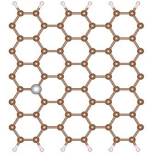
		Ni@AGNR-13	Ni@AGNR-14	Ni@AGNR-15	Ni@AGNR-16
Initial structure					
Relaxed structure					
Relative energy [eV]		0.747	0.759	0.763	0.774

Table A.2: Initial and relaxed structures from Ni@AGNR-9 to Ni@AGNR-16 with their respective relative energy in eV after relaxation.

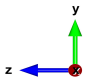
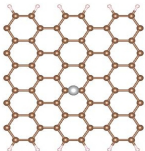
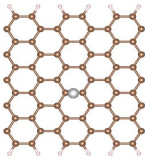
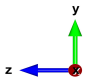
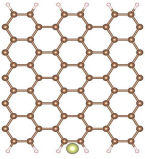
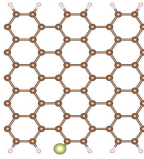
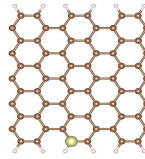
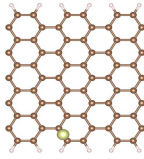
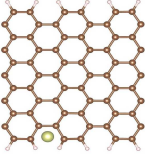
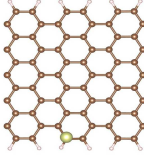
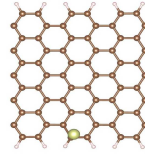
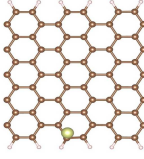
		Ni@AGNR-17
Initial structure		
Relaxed structure		
Relative energy [eV]	0.775	

Table A.3: Initial and relaxed structures of Ni@AGNR-17 with their respective relative energy in eV after relaxation.

A.2 Iridium relaxation

In this section we present a full table of initial and relaxed structures for Ir adatoms in graphene nanoribbon.

		Ir@AGNR-1	Ir@AGNR-2	Ir@AGNR-3	Ir@AGNR-4
Initial structure					
Relaxed structure					
Relative energy [eV]		0.000	0.009	0.024	0.038

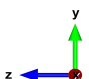
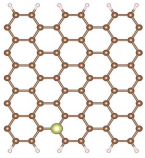
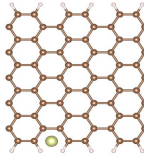
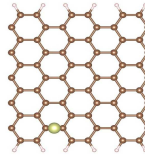
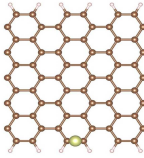
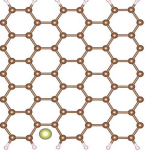
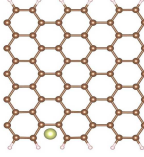
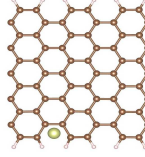
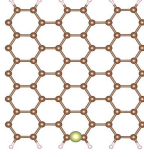
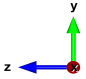
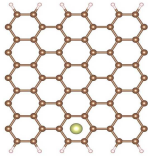
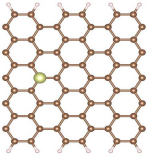
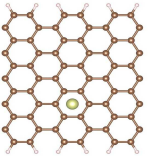
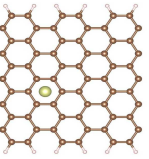
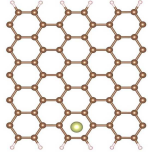
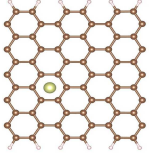
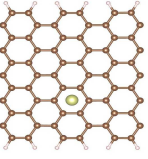
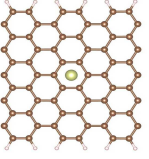
		Ir@AGNR-5	Ir@AGNR-6	Ir@AGNR-7	Ir@AGNR-8
Initial structure					
Relaxed structure					
Relative energy [eV]		0.041	0.042	0.043	0.102

Table A.4: Initial and relaxed structures from Ir@AGNR-1 to Ir@AGNR-8 with their respective relative energy in eV after relaxation.

		Ir@AGNR-9	Ir@AGNR-10	Ir@AGNR-11	Ir@AGNR-12
Initial structure					
Relaxed structure					
Relative energy [eV]		0.264	0.513	0.515	0.516

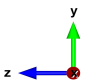
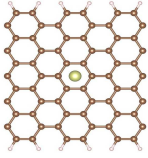
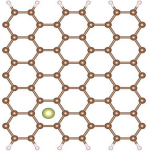
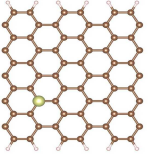
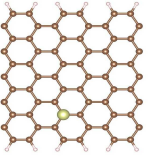
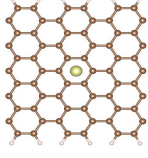
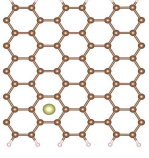
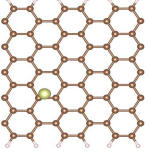
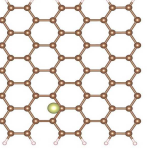
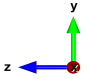
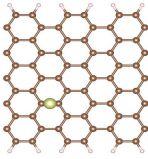
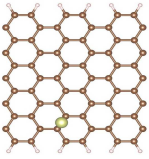
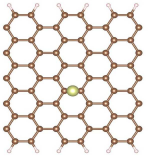
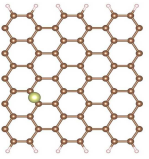
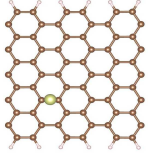
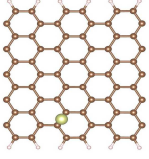
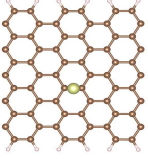
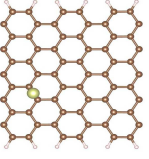
		Ir@AGNR-13	Ir@AGNR-14	Ir@AGNR-15	Ir@AGNR-16
Initial structure					
Relaxed structure					
Relative energy [eV]		0.516	0.525	0.640	0.655

Table A.5: Initial and relaxed structures from Ir@AGNR-9 to Ir@AGNR-16 with their respective relative energy in eV after relaxation.

		Ir@AGNR-17	Ir@AGNR-18	Ir@AGNR-19	Ir@AGNR-20
Initial structure					
Relaxed structure					
Relative energy [eV]		0.692	0.710	0.758	0.767

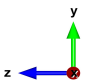
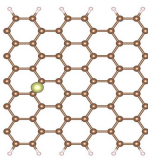
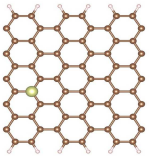
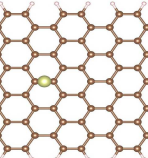
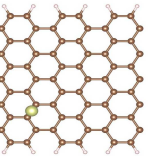
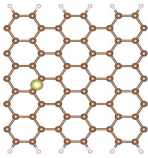
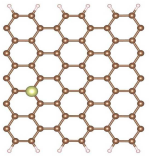
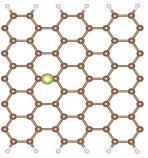
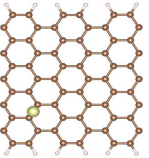
		Ir@AGNR-21	Ir@AGNR-22	Ir@AGNR-23	Ir@AGNR-24
Initial structure					
Relaxed structure					
Relative energy [eV]		0.784	0.813	0.822	0.834

Table A.6: Initial and relaxed structures from Ir@AGNR-17 to Ir@AGNR-24 with their respective relative energy in eV after relaxation.

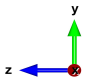
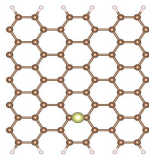
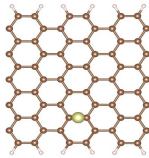
<div></div>		Ir@AGNR-25	
Initial structure			
Relaxed structure			
Relative energy [eV]	0.838		

Table A.7: Initial and relaxed structures of Ir@AGNR-25 with their respective relative energy in eV after relaxation.

Appendix B

Multiple defects spin-polarized transport

B.1 Transmission as a function of Length based on Ni@AGNR-1

B.1.1 At fixed concentration of 0.87 %

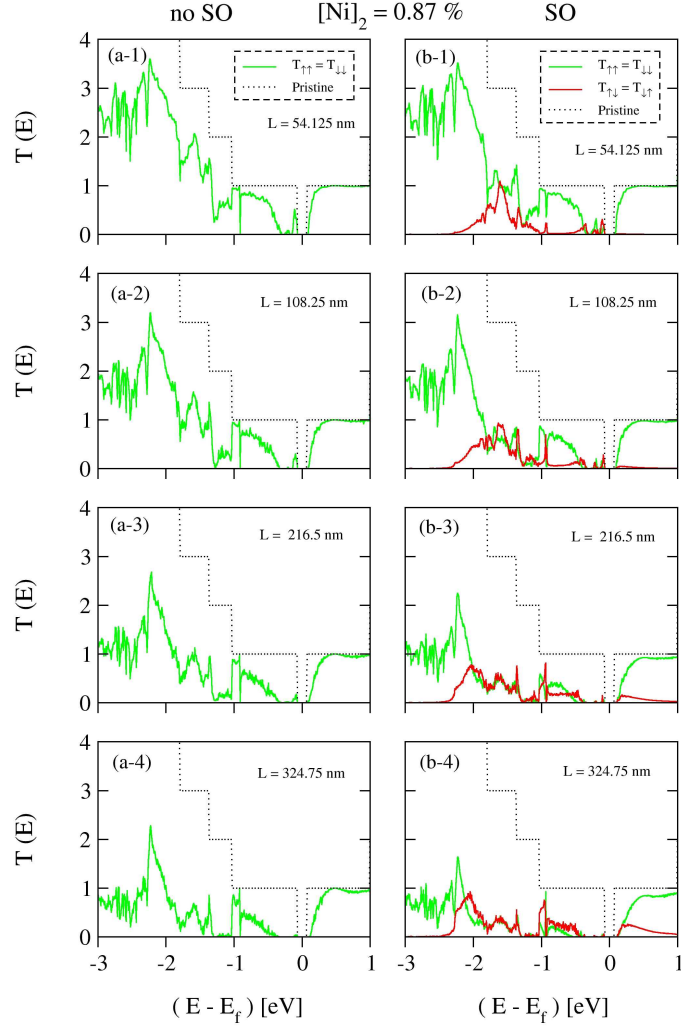


Figure B.1: Disordered transport of nanoribbon at fixed concentration of $[\text{Ni}]_2 = 0.87 \%$. (a) Spin-conserved ($T_{\uparrow\uparrow} = T_{\downarrow\downarrow}$) transmission probabilities without SO coupling; (b) Spin-conserved ($T_{\uparrow\uparrow} = T_{\downarrow\downarrow}$) and spin-flip ($T_{\uparrow\downarrow} = T_{\downarrow\uparrow}$) transmission probabilities with SO coupling. Dashed lines correspond to transport in the pristine AGNR.

B.1.2 At fixed length of 97.425 nm

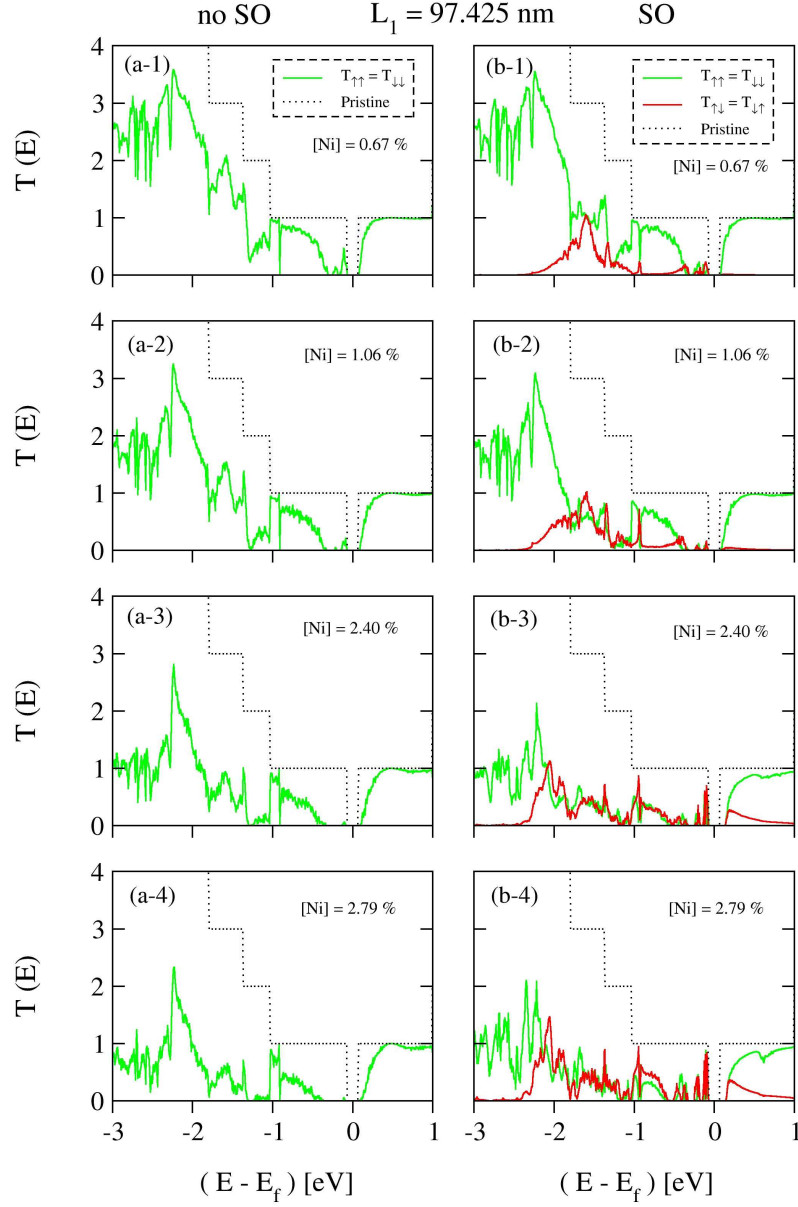


Figure B.2: Disordered transport of nanoribbon at fixed length of $L_1 = 97.425$ nm. (a) Spin-conserved ($T_{\uparrow\uparrow} = T_{\downarrow\downarrow}$) transmission probabilities without SO coupling; (b) Spin-conserved ($T_{\uparrow\uparrow} = T_{\downarrow\downarrow}$) and spin-flip ($T_{\uparrow\downarrow} = T_{\downarrow\uparrow}$) transmission probabilities with SO coupling. Dashed lines correspond to transport in the pristine AGNR.

B.1.3 At fixed length of 194.85 nm

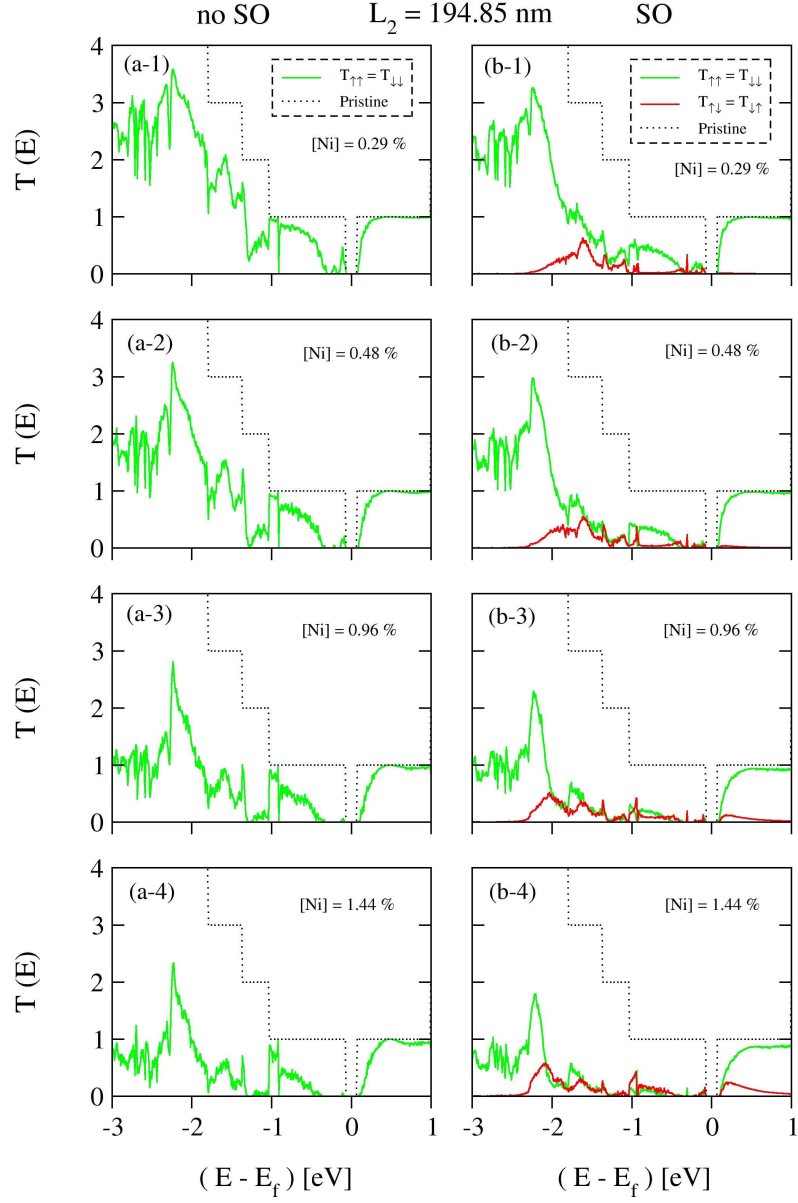


Figure B.3: Disordered transport of nanoribbon at fixed length of $L_2 = 194.85$ nm. (a) Spin-conserved ($T_{\uparrow\uparrow} = T_{\downarrow\downarrow}$) transmission probabilities without SO coupling; (b) Spin-conserved ($T_{\uparrow\uparrow} = T_{\downarrow\downarrow}$) and spin-flip ($T_{\uparrow\downarrow} = T_{\downarrow\uparrow}$) transmission probabilities with SO coupling. Dashed lines correspond to transport in the pristine AGNR.

B.2 Disordered transport based on Ni@AGNR-s

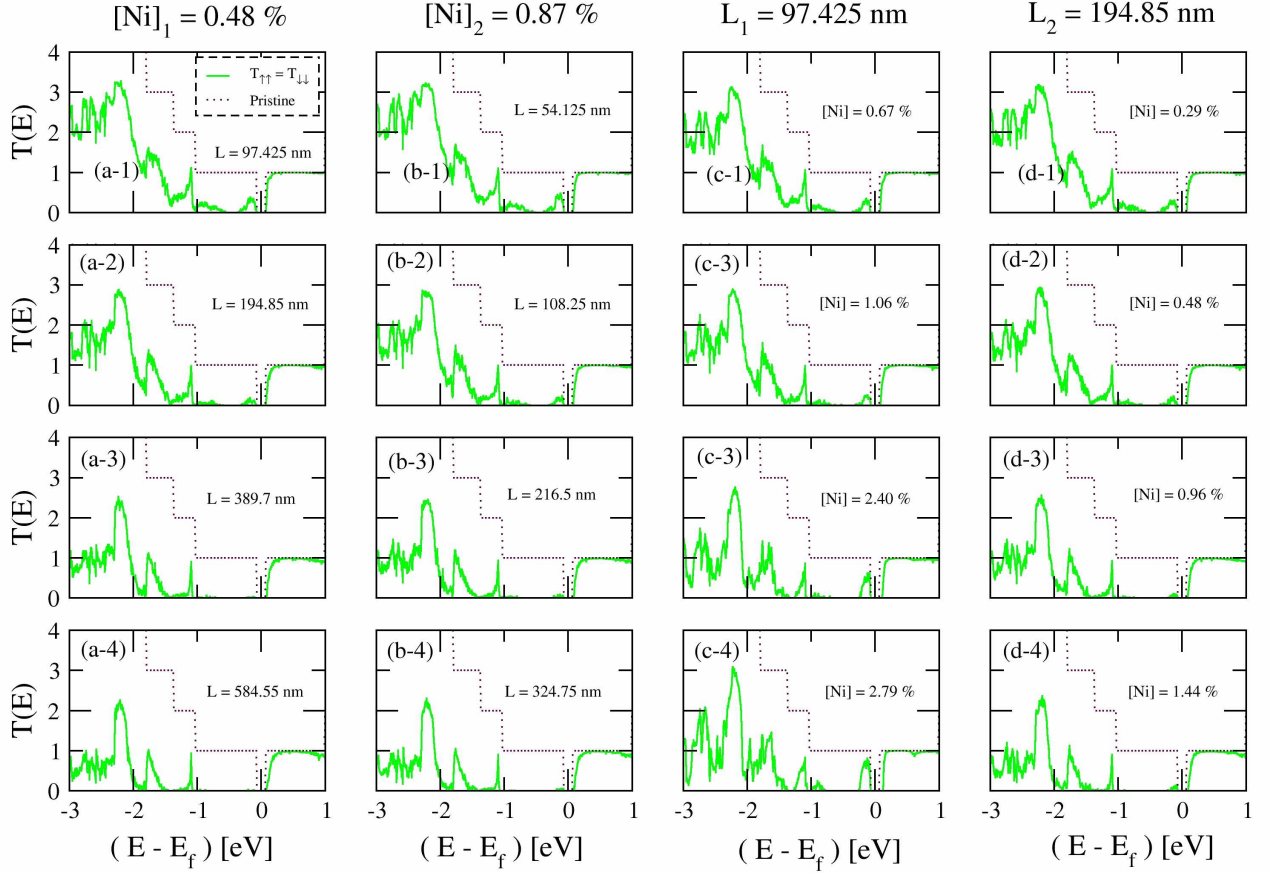


Figure B.4: Spin-conserved transmission coefficients ($T_{\uparrow\uparrow} = T_{\downarrow\downarrow}$) without spin-orbit coupling as a function of energy of disordered ribbon based on Ni@AGNR-s structure. (a) At fixed concentration of $[Ni]_1 = 0.48 \%$; (b) At fixed concentration of $[Ni]_2 = 0.87 \%$; (c) At fixed nanoribbon length of $L_1 = 97.425$ nm and (d) At fixed nanoribbon length of $L_2 = 194.85$ nm. Dashed lines are the transmission coefficients for pristine AGNR.

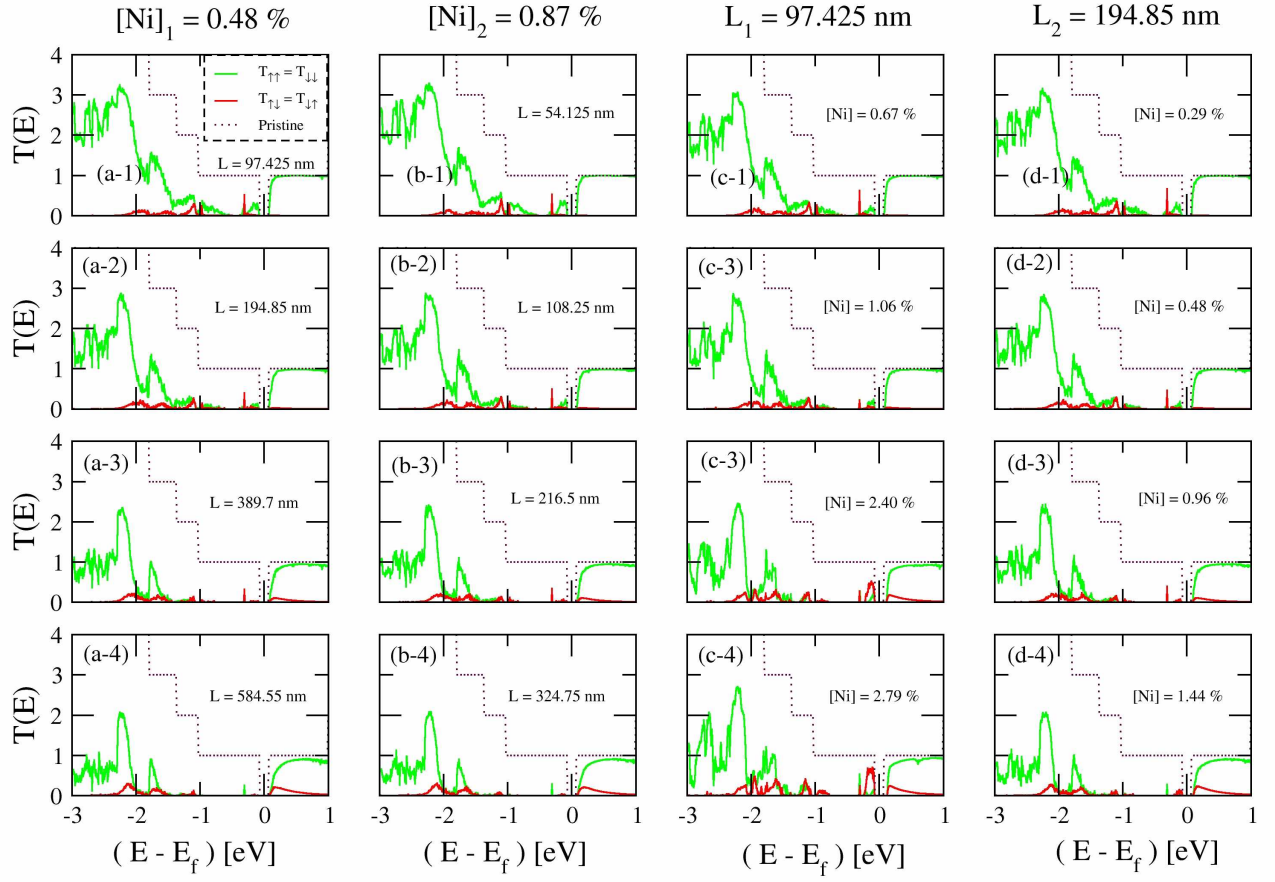


Figure B.5: Spin-conserved transmission coefficients ($T_{\uparrow\uparrow} = T_{\downarrow\downarrow}$) with spin-orbit coupling as a function of energy of disordered ribbon based on Ni@AGNR-s structure. (a) At fixed concentration of $[\text{Ni}]_1 = 0.48 \%$; (b) At fixed concentration of $[\text{Ni}]_2 = 0.87 \%$; (c) At fixed nanoribbon length of $L_1 = 97.425 \text{ nm}$ and (d) At fixed nanoribbon length of $L_2 = 194.85 \text{ nm}$. Dashed lines are the transmission coefficients for pristine AGNR.

B.2.1 At fixed concentration of 0.48 %

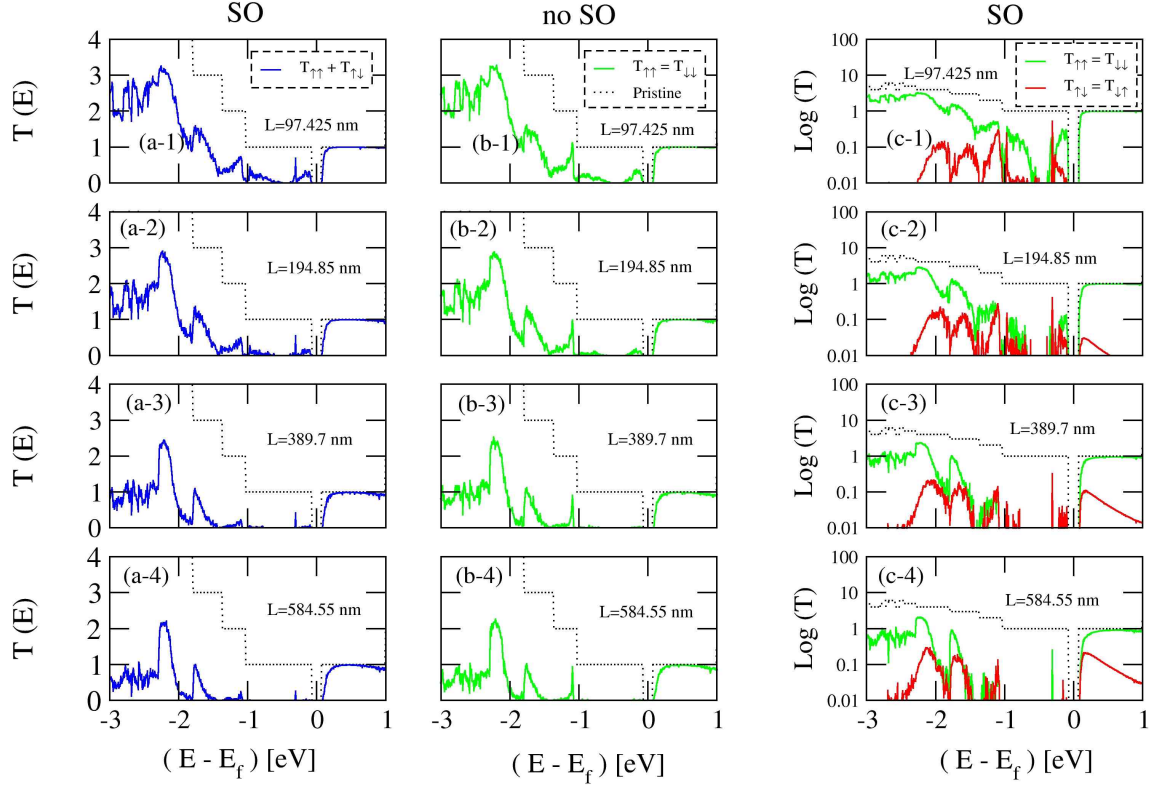


Figure B.6: Disordered transport of nanoribbon at fixed concentration of 0.48 %. (a) Total conductance ; (b) Spin-conserved ($T_{\uparrow\uparrow} = T_{\downarrow\downarrow}$) transmission probabilities without SO coupling; (c) Spin-conserved ($T_{\uparrow\uparrow} = T_{\downarrow\downarrow}$) and spin-flip ($T_{\downarrow\downarrow} = T_{\uparrow\uparrow}$) transmission probabilities with SO coupling in logarithmic scale. Dashed lines correspond to transport in the pristine AGNR.

B.2.2 At fixed concentration of 0.87 %

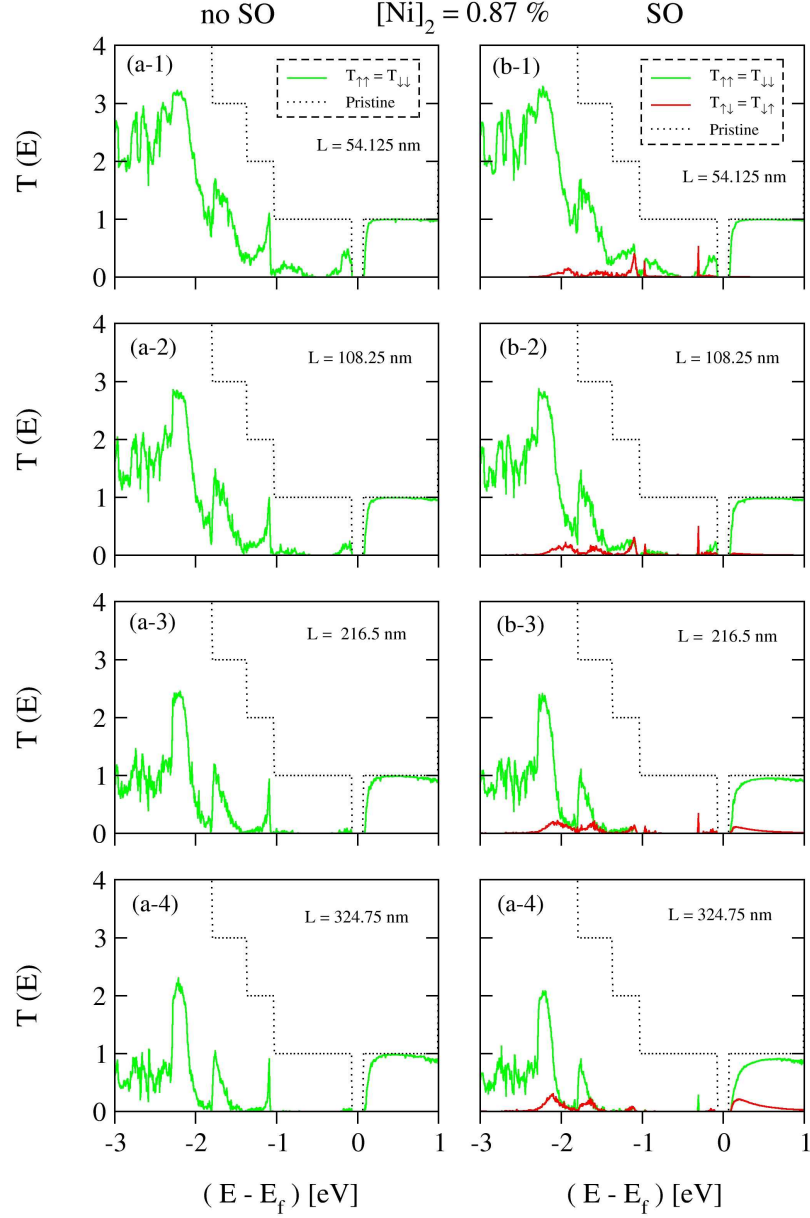


Figure B.7: Disordered transport of nanoribbon at fixed concentration of 0.87 %. (a) Spin-conserved ($T_{\uparrow\uparrow} = T_{\downarrow\downarrow}$) transmission probabilities without SO coupling; (b) Spin-conserved ($T_{\uparrow\uparrow} = T_{\downarrow\downarrow}$) and spin-flip ($T_{\uparrow\downarrow} = T_{\downarrow\uparrow}$) transmission probabilities with SO coupling. Dashed lines correspond to transport in the pristine AGNR.

B.2.3 At fixed length of 97.425 nm

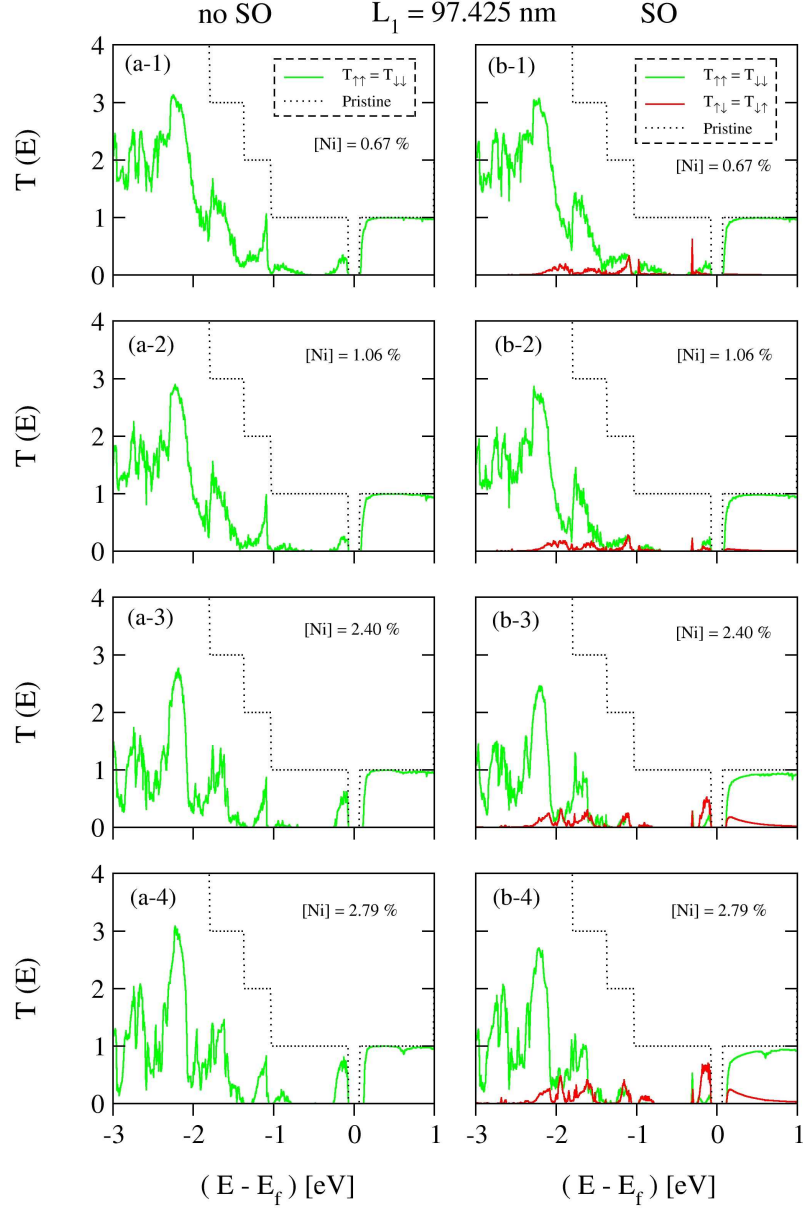


Figure B.8: Disordered transport of nanoribbon at fixed length of $L_1 = 97.425$ nm. (a) Spin-conserved ($T_{\uparrow\uparrow} = T_{\downarrow\downarrow}$) transmission probabilities without SO coupling; (b) Spin-conserved ($T_{\uparrow\uparrow} = T_{\downarrow\downarrow}$) and spin-flip ($T_{\uparrow\downarrow} = T_{\downarrow\uparrow}$) transmission probabilities with SO coupling. Dashed lines correspond to transport in the pristine AGNR.

B.2.4 At fixed length of 194.85 nm

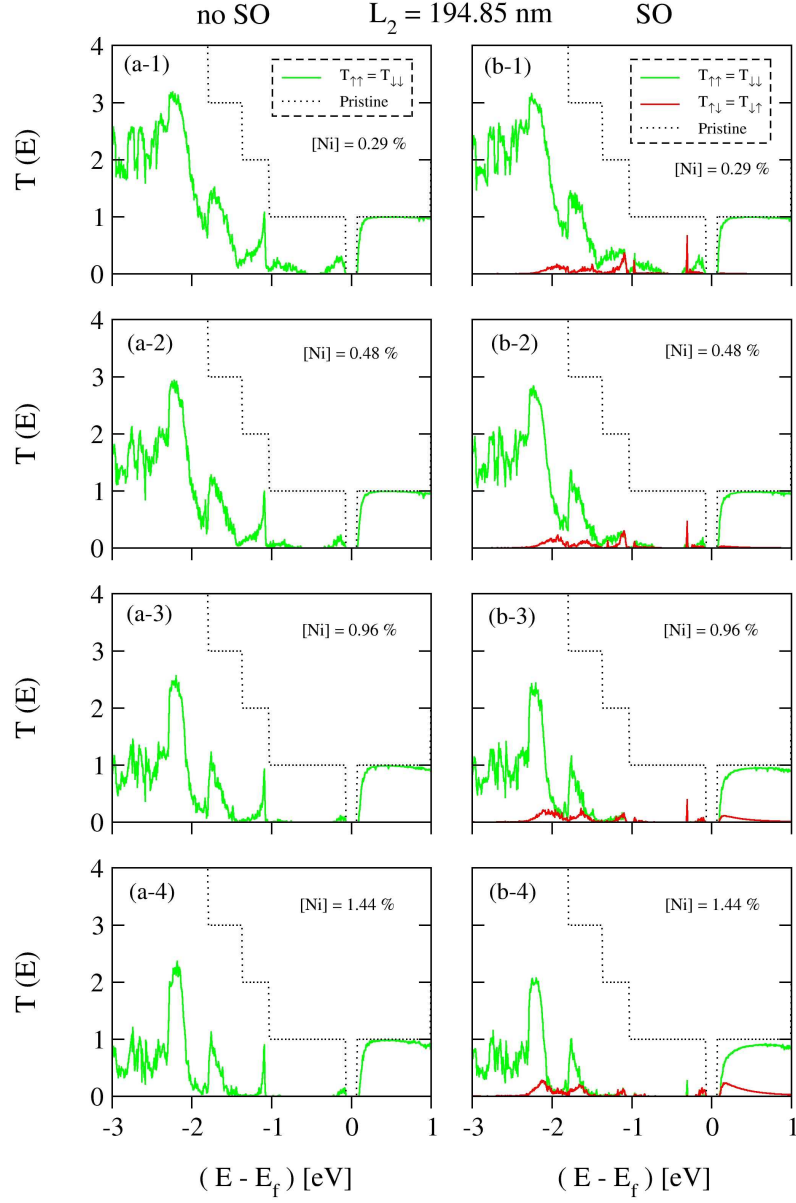


Figure B.9: Disordered transport of nanoribbon at fixed length of $L_2 = 194.85$ nm. (a) Spin-conserved ($T_{\uparrow\uparrow} = T_{\downarrow\downarrow}$) transmission probabilities without SO coupling; (b) Spin-conserved ($T_{\uparrow\uparrow} = T_{\downarrow\downarrow}$) and spin-flip ($T_{\uparrow\downarrow} = T_{\downarrow\uparrow}$) transmission probabilities with SO coupling. Dashed lines correspond to transport in the pristine AGNR.